NASA Contractor Report 194894

IN-71
5101
120 P

Computational Analysis of High Resolution Unsteady Airloads for Rotor Aeroacoustics

Todd R. Quackenbush, C.-M. Gordon Lam, Daniel A. Wachspress
Continuum Dynamics, Inc., Princeton, New Jersey

Donald B. Bliss
Duke University, Durham, North Carolina

Contract NAS1-19303

May 1994

Computational Analysis of High Resolution Unsteady Airloads for Rotor Aeroacoustics

Todd R. Quackenbush, C.-M. Gordon Lam, Daniel A. Wachspress
Continuum Dynamics, Inc., Princeton, New Jersey

Donald B. Bliss
Duke University, Durham, North Carolina

COMPUTATIONAL ANALYSIS OF HIGH RESOLUTION UNSTEADY AIRLOADS FOR ROTOR AEROACOUSTICS

Todd R. Quackenbush, C.-M. Gordon Lam, Daniel A. Wachspress and Donald B. Bliss*

Continuum Dynamics, Inc.
Princeton, New Jersey 08543

*Duke University
Durham, North Carolina 27006

SUMMARY

The study of helicopter aerodynamic loading for acoustics applications requires the application of efficient yet accurate simulations of the velocity field induced by the rotor's vortex wake. This report summarizes work to date on the development of such an analysis, which builds on the refined Constant Vorticity Contour (CVC) free wake model, previously implemented for the study of vibratory loading in the RotorCRAFT computer code. The primary focus of the present effort has been on implementation of an airload reconstruction approach that computes high resolution airload solutions of rotor/rotor-wake interactions required for acoustics computations. Supplementary efforts on the development of improved vortex core modeling, unsteady aerodynamic effects, higher spatial resolution of rotor loading, and fast vortex wake implementations have substantially enhanced the capabilities of the resulting software, denoted RotorCRAFT/AA (AeroAcoustics). Results of validation calculations using recently-acquired model rotor data are presented, as are other demonstration calculations on main rotors and tail rotors. These calculations show that by employing airload reconstruction it is possible to apply the CVC wake analysis with temporal and spatial resolution suitable for acoustics applications while reducing the computation time required by one to two orders of magnitude relative to the direct calculations used in traditional methods. Promising correlation with measured airload and noise data has been obtained for a variety of rotor configurations and operating conditions.

TABLE OF CONTENTS

NOMENCLATURE

A	matrix of influence coefficients defined in Eq. 6-10
C_N	spanwise normal force coefficient $\left(N/\tfrac{1}{2} \rho \, V_{local}^2 \, c_{local}\right)$
C_T	rotor thrust coefficient
$\bar{c}$	mean blade chord
c_{local}	local blade chord
D	vortex age parameter, $\tfrac{1}{2}\left(\Gamma/k_R^2\right)\phi$
dC_T/dx	spanwise thrust coefficient, dT/dr normalized by $\tfrac{1}{2}\rho\,(\Omega R)^2\,\bar{c}$
dT/dr	spanwise distributed thrust
G	indicial pressure response function of an unsteady loaded wing
k_R	nondimensional distance inboard of blade tip $(R-r)/R$
k_x	wave number of the spanwise component of a gust field
k_y	wave number of the chordwise component of a gust field
l_{jk}	length of kth side of jth quadrilateral
R	main rotor radius
r	radial distance from rotor hub
r_c	physical vortex core radius
r_f	artificial ('fat') vortex core radius
r_s	laminar core radius
r_t	turbulent core radius
s	nondimensional time defined in Eq. 6-1 or span of the tip vortex rollup region
s_{jk}	unit vector giving the direction of the kth side of the jth quadrilateral
s_T	nondimensional time increment corresponding to one rotor azimuthal increment
T	total rotor thrust or time for one rotor azimuthal increment
U	mean freestream onset velocity in the tip region
U_∞	free stream velocity component in X direction
V_{local}	local free stream speed, $\Omega r + U_\infty \sin\psi$
v_θ	vortex swirl velocity
w_j	downwash velocity at the control point of the jth vortex quadrilateral
X,Y,Z	global axes centered at the rotor hub (X positive aft, Z positive down)
$\vec{x}_{cm}$	centroid of a group of vortex elements
$\vec{x}_i$	position of ith collocation point
α_s	shaft angle of attack
Γ	vortex filament circulation or bound circulation at the inboard edge of the tip vortex rollup region
$\bar{\Gamma}$	normalized bound circulation, $\Gamma/\Omega R^2$
ϵ	nondimensional blade tip loading parameter $\Gamma/2\pi s U$
γ_j	bound circulation at jth vortex quadrilateral
Δp	difference in pressure between upper and lower surfaces of a blade

θ	rotor blade root pitch angle
λ_x	wave length of the spanwise component of a gust field
λ_y	wave length of the chordwise component of a gust field
μ	rotor advance ratio, $U_\infty/\Omega R$
v_i	volume of ith vortex element
Φ_{rt}	indicial response function for near wake downwash
ϕ	azimuthal age of a vortex element
ψ	azimuth angle
ψ_{ovl}	azimuthal extent of the overlap region
Ω	main rotor angular velocity
$\bar{\omega}_i$	vorticity associated with ith vortex element

1.0 INTRODUCTION

The efficient and accurate computation of wake-induced loading on helicopter blades is an important topic for many rotorcraft applications. One such application is rotorcraft noise analysis, where one of the most significant challenges is the problem of prediction of noise from rotor/wake interactions. Such noise is generated both by interactions of main rotor blades with their own wake as well as main rotor / tail rotor interactions. Very accurate computation of the wake influence is required for noise calculations, along with high temporal resolution. Previous efforts (Refs. 1 and 2) addressed an important component of the prediction of unsteady loads, namely the analysis of wake-induced flow fields. This work was carried out in part to demonstrate an exceptionally efficient approach to the generation of high-resolution velocity field calculations, based on the method of flow field reconstruction. The work on this topic has covered a wide range of wake/rotor interactions, including the interaction of the main rotor with its own wake (Ref. 1) and main rotor/tail rotor interactions (Ref. 2).

The present report summarizes work on the development of a comprehensive analysis of rotor aerodynamics designed to obtain high resolution loading for aeroacoustics applications. The point of departure for this development effort was the RotorCRAFT (Computation of Rotor Aerodynamics in Forward flighT) code (Refs. 3 and 4). The analysis that has emerged from the present effort has dramatically expanded capabilities relative to its parent code. The new analysis has been designated RotorCRAFT/AA (AeroAcoustics) to indicate its new focus. Broadly, the new capabilities of RotorCRAFT/AA include:

- flow field and airload reconstruction capabilities that permit high-resolution computations with a reduction of from one to two orders of magnitude in CPU relative to direct free wake computations.

- additional efficiency enhancements, including fast vortex methods based on multipole expansions, that produce a factor of 5 to 10 in CPU reduction in addition to that realized by reconstruction.

- improved models of unsteady aerodynamic effects.

- high resolution blade surface pressure modeling, including thickness effects

- multilayer vortex core modeling, permitting more realistic predictions of wake-induced velocity fields during close blade/vortex encounters.

- dual rotor modeling capability to address main rotor / tail rotor interactions

After a brief review of related efforts, the technical details of these and related basic features of RotorCRAFT/AA will be described. Results involving the application of reconstruction techniques to both flow field and airload prediction will be presented, including comparisons to recently acquired measurements of unsteady loads on main rotor blades. Finally, the priorities currently envisioned for follow-on work to build on the present code for still more advanced implementations will be summarized.

1.1 Background

As noted, the motivation for the work described here was the analysis of rotor noise due to wake/rotor interactions. Substantial effort has gone into both experimental

1

and analytical study of the general topic of rotorcraft acoustics in recent years (Refs. 5-11). Experimental studies such as References 6 and 7 have amply demonstrated the importance of blade/wake interaction in the generation of loading noise. Though recent analytical and computational work has shown some progress toward predicting rotor noise (Refs. 8-11), it is clear that substantial problems remain to be solved.

An obvious prerequisite to successful prediction of rotor noise is accurate analysis of unsteady aerodynamic loading, which in turn depends on an ability to correctly model the structure of the main rotor wake and the velocity field it induces. Recent studies of rotor wake vortex dynamics have produced a rotor wake model that is superior in refinement, consistency, and efficiency to previous treatments. It was found in Reference 12 that in order to successfully predict main rotor aerodynamic loads, it is necessary to account for the vortex wake generated by the entire blade span, not just the tip region. A particularly attractive implementation of a full-span wake involves modeling the wake by a field of constant strength filaments which correspond to the actual resultant vorticity field in the wake (see Fig. 1-1, which shows the wake of one blade of a four-bladed rotor at advance ratio 0.3). These vortex filaments are laid out on contours of constant vortex sheet strength in the rotor wake, a circumstance that gives the method its name: the Constant Vorticity Contour (CVC) wake model. The CVC wake model treats each curved vortex element as a resultant vector of the local vorticity field, an approach that removes the essentially artificial distinction between "shed" and "trailed" vorticity. Figure 1-1 shows the very complicated incident wake structure generated by typical rotors; this complex structure leads to a wide range of possible interactions of the wake with the main rotor blades, as well as the potential for significant main rotor/tail rotor (MR/TR) interactions. Figure 1-2 illustrates the still more complex vorticity fields that can arise in low speed flight, when wake-on-wake interaction becomes particularly significant.

References 3 and 12 discuss the development of the CVC vortex dynamics analysis method and document its success in the prediction of main rotor blade unsteady airloading. The resulting RotorCRAFT code uses a vortex lattice representation of the blade to predict aerodynamic loads and a finite element model of the rotor blade structure. RotorCRAFT incorporates a full flap/lag/torsion aeroelastic model that captures realistic blade deflections, as well as a trim algorithm that ensures that the rotor loading is calculated using consistent control settings. References 3, 4, and 13 describe the technical substance of RotorCRAFT as well as its application to a variety of calculations of practical importance, including studies of steady and unsteady aerodynamic loads on rotors in both high- and low-speed flight.

Reference 4 describes the extension of the RotorCRAFT code to the computation of blade stresses and hub loads. This work was motivated by the desire to support recent research into the application of higher harmonic pitch control for the alleviation of rotor noise. Experimental studies have shown considerable promise in the strategy of applying four-per-rev(4P) root pitch control to reduce rotor noise (Ref. 14). However, the effect of such control strategies on vibratory load levels must be considered. To address such issues, an extended version of RotorCRAFT - denoted Mod 1.0 - was developed that allowed for the calculation of internal blade stresses as well as forces and moments at the rotor hub. Representative results of this work are presented in Reference 4.

While the existing variants of the basic RotorCRAFT code embodied a significant capability for the prediction of unsteady airloads, a substantial increment in performance was required to enable the analysis to resolve rotor loading on the time scales necessary for the direct prediction of rotor acoustics. Moreover, additional features had to be added to permit the computation of distributed surface pressures in a form suitable for input to
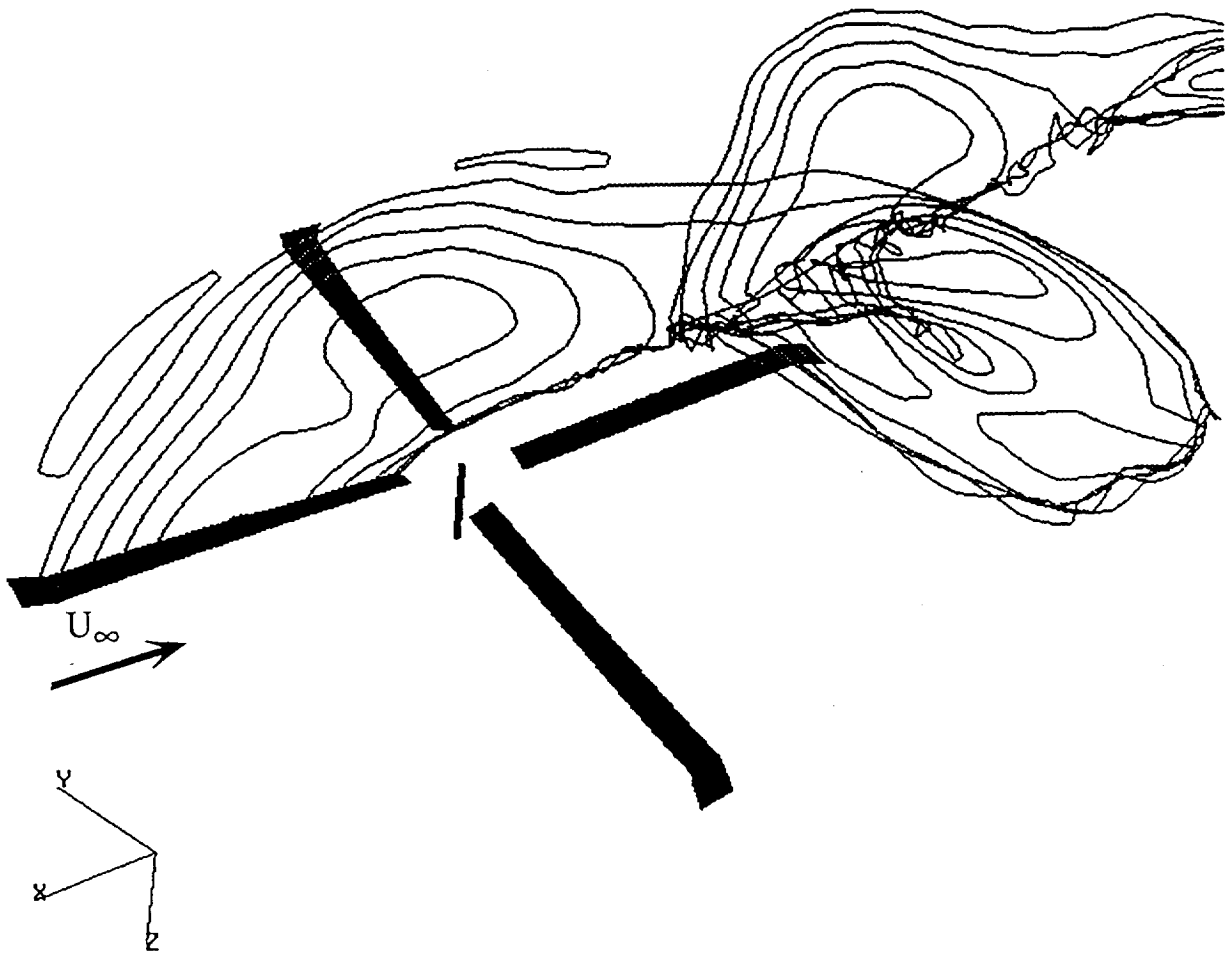
2

U_∞

Figure 1-1. Typical Constant Vorticity Contour (CVC) wake geometry for a UH-60 main rotor at advance ratio 0.3 (only the wake of one blade is shown for clarity).
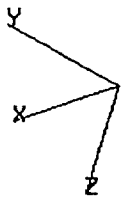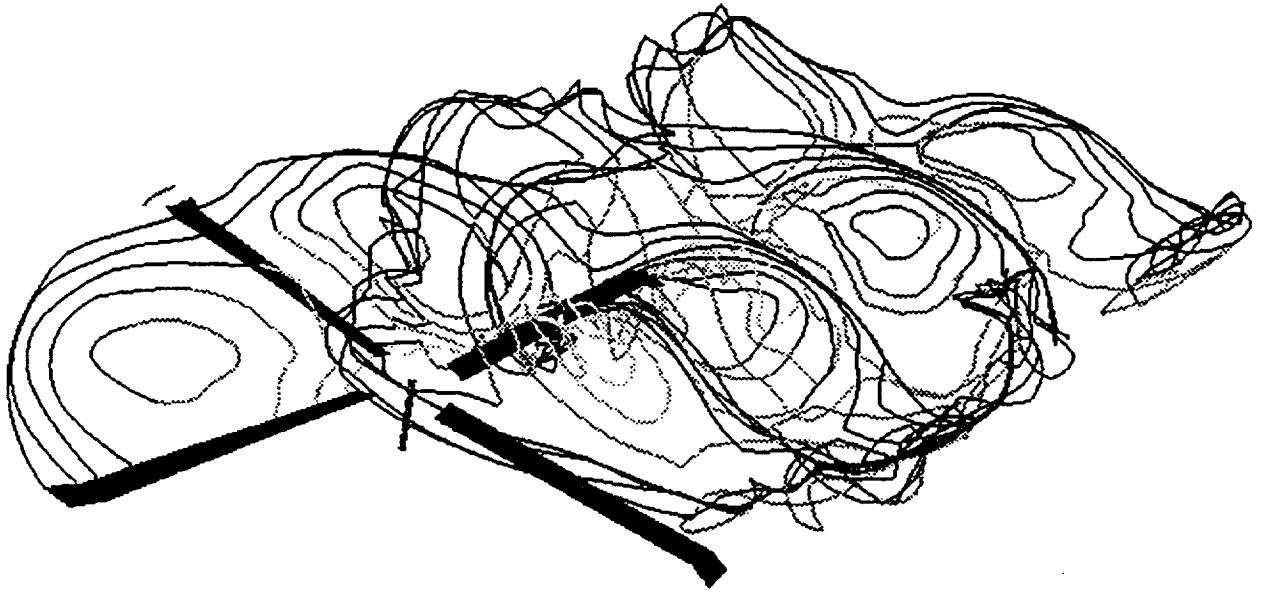
3

Figure 1-2. CVC rotor wake geometry for a UH-60A rotor in low speed flight, advance ratio 0.136 .

rotor noise analyses such as NASA's WOPWOP code (Ref. 15). Finally, basic improvements also were required in a variety of areas, such as the modeling of near wake unsteady effects on the rotor blade, enhanced representations of vortex core structure, and the capability to analyze main rotor / tail rotor systems.

These requirements constituted the technical motivation for the development of RotorCRAFT /AA. The sections that follow address the major elements of the code in detail. Sections 2 and 3 describe the methods used to accelerate the vortex wake computations, focusing on flow field reconstruction and fast vortex methods; Sections 4 and 5 discuss fundamental improvements to the wake and blade models; Section 6 describes the computation of surface pressure distributions and the calculation of rotor noise; Section 7 details the results of an extensive correlation study for both rotor airloads and noise; and Section 8 summarizes the work to date, as well as the likely priorities for follow-on work.

2.0 FLOW FIELD AND AIRLOAD RECONSTRUCTION

The results discussed in References 3 and 4 address the prediction of unsteady loads that contribute to rotor vibration, but aerodynamic loads of much higher characteristic frequency must be resolved to predict rotor noise. This means that very small time steps must be used to discretize each rotor revolution. Since the CVC wake model is a Lagrangian description of the vortex wake, it suffers from problems with computational efficiency common to all such methods when very high temporal resolution of the flow is required. A 'reconstruction' approach has been developed to allow the refined flow field model inherent in the CVC wake description to be retained while reducing the computational requirements from one to two orders of magnitude relative to direct, conventional Lagrangian computations of unsteady vorticity fields. Previous papers and reports have outlined the operation of this approach, which will be briefly summarized in this section, along with results of demonstration calculations.

2.1 Outline of Reconstruction

The first step in motivating the reconstruction approach is to appreciate that the rapid temporal variations in the velocity field (and airloads) observed on rotor blades encountering the vortex wake are directly related to the steep spatial velocity gradients they experience during such interactions. Small time steps are required to resolve these interactions, leading to large CPU times for conventional Lagrangian models. In such models, traditional practice is to model several turns of the vortex wake with freely distorting vortex elements; one element is introduced in the flow field at each time step (typically at the generating rotor blade) while one is removed (or merged into a prescribed far wake model) at the end of the free wake region. The computation time scales with the quantity $N_T N_E^2$, where N_T is the number of time steps per blade revolution and N_E is the number of wake elements. Doubling the number of time steps per revolution requires twice as many wake elements to represent the same length of free wake. Therefore, the computation time scales with the cube of the number of time steps.

Now consider a different approach that could circumvent this very substantial computational burden. First assume that the core size of the main rotor vortices penetrating or approaching a region of interest $\mathcal{R}$ could be increased arbitrarily (the "region of interest" or "evaluation region" is typically a grid of points on the main rotor or tail rotor blades). This would make the velocity gradients encountered by the rotor blades much smoother and, consequently, far fewer time steps would be required to resolve the blade loads to an acceptable degree of accuracy. A simulation with artificially "fat" vortex cores could thus be undertaken with a complex Lagrangian model such as the full-span CVC wake using reasonable amounts of CPU time, though the solution would be physically meaningless because of the artificial smoothing. However, if the use of the fat core were restricted to computation of the induced velocity in $\mathcal{R}$ and the actual vortex core were used elsewhere (e.g., wake-on-wake interactions) then the motion of the vortex wake through the region of interest would be correct; any errors due to the use of the fat core would only affect the nearfield flow used to compute wake-induced velocities on the points in $\mathcal{R}$.

This approach assumes that the correct velocity profile inside the vortex core (i.e., the 'actual core' solution) is known or that the analyst is willing to specify a suitable approximation to it. Given this additional assumption, it is possible to construct nearfield corrections to recover the physically correct solution with the actual core from the smoothed velocity field with low temporal resolution. Since this correction scheme is

6

applied only to the relatively small number of points of evaluation in $\mathcal{R}$, the total CPU time required should be negligible compared to the CVC rotor wake calculation required to define the wake geometry. Also, the time evolution of the vortex wake elements in $\mathcal{R}$ is handled through interpolation of the filament trajectories. Since the low-resolution filament trajectories are interpolated (as opposed to induced velocities), higher effective time resolution can be obtained.

Using this general approach, then, computations yielding high spatial and temporal resolution of the wake flow field could become much more efficient, since high local accuracy is obtained by matching in an appropriate nearfield solution rather than by direct computation of the vortex wake geometry using small time steps. Clearly, the execution of such a local nearfield correction is crucial to the accuracy of this method. A further discussion of the nearfield correction scheme used here is given in Section 2.2, with further discussion in Section 4.

The first step in the overall computation is to run the CVC free wake model in RotorCRAFT/AA for a specified number of main rotor revolutions using relatively coarse time steps, usually between thirty and fifty steps per main rotor revolution. At each time step the velocity field generated at specified points within a user-defined evaluation region $\mathcal{R}$ is calculated and stored; for most applications of interest here, $\mathcal{R}$ coincides with the surface of the rotor blades. Simultaneously, the positions and orientations of vortex filament intersections with a reference volume that encompasses $\mathcal{R}$ are also recorded. The role of this volume and of the planes bounding it is to define a convenient reference for the geometry of the vortex filaments in the near field of $\mathcal{R}$, allowing correction terms to be applied. These computations comprise the initial (and by far the most computationally costly) phase of the overall analysis. It is important to note, however, that this calculation requires vastly less computation time than would a direct calculation at the refined time steps normally required for acoustics calculations.

Once this portion of the simulation is completed, a reconstruction program is used to take the stored information on the wake-induced velocity field and the "tracks" of the vortex intersections with the scan planes and regenerate the velocity field induced by the transit of the actual wake vortices through the vicinity of $\mathcal{R}$. This is accomplished by first interpolating the smoothed velocity field generated by using the fat core to yield the "background" flow at each of the evaluation points, i.e. a low-resolution solution for the flow field. Note that this is interpolation in time, which can be carried out in confidence because the use of the fat core has eliminated the steep velocity gradients from the velocity field at the points of evaluation. Second, the positions of the vortex elements within the scan volume are also interpolated providing the information needed for producing high temporal resolution histories of the vortex trajectories and thus of the local flow field. By applying the nearfield analytical correction terms detailed in References 1 and 2 to the low-resolution flow computed using the fat core, the velocity induced using the actual vortex core can be recaptured while simultaneously refining the time history of the flow field at the selected evaluation points.

As noted above, the reduction in CPU typically scales with the cube of the temporal interpolation factor, i.e., a factor of 5 should yield roughly two orders of magnitude reduction in CPU time. A flow chart depicting the major features of the reconstruction procedure is given in Figure 2-1. Note that this flow chart depicts the generation of aerodynamic loads as well as high resolution flow field calculations; the methods used for the computation of such loads will be outlined in the next section.

7

Inputs:
```
-Rotor Geometry  - Fat Core Radius
-Flight Condition  - Interpolation Factor
-Scan Plane /    - Noise Evaluation
 Scan Volume       Points
 Configuration   - Pitch inputs
```

RotorCRAFT
Procedures

Initial Blade Loading
Estimation Routine

Optional: Invoke WOPWOP
for Noise Time History
at Specified Points (e.g.,
microphone locations)

Main Rotor CVC
Wake Model with
Fat Core

Vibratory
Hub Loads

High Resolution Blade
Loading Solution

Scan Volume
Filament Intersection
Tracking Routine

Low Resolution Flow Field
and Vortex Lattice Blade Loads

Vortex Intersection
Postions and Orientations

Intersection Event Sorting
and Track Formation
Program

Matching Routine for
Lifting Surface Loads
and Chordwise Pressure
Distributions (Optional
Thickness Correction)

Velocity Field and
Trajectory Interpolation
Routine

High Resolution Blade
Lattice for Chordwise
Pressure Distribution

Nearfield Velocity Corrections
with Refined Core Model

High Resolution Flow Field at the
Instantaneous Blade Surface Position
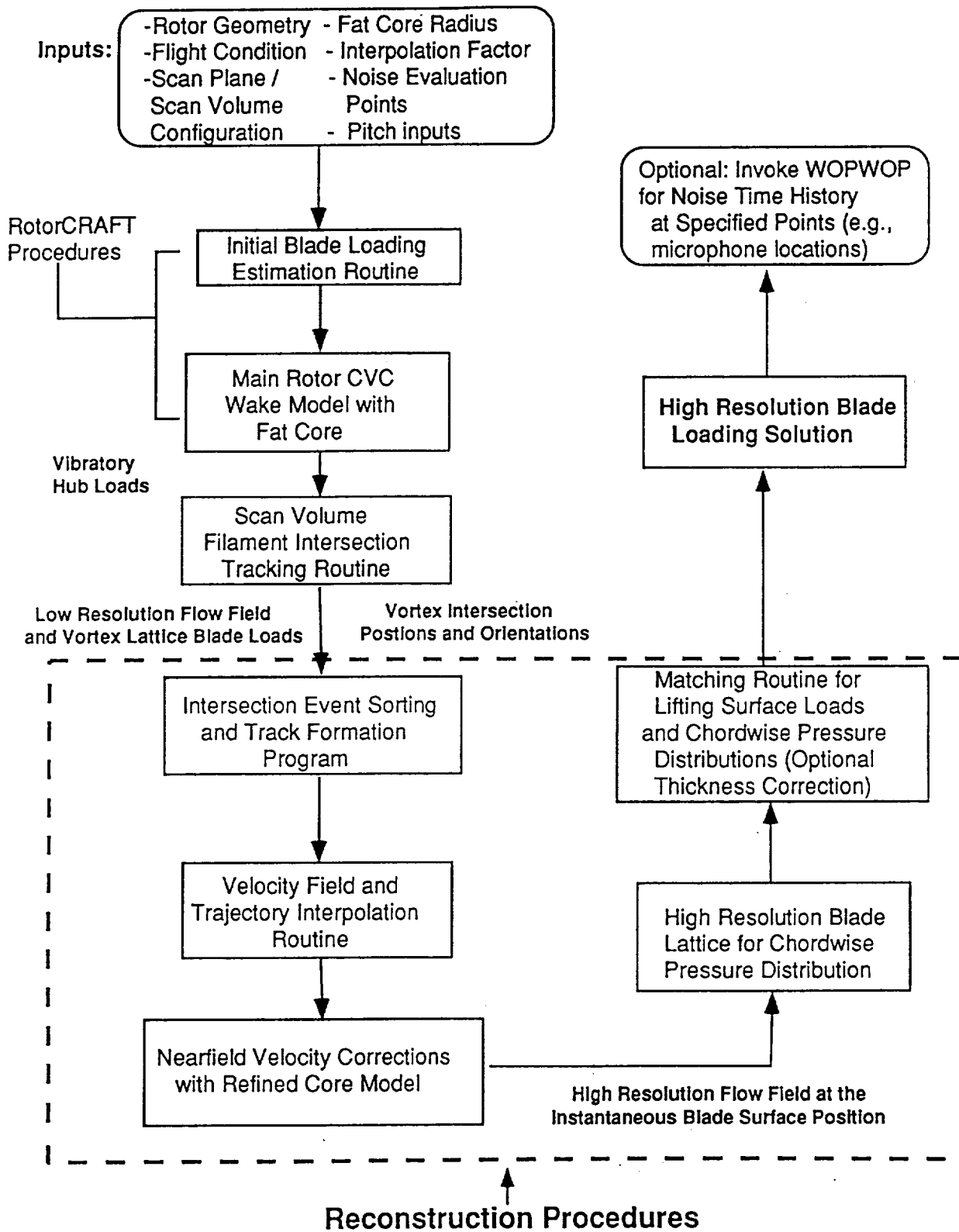
Reconstruction Procedures

Figure 2-1. Flow chart of the operation of the RotorCRAFT/AA code, highlighting the
reconstruction procedures.

This reconstruction procedure is complex to implement, but once in place it yields not only dramatic reductions in CPU time but also a high degree of flexibility and robustness. Previous methods using approaches superficially similar to that described here have in fact been based on ad hoc treatment of close interaction effects. One of the strengths of the present implementation is that the nearfield velocity corrections are produced by a formal matching procedure similar to the method of matched asymptotic expansions. This method is one application of the technique known as Analytical/Numerical Matching (ANM), an approach to problems in vortex dynamics described in several recent papers (Refs. 16-18). The discussion in the next section briefly summarizes the application of ANM in this context.

2.2 Application of Near Field Corrections via ANM

As noted above, the numerical free wake velocity field first is smoothed with an artificially fat vortex core when velocities at the points in the evaluation region are computed. Because this smoothing produces very gradual variations in velocity, only relatively few calculation points are required to reconstruct this velocity field accurately in the designated region of interest. The fat core smoothing is used only to calculate wake effects at the evaluation points, whereas the actual core is used when calculating velocities on the wake itself. This means that the vortex filament motions are still being accurately computed.

Given the geometry and trajectory of the filaments, an analytical solution is then developed based on the nearfield filament configuration. This solution incorporates the local position and curvature of the filament modeled as a parabolic arc. Actually, to compute the correction term that removes the error introduced by using the fat core, two such analytical solutions are superimposed. One solution adds the contribution of a vortex filament with a physically realistic core, and the other solution subtracts a vortex filament with the same fat core used in the numerical calculation. The net effect in the near field is to cancel the numerical fat core effect and add the effect of the actual core size. At the same time, the far field effect remains unchanged since the two portions of the analytical solution cancel in the far field. The superposition of analytical and numerical solutions is shown in Figure 2-2.

Typically, "fat" vortex cores are at least three to four times the size of the baseline "actual" core (see Section 2.5). The numerical smoothing is achieved by use of a particular vortex core model chosen for its ease of implementation, smooth behavior, and its functional simplicity. In its two-dimensional form, the vortex swirl velocity is expressed as $v_\theta = (\Gamma/2\pi)r (r^2 + r_c^2)^{-1}$ (i.e., what is conventionally termed a "Scully core"). For small r ($<< r_c$) the velocity behaves as if in solid body rotation, whereas for large r ($>> r_c$) the velocity behaves as an irrotational point vortex. When velocities are computed in the evaluation region, r_c is replaced by r_f, where r_f is a fat core radius to provide smoothing; for all other velocity calculations a physically realistic value of core radius r_c is used.

It is important to note that this choice of a vortex core model was not intended as an accurate description of the core flow field, but rather as a representative model suitable for use in demonstrating the analysis. The "actual" vortex core sizes were chosen to be typical of those visualized or inferred from flow field data in the literature. One of the strengths of the reconstruction approach implemented here is that the nearfield solution can take nearly any analytical form. Even relatively complex local flow fields representing, for example, a multilayer laminar/turbulent core structure may be built into the nearfield solution without impairing the computational efficiency of the method.
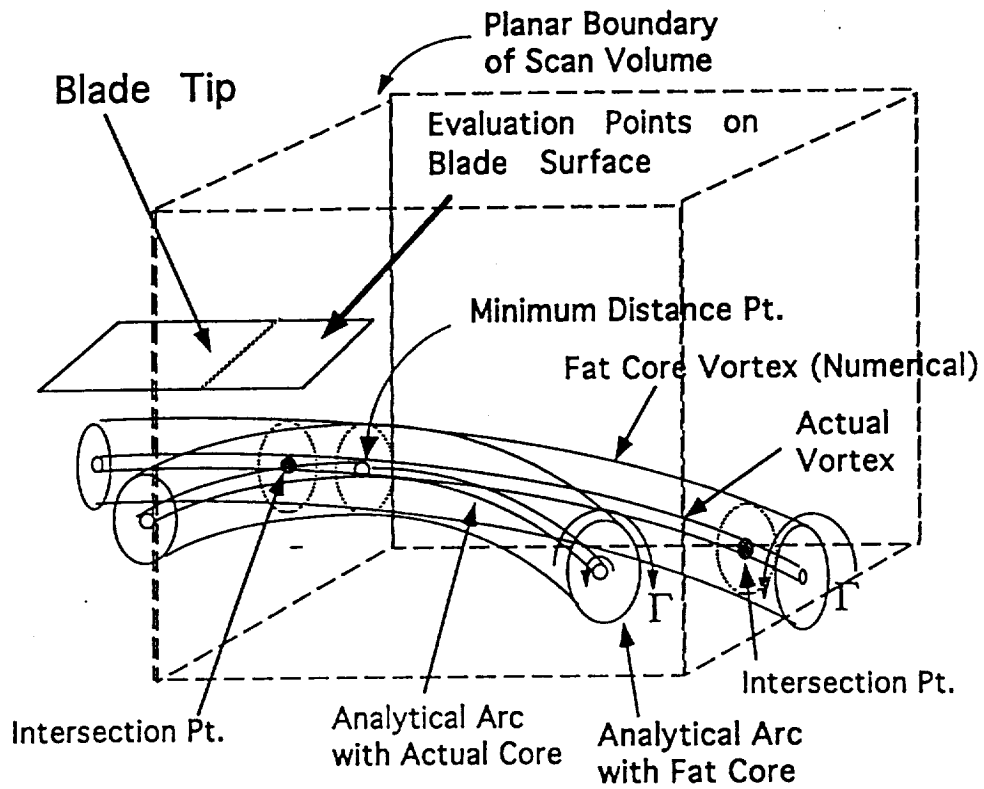
9

Figure 2-2. Schematic of overlapping vortex core models in the application of ANM to flow field reconstruction: close passage to blade tip.
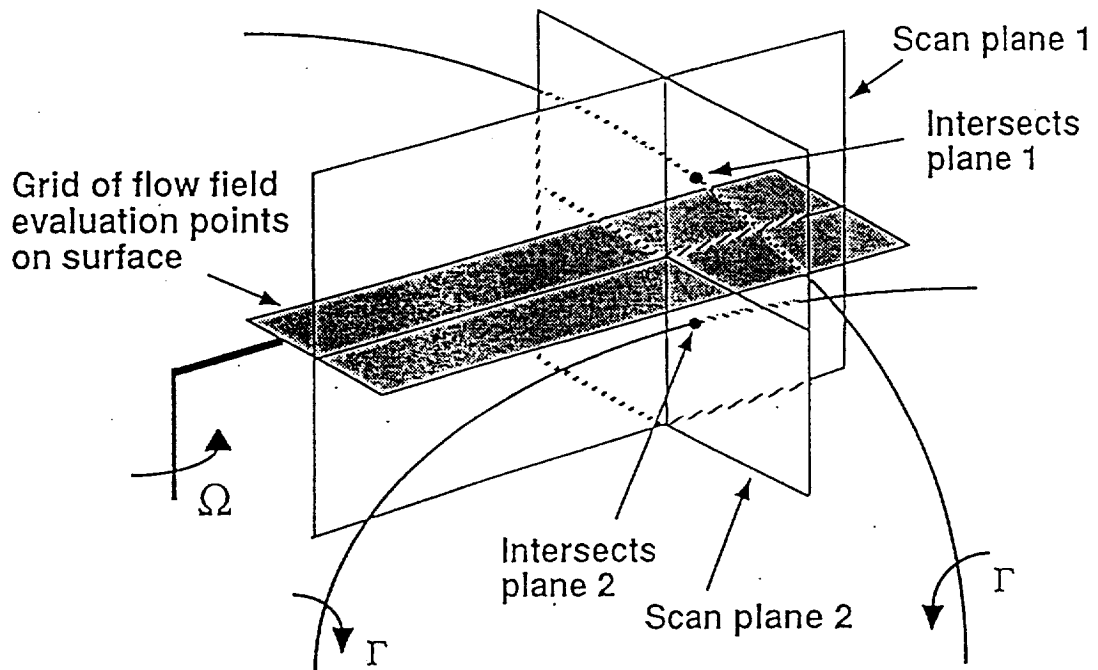

Figure 2-3. Typical orientation of scan planes relative to the rotor blade in the Phase I vortex tracking algorithm.

Implementation of such a core model is discussed in Section 4, which also describes how this treatment interfaces with the existing core model in the CVC wake.

2.3 Examples of Flow Field Reconstruction

Reference 1 described several preliminary applications of flow field reconstruction to representative main rotor systems. This work involved test calculations on representative rotors and evaluation points on and near the main rotor blades. These calculations produced generally very favorable results, demonstrating effective time interpolation factors of up to 4:1 using fat cores three times larger in radius than the nominal actual core radius of .02R. Very accurate reconstruction of downwash velocity fields was obtained for both three- and four-bladed rotors at advance ratios ranging from 0.14 to 0.39. Since good airload correlation had been achieved for both of the rotors examined (the main rotors from the SA-349 Gazelle and the H-34 described in Refs. 19-21), it was inferred that the reconstructed velocity fields would closely parallel reality, assuming that the good airload correlation would carry over into the modeling of the induced velocity field.

One difficulty that was observed, however, was that the computations proved somewhat sensitive to the location and orientation of the scan planes which were used to capture vortex passage events. A typical implementation of these scan planes is shown in Figure 2-3. While this orientation would capture many realistic interactions, it did not prove to be sufficiently robust, producing some results where the quality of the reconstruction was excessively sensitive to the relative location of the scan planes at the points of evaluation. Figure 2-4 shows one such result, specifically the original and reconstructed velocity field at two points along the span of the H-34 main rotor. In this case, the scan planes were set up as suggested in Figure 2-3, mutually perpendicular and with the planes intersecting at r/R = 0.9. Figure 2-4 shows that the reconstruction of the induced velocity field is good at this location, but deteriorates farther inboard (Fig. 2-5). This indicates an undesirable sensitivity of the reconstruction to the scan plane location. To remedy this, a more general approach involving a "scan volume" was implemented.

This approach involves setting up a rectangular box enclosing the rotor blade to capture the vortex intersection events. During the calculation, the wake filaments are tested for any penetration of the scan volume surface as well as for being enclosed within the volume. The shortest distance of an enclosed filament arc to a given evaluation point (typically located on the blade surface) is determined, and the geometric properties of the corresponding vortex element are recorded for use in subsequent reconstruction Unlike the intersecting scan plane method, which captures only the position of vortex intersections and local filament curvature, the scan volume approach stores additional information about the geometry of 3D arcs near the blade and executes a more refined reconstruction based on this information.

Test calculations were set up to exercise the scan volume method on a four-bladed rotor at advance ratio 0.4. The particular rotor configuration used here was a Eurocopter Puma, a rotor with a radius of 24.8 ft., a constant chord of 1.98 ft., and -12 deg. of linear twist. The rotor was operated at a thrust coefficient of 0.007. The particular details of the operating condition were not judged to be critical, however, since the primary aim of this exercise was to produce a challenging test for the wake capturing tools used here.

For the purpose of these computations, the wake code was forced to use single, rolled-up tip filaments, using only a very short CVC wake for the moment (see Fig. 2-6). (Note: because of the overlap near wake model used in this analysis, the blade does not "see" the multiple filaments trailed in these figures; also, in these figures, the free stream
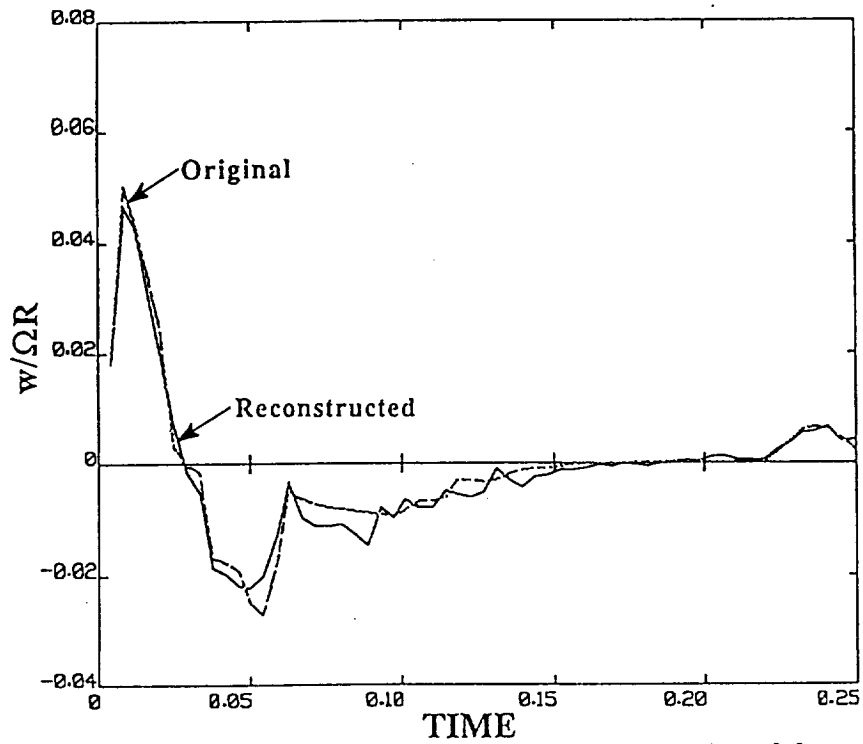
Figure 2-4. Original and reconstructed downwash velocities at r/R = 0.9 over one blade revolution on the H-34 rotor at advance ratio 0.39 : 4:1 time interpolation used in reconstruction.
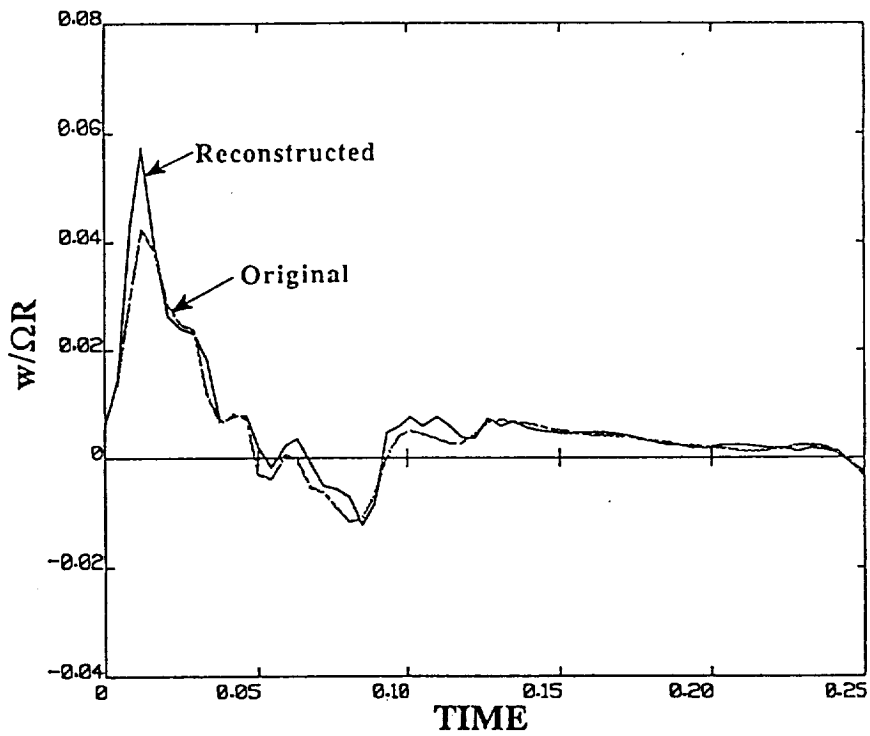

Figure 2-5. Original and reconstructed downwash velocities at r/R = 0.7 over one blade revolution on the H-34 rotor at advance ratio 0.39 : 4:1 time interpolation used in reconstruction.
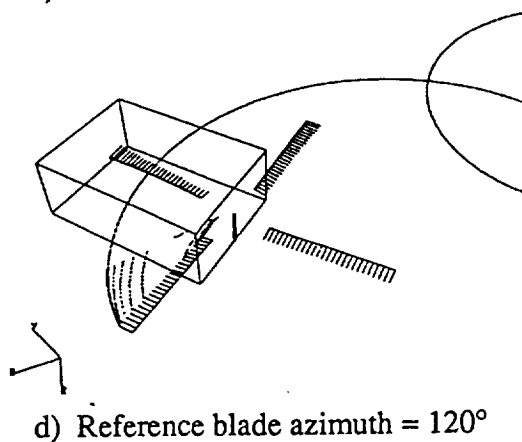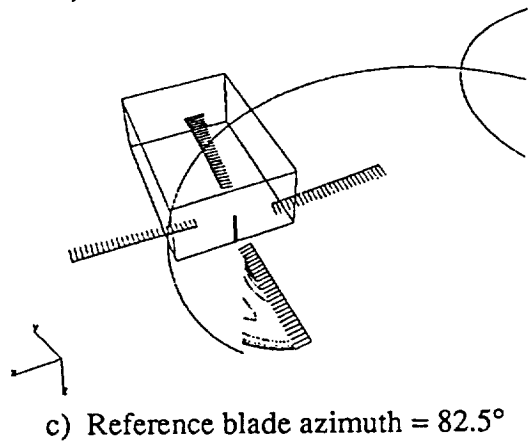
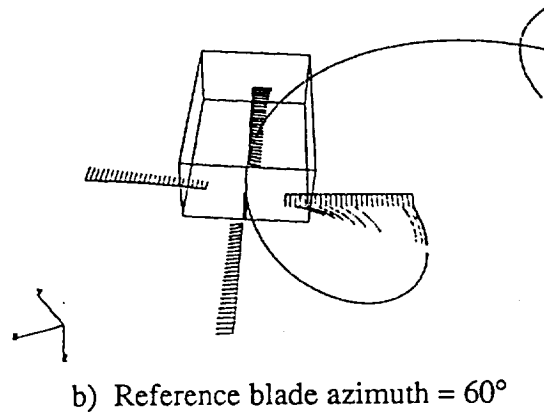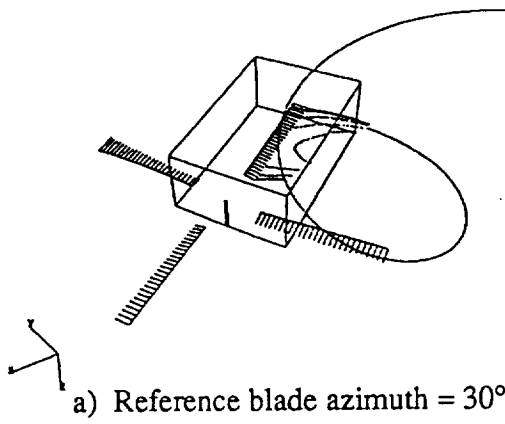a) Reference blade azimuth = 30°

b) Reference blade azimuth = 60°

c) Reference blade azimuth = 82.5°

d) Reference blade azimuth = 120°

Figure 2-6. Representative schematics of the scan volume used to capture blade/wake interactive events; typical tip vortex interactions are shown.

13

runs opposite the local X axis). This was done because the presence of a single, small-core tip vortex trailing from a rotor blade - while nonphysical in many cases - in fact poses a more difficult challenge for the reconstruction procedure because the maximum bound circulation on the blade is concentrated in this filament, making any errors in locating the vortex or applying nearfield velocity corrections particularly evident. Figure 2-6 shows several of the typical close BVI events that occur in forward flight, as well as the scan volume used to capture the position and orientation of the filaments relative to the blade.

Now consider the induced velocity distributions for this case, shown in Figure 2-7. These compare the results obtained using a rotor computation with 144 steps per revolution (2.5 deg. per step) with those obtained with 48 steps per revolution (7.5 deg. per step). Clearly the 48-step case (applied with no reconstruction) misses many velocity peaks and would not produce the same high-frequency loading signature as the 144 step computation.

Consider next the results shown in Figure 2-8, which also takes a low resolution wake geometry solution -using 24 time steps per revolution- and applies reconstruction with a time interpolation factor of 6.0 to predict a high resolution velocity field. Plotting the results with the high resolution reference case of 144 time steps per rev makes it evident that reasonable accuracy is achieved in the reconstruction, however some of the peaks of the induced velocity are not properly recovered. The ability to carry out this 6:1 reconstruction is very beneficial in computation time, since a CPU reduction of approximately a factor of almost 200 can be realized with this approach.

Obviously, the maximum CPU savings are obtained if as few steps as possible are used in the low-resolution initial run. Figure 2-9 shows the results achieved using 48 steps per rev to define the low-resolution wake geometry. In many respects, the results are substantially improved, indicating that a minimum number of steps is in general necessary to obtain good resolution of all components of the induced velocity. During Phase I, some preliminary calculations suggested that it would only be necessary to use 20-30 time steps per revolution to set up the wake geometry, and this may indeed be adequate in some cases. However, additional investigation has indicated that 40-50 steps may be more appropriate from the point of view of guaranteeing robust, accurate results. This judgement is reflected in the cases examined in Section 7. In addition, the need to run with relatively large numbers of time steps in the low resolution case motivated the incorporation of accelerated vortex wake models, to be discussed in Section 3.

In sum, all three components of velocity in Figure 2-9 are well reconstructed, with only minor deviations. The ability to carry out this 3:1 reconstruction is very beneficial in computation time, since a CPU reduction of approximately a factor of 25 can be realized with this approach. A particularly important aspect of these results is that even the very sharp peaks associated with the close encounter of the rotor blades with highly rolled-up tip filaments are captured. The application of the scan volume approach described earlier has made this possible, reflecting a considerable improvement in the performance of the reconstruction algorithm relative to the Phase I code described in Reference 1 and to versions used earlier in the present effort.

2.4 Reconstruction of Airloads

The discussion to this point has focused on the reconstruction of flow fields without directly addressing the application to airload calculations. The prediction of aerodynamic loading in RotorCRAFT/AA is at present handled primarily through the application of a quasi-steady vortex lattice model, with nearfield unsteady wake
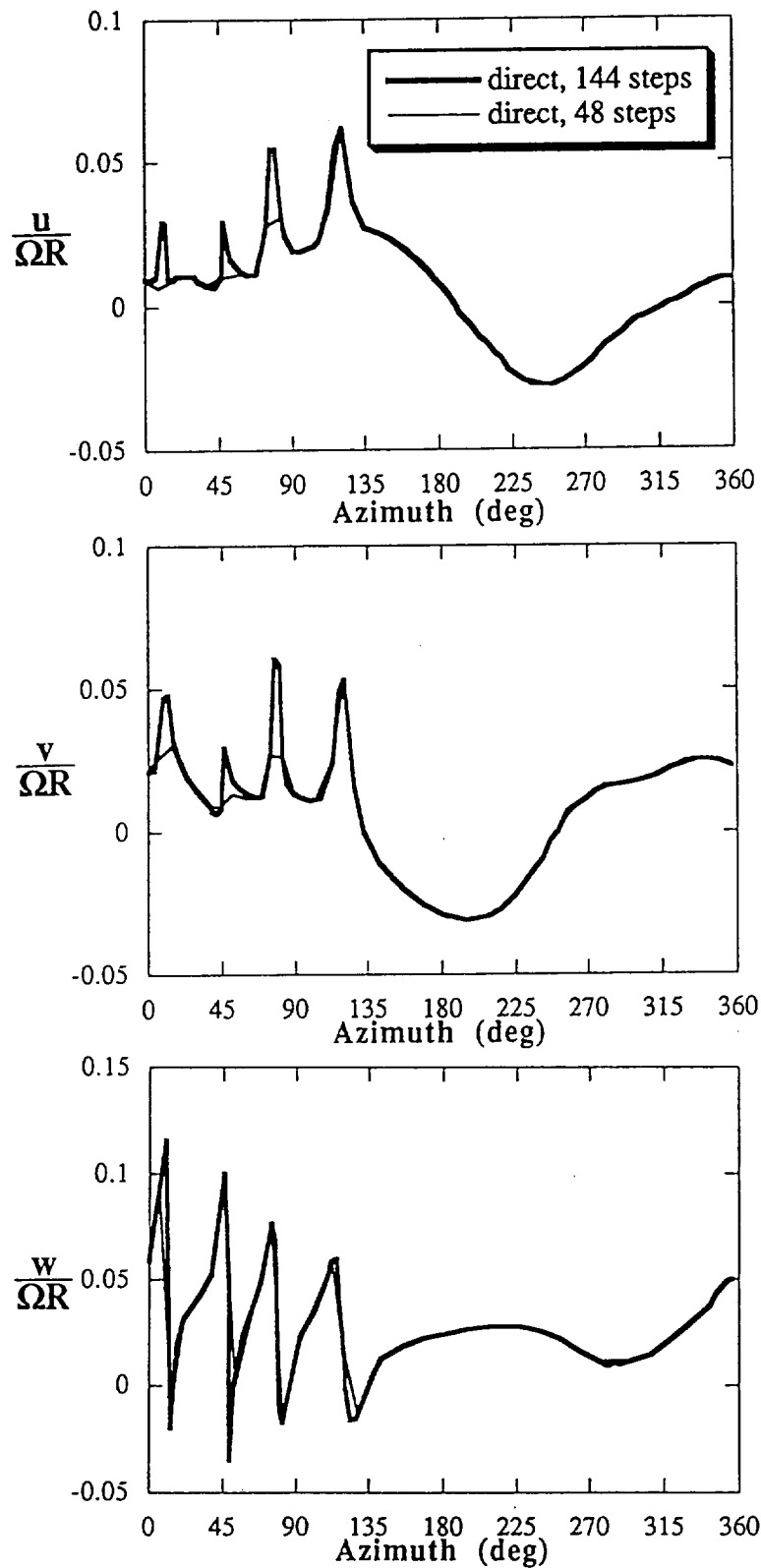
14

Figure 2-7. Comparison of direct velocity predictions for three components of induced velocity at r/R = 0.5 on the Puma main rotor: 48 time steps compared to 144 time steps.
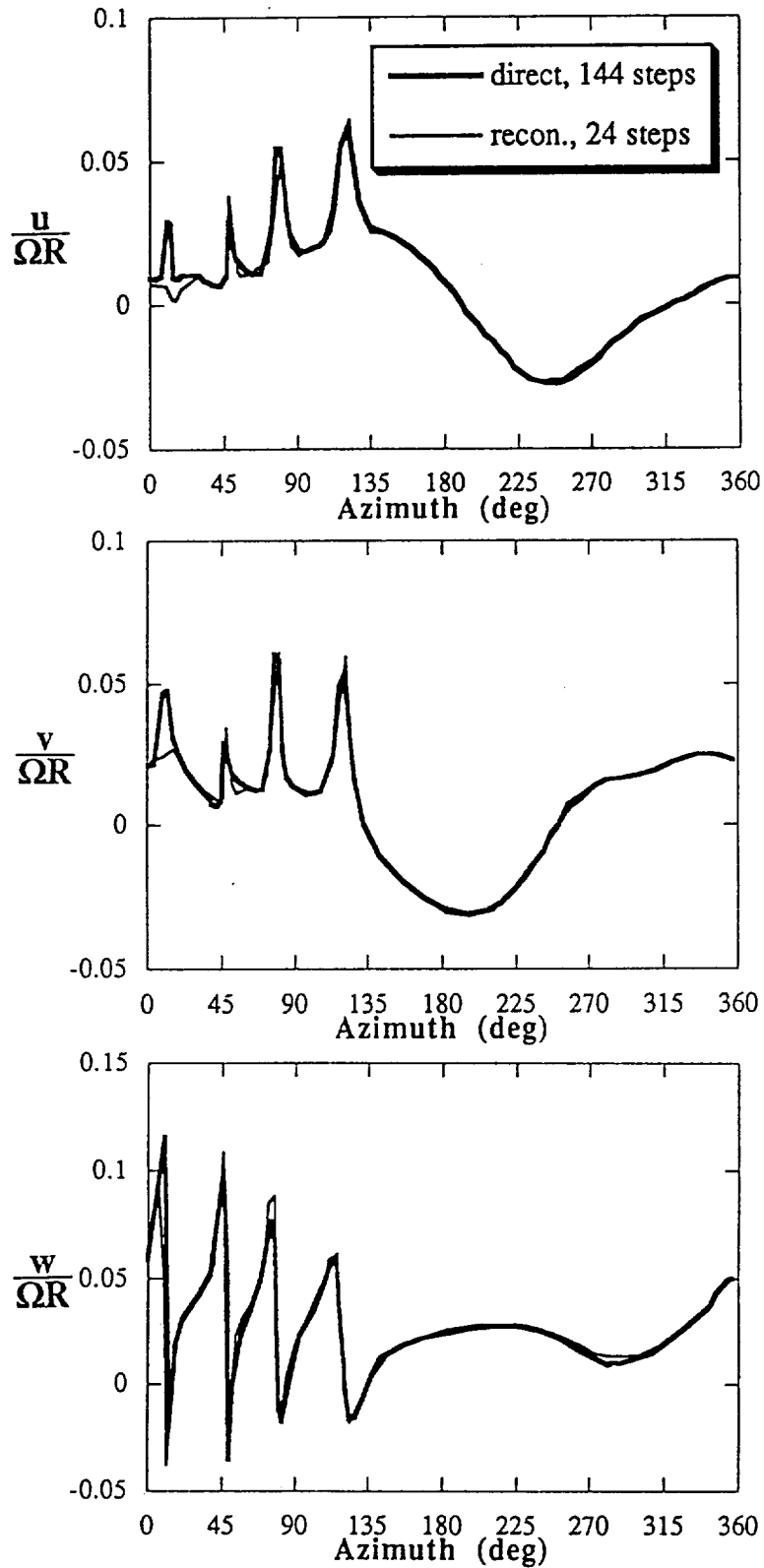
Figure 2-8. Comparison of direct velocity predictions using 144 time steps to the reconstructed velocity based on 24 time steps in the low-resolution solution.
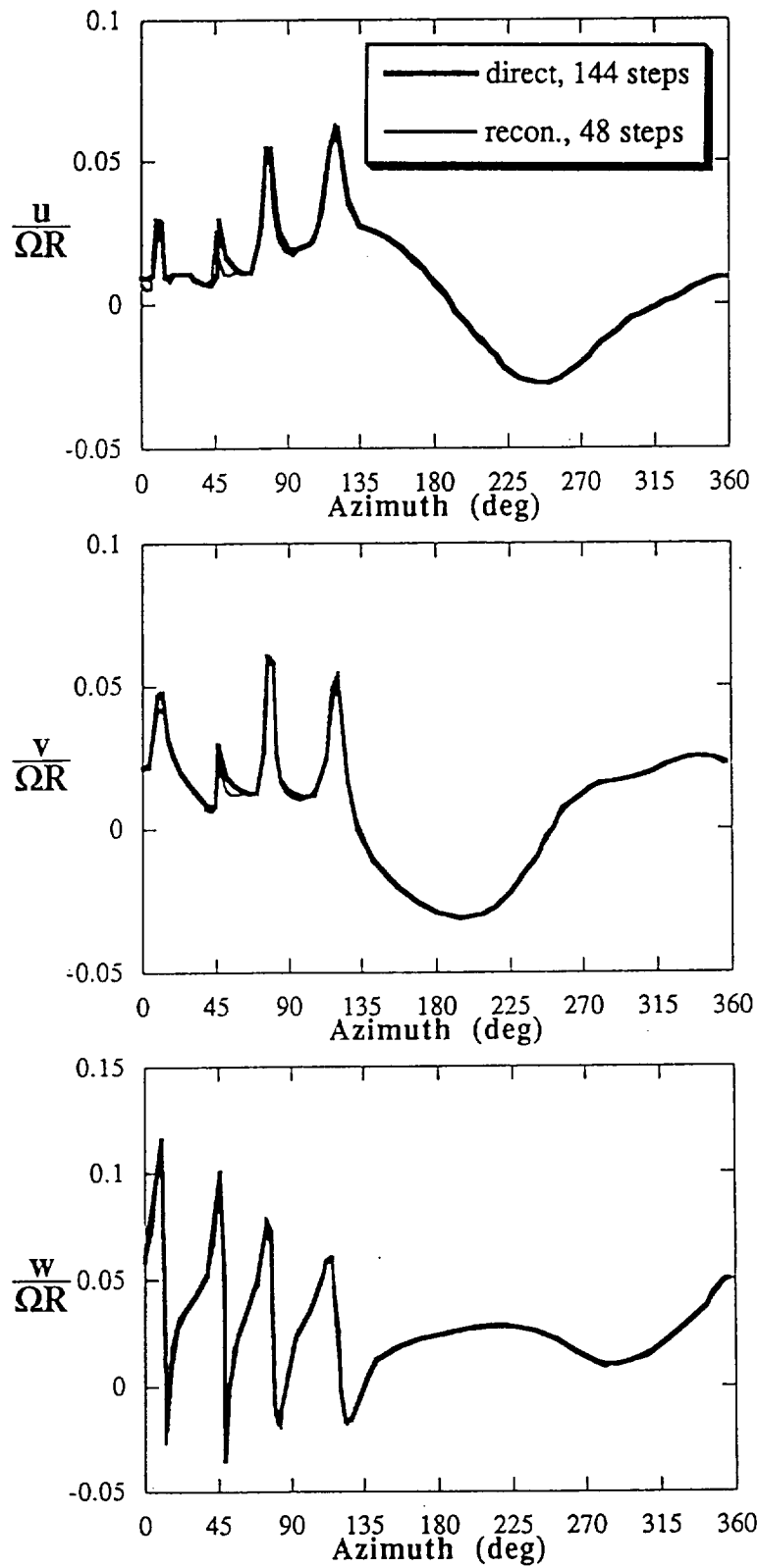
16

Figure 2-9. Comparison of direct velocity predictions using 144 time steps to the reconstructed velocity based on 48 time steps in the low-resolution solution.

17

corrections to account for rapid gradients in loading. Since such models depend directly on the predicted induced velocity field to compute the loading, good performance in velocity field reconstruction can in general be taken to presage similar performance for airloads.

Test cases were run to verify this, though these will not be presented here, since the data correlation studies given in Section 7 will serve this purpose. During this process, though, other features came into focus that were required to ensure a consistent reconstruction. As noted above, the reconstruction process involves linearly interpolating the positions of vortex filaments to account for their motion relative to the evaluation points. In the flow field computations above, these points were either fixed or moved in a prescribed manner on a rotating "pseudo-blade" occupying the same location in space as the blade itself. In airload calculations, the blade surface itself is typically moving in a much more general fashion than rigid rotation, since fully coupled lag, bending, and torsion motion may be taking place. In such a case, the positions of the flexible blade surface must also be interpolated to a time resolution level appropriate for the reconstruction problem.

2.5 Additional Comments on Reconstruction

As has been clear to this point and as will be illustrated further in Section 7, the basic scheme of reconstruction has been quite successful. Dramatic reductions in computation time have been achieved with a high degree of robustness in terms of the ability of the vortex tracking algorithms to correctly reconstruct a wide variety of incident velocity and vorticity fields. This section summarizes information obtained to date regarding parameter selection within the code as well as a discussion of the implementation of the present model and its limitations.

First, as to the selection of the fat core radius, the considerations to bear in mind are that the core must be large enough to meaningfully smooth blade/wake interactions to the point where a blade time step at the rotor tip traverses roughly one fat core radius. For a representative low resolution run involving 48 time steps per revolution, this suggests a fat core radius of approximately $2\pi R/48 = 0.13R$. Since typical vortex core radii for tightly rolled-up vortices are in the vicinity of 1-2% of radius, this implies a fat core multiplier of roughly 10.

Second, a clarification of the exact role of the fat core model is in order. The baseline 'actual core' in the CVC wake model is used to compute the wake-on-wake interactions of the filaments, so that the artificial smoothing in the fat core does not affect the evolution of the wake. Moreover, the velocity induced by the smoothed fat cores on the blade is in fact computed on a companion pseudo-blade coincident with the "real" blade used in the computation. The "real" blade sees the induced velocity field of the baseline actual cores, and therefore produces a blade motion solution consistent with this velocity field. This is an important step, since this blade motion solution is used in the reconstruction analysis, as discussed in Section 4. The smoothed velocity field on the pseudo-blade is stored and used as the starting point of the reconstruction analysis.

Third, the maximum time interpolation factor that can be used has not formally been determined, though numerical experimentation to date indicates that a factor of 30:1 is achievable with the current analysis. Flow field reconstruction computations in Phase I routinely operated at factors of 3:1 or 4:1, but these relatively low multipliers were chosen in part because validation of the interpolated results could not conveniently be done, due to the large CPU investment necessary to obtain a high-resolution result.

18

However, computations during the present effort have routinely been performed with reconstruction multipliers between 8:1 and 20:1 with no apparent anomalies. Many of the computations carried out in Section 7 use an 8:1 time interpolation ratio, which yields azimuthal steps of roughly 1 deg. given a typical low-resolution case involving 48 time steps per revolution (7.5 deg. azimuthal increments). Other computations in Section 7 use factors as high as 20:1, yielding an azimuthal resolution of 0.375 deg.

Finally, it is important to specify a central assumption of the method, namely that the velocity field during the high-resolution reconstruction process is adequately represented by computing the velocities induced by vortices with interpolated positions. Those features of vortex evolution that are not easily captured by such simple interpolation procedures will be lost in reconstruction. In most cases, such errors are judged to be negligible, though in some cases at very low forward speeds, some wake distortion may take place on a time scale that would not be captured by the coarse time-resolution case. In addition, the blade load motion solution is not re-converged in the presence of the high resolution velocity field as part of the reconstruction. Thus an element of consistency may in principle be lost in the final reconstructed solution. However, closing this computational loop is possible and in fact a desirable objective of follow-on work.

3.0 ACCELERATED VORTEX WAKE MODELING

Section 2 has described the reconstruction strategy pursued in the current effort and documented the dramatic reductions in CPU time that it makes possible. The basis for this strategy is using a free wake run with the CVC model with relatively low temporal resolution to set up the incident wake geometry in those regions where high-resolution results for the flow field and airloads are required. However, in some cases the initial run with low temporal resolution itself can be moderately computationally intensive, particularly if it is desired to use a large number of vortex elements to provide high spatial resolution of the wake. Thus it was judged appropriate to focus additional effort on simplifying and accelerating the basic free wake model, since this would yield increments in computational efficiency over and above the gains realized through the use of reconstruction.

3.1 Simplified CVC Wake Calculations

Two relatively straightforward strategies were pursued within the basic CVC wake calculation itself to enhance its computational efficiency. The fundamental approach to the computation of vortex filament geometry and wake-induced velocity is the 'direct' Lagrangian wake computation involving the calculation of the full effect of each vortex element on every other vortex element in the wake. The implementation of this approach and various methods for reducing the CPU demands of the full free wake computation are discussed in Reference 3; details of its implementation are given in Reference 22. These include the various approximate models of the far wake, such as collapsing the CVC filaments into single free vortices, and/or then approximating these free vortices by semi-infinite prescribed filaments.

One option made available as part of the present effort involved implementation of an optional time stepping scheme that can replace the default integration scheme, a predictor-corrector method drawn from Reference 23. This scheme is presently used to advance the position of each collocation point in the wake x_i based on the wake-induced velocity v_i. The current scheme involves the following steps to advance from the nth to the n+1st time level:

Predictor: $$\vec{x}_i^{*n+1} = \vec{x}_i^n + \vec{v}_i(\vec{x}_i^n)\Delta t \qquad (3\text{-}1)$$

Corrector: $$\vec{x}_i^{n+1} = \vec{x}_i^n + 0.5\left(\vec{v}_i(\vec{x}_i^n) + \vec{v}_i(\vec{x}_i^{*n+1})\right)\Delta t \qquad (3\text{-}2)$$

This scheme yields second-order accuracy, but does require two evaluations of the vortex-induced velocity field. An alternative backward difference treatment was tested during this effort that involved a single velocity field evaluation:

Backward Difference: $$\vec{x}_i^{n+1} = \vec{x}_i^n + 0.5\left(3\vec{v}_i(\vec{x}_i^n) - \vec{v}_i(\vec{x}_i^{n-1})\right)\Delta t \qquad (3\text{-}3)$$

Here, the second velocity evaluation is bypassed by using "old" velocity information from the previous time step. Owing to the need for only a single velocity evaluation, this approach requires only half of the CPU used by the predictor-corrector. Moreover, the method is also second-order accurate in time, albeit with a larger constant multiplying the

$(\Delta t)^2$ term. In most cases, this option provides a factor of two acceleration of the free wake computation with very little degradation in accuracy.

Another feature presently available is the restriction of the domain of the application of the full wake-on-wake velocity computation. Such interactions are typically quite important in the immediate vicinity of the rotor disk, and should be retained for cases at low to moderate advance ratio or high thrust. However, for higher forward speeds, the wake distortion can be ignored for points sufficiently far from the rotor blades. Thus, a second option tested during the present effort removed wake-on-wake velocity computations for points downstream of the main rotor disk. This option has been found to be most appropriate for advance ratios above 0.2; in such cases, the typical reduction in CPU has been up to roughly a factor of two, though the exact result will vary as a function of other wake acceleration features used in the model.

3.2 Fast Vortex Computations

The basic computational tool in all of these computations is the parabolic Basic Curved Vortex Element, or BCVE (Ref. 24). Over the last ten years, the BCVE has proved to be an exceptionally efficient and accurate tool for vortex wake computations, superior to the straight line vortex elements it replaced. However, its high accuracy is useful primarily in near-field interactions; for distant interactions, it is possible to replace it by much simpler models that require less CPU time. Moreover, an appropriate choice for such a model is the vortex particle or vorton (Fig. 3-1); this artifact is particularly amenable to use in reduced-order models that can achieve dramatic reductions in CPU relative to direct calculations. These so-called fast vortex methods are now described.

3.2.1 Background

As noted above, a full free wake calculation results in an N-body interaction problem with an asymptotic time complexity of $O(N^2)$. This is very expensive and usually limits the number of elements used in a calculation to $O(10^4)$. Recently, Leonard and a co-worker (Ref. 25) addressed this problem for 2D computations, developing a fast two-dimensional vortex method where the vortex particles are clustered into groups and the interactions between well-separated groups are simplified using a far-field approximation. In their calculations, a grid of boxes is superimposed on the flow domain, and vortex particles which reside within the same box are clustered into groups. The interactions between particles which are from the same group or immediate-neighboring groups are treated using an exact pair-wise interaction. However, in considering the far-field effects, an approximate group-to-group interaction is used. For example, given two groups A and B (see Fig. 3-2), to compute the induced velocity of group A on group B the inducting effect due to group A is computed as a truncated multipole expansion. This is evaluated at the centroid of group B and a Taylor series is used to extrapolate the velocity at each vortex location within group B.

This method is highly accurate and provided that the two groups are well separated (i.e., r>D, where r is the separation distance between the two groups and D is the diameter - or characteristic dimension - of the inducting group) the multipole expansion converges (Ref. 26). Using such far-field group-to-group approximations, considerable savings in computational time can be achieved. In particular, for large N and M, where N is the number of vortex particles and M is the number of groups (boxes), the time complexity of the method becomes independent of the number of groups and is $O(N^{4/3})$.
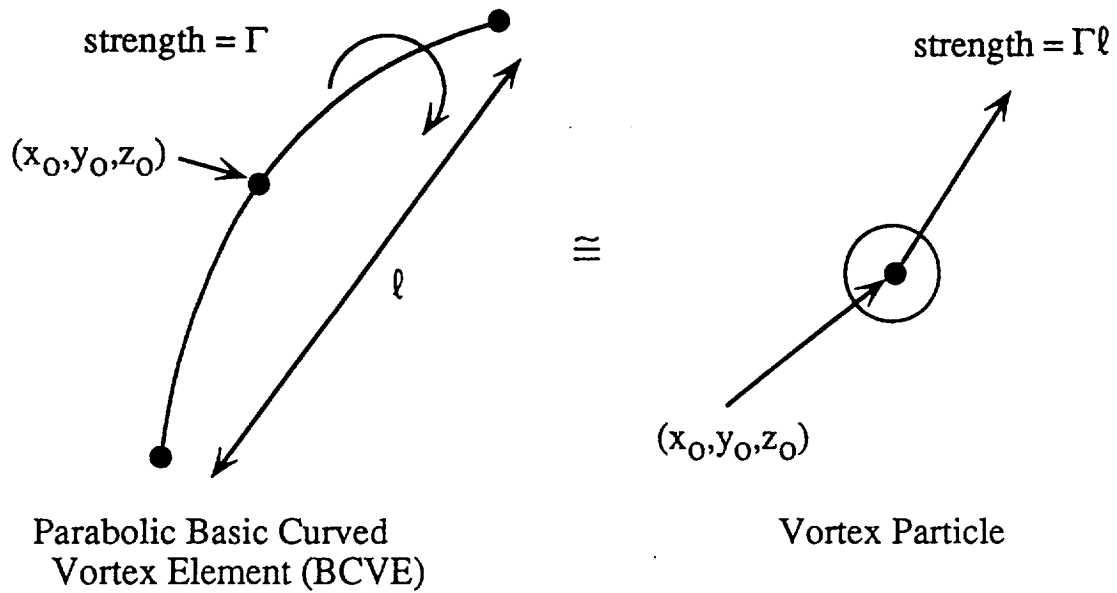
21

Far far-field interactions:

strength = Γ

(x_0,y_0,z_0)

ℓ

$\cong$

strength = $\Gamma\ell$

(x_0,y_0,z_0)

Parabolic Basic Curved
Vortex Element (BCVE)

Vortex Particle

Figure 3-1. Approximations of BCVEs by vortex particles for far-field interactions.

Taylor series expansion about
centroid of vorticity

group B vortices

group-to-group interaction

multipole expansion about
centroid of vorticity

group A vortices
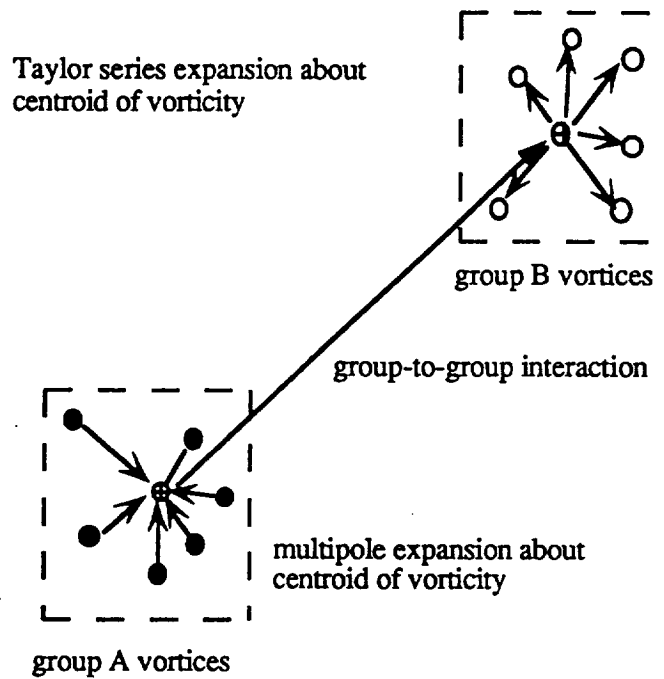
Figure 3-2. Schematic showing far-field group-to-group interaction for the fast
vortex method.

In the present effort, we have applied an extended version Leonard's two-dimensional fast vortex method for the three dimensional flow field around the rotor, invoking an arbitrary-order multipole expansion of the three-dimensional Biot-Savart law. This has been used in the evaluation of the far-field velocity induction where a point vortex representation yields accuracy essentially equivalent to the BCVE. The induced velocity due to a group of point vortices is in general given by:

$$\vec{u}(\vec{x}) = -\frac{1}{4\pi} \sum_{i=1}^{N} \frac{(\vec{x} - \vec{x}_i) \times \vec{\omega}_i \, \delta v_i}{|\vec{x} - \vec{x}_i|^3} \tag{3-4}$$

where $\vec{\omega}$ and dv are the vorticity vector and the volume (length times cross-sectional area) of vorticity, respectively of the BCVE. A multipole expansion about the centroid of vorticity of Equation 3-4 is carried out. The centroid of vorticity is computed by:

$$\vec{x}_{cm} = \frac{\displaystyle\sum_{i=1}^{N} \vec{x}_i \, |\vec{\omega}_i \, \delta v_i|}{\displaystyle\sum_{i=1}^{N} |\vec{\omega}_i \, \delta v_i|} \tag{3-5}$$

Since both signs of vorticity may be present in the wake, in each locality the vortex elements are clustered into two separate groups, one for the positive-sign (counter-clockwise rotation, seen from downstream of the generating blade) vortices and one for the negative-sign (clockwise rotation) vortices. This is necessary because the centroid of a mixed group of opposite-sign vortices may be at infinity.

For the purpose of illustration, we assume that the centroid of the group of vortices is at the origin. The arbitrary order multipole expansion can then be written as:

$$\vec{u}(\vec{x}) = -\frac{1}{4\pi r^3} \sum_{k=0}^{\infty} \vec{E}_k \frac{1}{r^k} \tag{3-6}$$

$$\vec{E}_k = \sum_{i=1}^{N} C_k^{3/2}(\cos\gamma_i) \, r_i^k (\vec{x} - \vec{x}_i) \times \vec{\omega}_i \, \delta v_i \tag{3-7}$$

where $r = |\vec{x}|$, $r_i = |\vec{x}_i|$, $\cos(\gamma_i) = \hat{e} \cdot \hat{e}_i$, $\hat{e} = \vec{x}/r$, $\hat{e}_i = \vec{x}_i/r_i$ and the coefficients C_k^λ are the Gegenbauer polynomials (Ref. 27) given by:

$$C_k^\lambda(t) = \frac{-1^k}{2^k} \frac{\Gamma(2\lambda+k)\Gamma(\frac{2\lambda+1}{2})}{\Gamma(2\lambda)\Gamma(\frac{2\lambda+1}{2}+k)} \frac{(1-t^2)^{\frac{1}{2}-\lambda}}{k!} \frac{d^k}{dt^k}\left\{(1-t^2)^{\lambda+k-\frac{1}{2}}\right\} \tag{3-10}$$

and Γ is the Gamma function. The use of the Gegenbauer polynomials facilitates the expansion to arbitrarily high order. It is useful to note that the $1/r^2$ Biot-Savart kernel in

23

the induced velocity drops off very rapidly with increasing r, where $r = |\vec{x} - \vec{x}_j|$. Typically, sufficient accuracy can be obtained with two or three terms in the expansion.

In the present effort, three terms, i.e., the monopole, dipole and quadrupole, are kept in the expansion. This makes the evaluation of the vortex induced velocity (which is the bulk of the vortex calculations) extremely efficient. For example, given a group of N tightly clustered vortex elements (e.g., group A in Fig. 3-2) and M observation points where the velocity is to be evaluated, if direct evaluation is made using Equation 3-4, then the summation over N terms in this equation must be evaluated at every observation point, resulting in NM evaluations (as in the classical N^2 method). However, if we assume that the evaluation points are well separated from the group of vortex elements, then the far-field approximations given by Equation 3-6 can be used. In Equation 3-6, the coefficients $\vec{E}_k$ can be further manipulated to a form which depends on the distribution of vorticity only (i.e. first moment, second moment and so on) and not on the observation point $\vec{x}$. The evaluations of these coefficients involve N operation counts, but, once computed, they are used for all the evaluation points. The total number of machine operations is therefore N+M, which is considerably fewer than NM, for large N and M.

Using Equation 3-6, the far-field induced velocity due to a group of vortex elements can be computed efficiently. The velocity is evaluated at the centroid of a distant group, as shown in Figure 3-2. The latter can be any group of points where the local velocity is needed, and in the present effort these include wake points, blade surface points and off-rotor flow field evaluation points. The centroid of the group of wake points is computed using Equation 3-5, while the centroids of groups of blade surface points and off-rotor scan-plane points are computed simply by taking the average location of the points within each group.

A further improvement in computational efficiency can be attained by using a Taylor series approximation. To illustrate, let us consider the example given in Figure 3-2, with N vortex elements and M observation points. If we assume that the observation points are also tightly clustered in physical space, then the induced velocity given by Equation 3-6 need only be evaluated at the centroid $\vec{x}_{cm}$ of the group and the velocity at each observation point can be obtained using a Taylor series expansion about the centroid:

$$\vec{u}(\vec{x}) = \vec{u}(\vec{x}_{cm}) + \delta\vec{x} \cdot \nabla\ \vec{u}(\vec{x}_{cm}) + \frac{1}{2!}\left(\delta\vec{x} \cdot \nabla\right)^2 \vec{u}(\vec{x}_{cm}) + ... \qquad (3\text{-}9)$$

where $\delta\vec{x} = \vec{x} - \vec{x}_{cm}$ and $\nabla = \partial/\partial\vec{x}$. In Equation 3-9, the velocity gradients $\partial\vec{u}/\partial x_i$, $\partial^2\vec{u}/\partial x_i\partial x_j$ and so on (here, x_i and x_j denote the ith and jth components, respectively, of the vector $\vec{x}$) are evaluated only once at $\vec{x}_{cm}$ and the velocity at each observation point is obtained through simple multiplication, which is much cheaper than evaluating the terms $1/r$, $1/r^2$ etc. needed in Equation 3-6. Similar to the velocity evaluations, the gradient terms are also approximated using a multipole expansion. In the present effort, because of the fast drop-off of the Biot-Savart kernel, only two terms are kept in the Taylor series expansion.

3.2.2 Vortex Clustering Scheme

In the present effort, a single-level vortex clustering scheme was used. The computational length-scale introduced by the arc-length of the BCVEs, which is much

larger than the core size of the element, sets a lower bound on the size of the group, i.e. the diameter of the smallest group must be greater than the arc-length of each individual element. Therefore, it is judged most appropriate simply to cluster the elements into one set of vortex groups, each of the same size.

Figure 3-3 shows a typical wake/rotor combination to which the clustering scheme must be applied. A fixed grid of cubic boxes is laid over a limited domain in the flow, typically encompassing the rotor diameter in lateral dimension and at least one diameter downstream; the vertical dimension of the wake varies with advance ratio, but one blade radius typically suffices. All curved vortex elements with same-sign circulation and whose mid-points reside within a given box are assigned to the same group. Note that the end-points of the elements may extend beyond the box. However, it is important that the arc-length of the elements be smaller than the size of the box. Figure 3-4 schematically depicts this box geometry around the wake of one blade.

The RotorCRAFT/AA analysis can accommodate any user-selected distribution of boxes. However within the present code, an appropriate default system for setting the size of the boxes has been adopted, as described in Reference 28 and references therein. This default selection has been found to be robust from the point of view of yielding good accuracy while retaining the improvements in computational efficiency characteristic of the fast vortex method.

As an aside, it should be noted that the technology needed for a multi-level, hierarchical clustering scheme has been well proven in related work on vortex dynamics (e.g., Refs. 27 and 29). In those calculations, vortex particles (with no associated length-scale) are used exclusively, though in some cases, a numerical smoothing core - which is of the order of the smallest spacing between elements - is incorporated. (Although the core size introduces a computational length-scale into the calculation, it is chosen to be smaller than the smallest physical length scale which the calculation attempts to resolve). In a typical Lagrangian calculation, the spectrum of length-scales usually spans several orders of magnitude. In cases where calculations are performed only with vortex particles, it is therefore appropriate to use a multi-level, hierarchical clustering scheme such that the interactions between different groups of varying sizes representing various length-scales in the calculation can be treated accurately and efficiently.

3.2.3 Test Results

The fast vortex method has been implemented in the present version of the RotorCRAFT/AA code, and representative rotor configurations have been examined. Three terms are used in the multipole expansion of the velocity induction (Equation 3-6) and two terms in the Taylor series approximation of the induced velocity (Equation 3-9).

Calculations were run to quantify the gains in CPU time using this approach. Figure 3-5 shows a comparison of the CPU time (in seconds) taken per time step to compute the wake-on-wake velocity interactions. The data are plotted against the number of vortex elements in the wake. In the calculations using the classical N^2 Biot-Savart summation (square), because of the quadratic dependence, the CPU requirement increases rapidly with increasing number of elements. In the fast vortex calculations (triangle), the N-dependence is much weaker and the increase in CPU requirements is considerably slower. With a total number of elements of about 2500 (representative of a typical forward flight condition), the fast method is roughly three times as fast as the classical method.
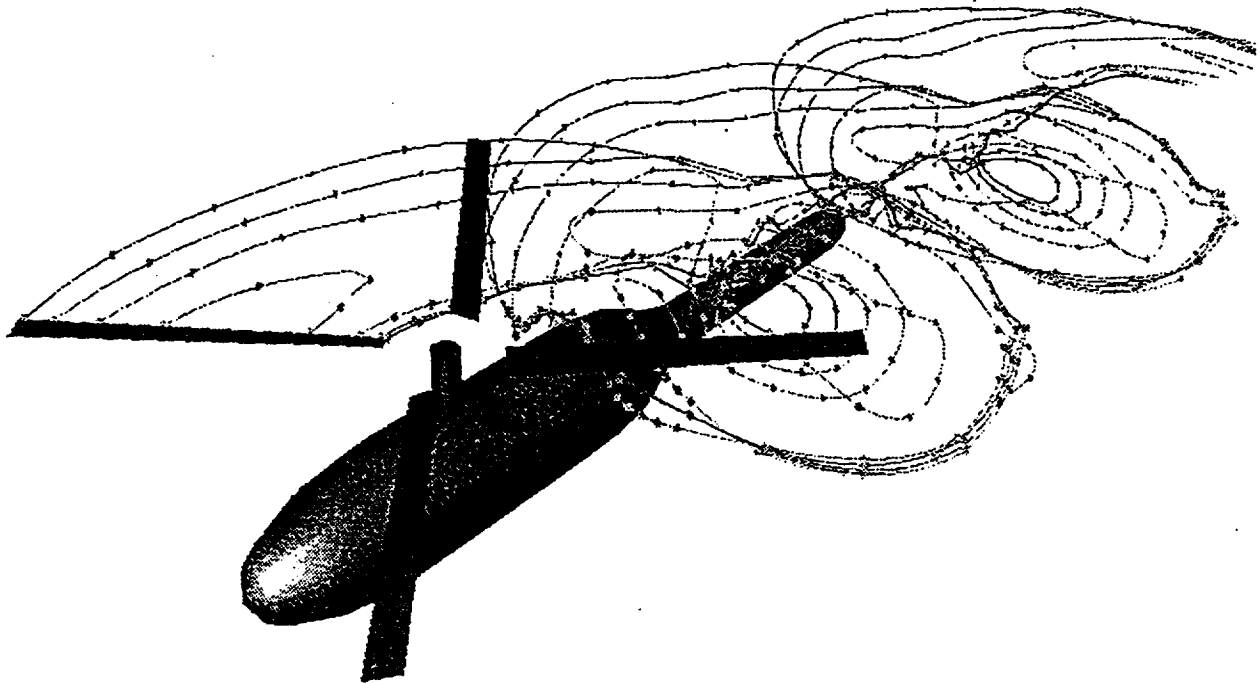
Figure 3-3. Schematic showing a model-scale helicopter flow configuration composed of a fuselage, a four-bladed rotor and a trailed CVC vortex wake.
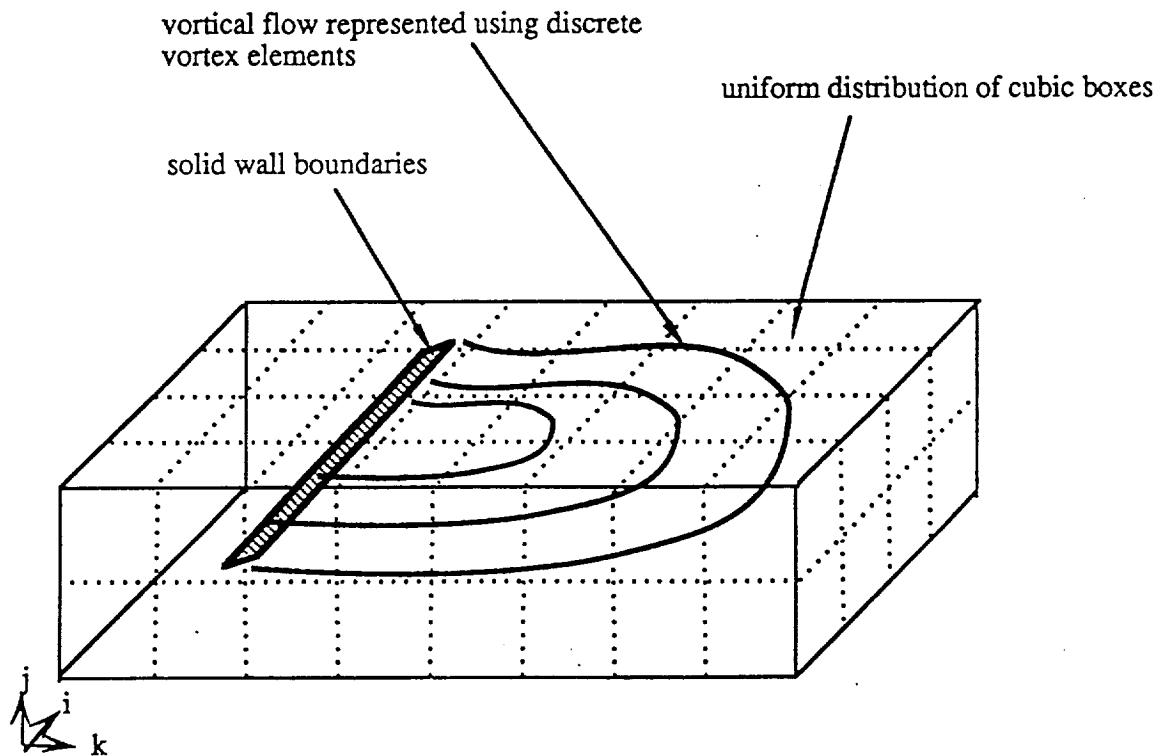

Figure 3-4. Schematic showing fixed grid of cubic boxes which encompass a blade and its trailing wake.
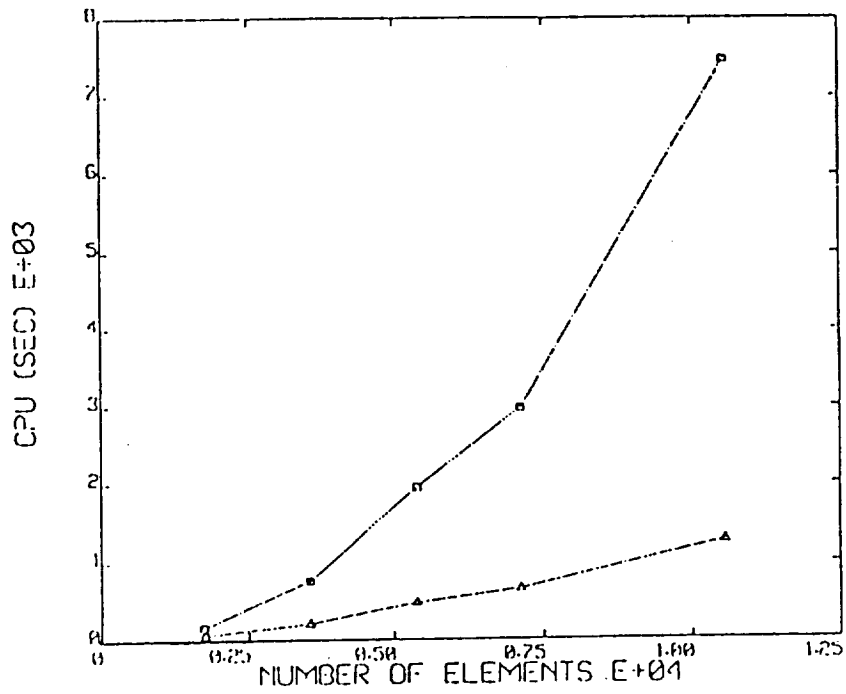
26

Figure 3-5. Comparison of computation time (sec) for the wake-on-wake interaction, using fast vortex method - △ and direct summation - □ .
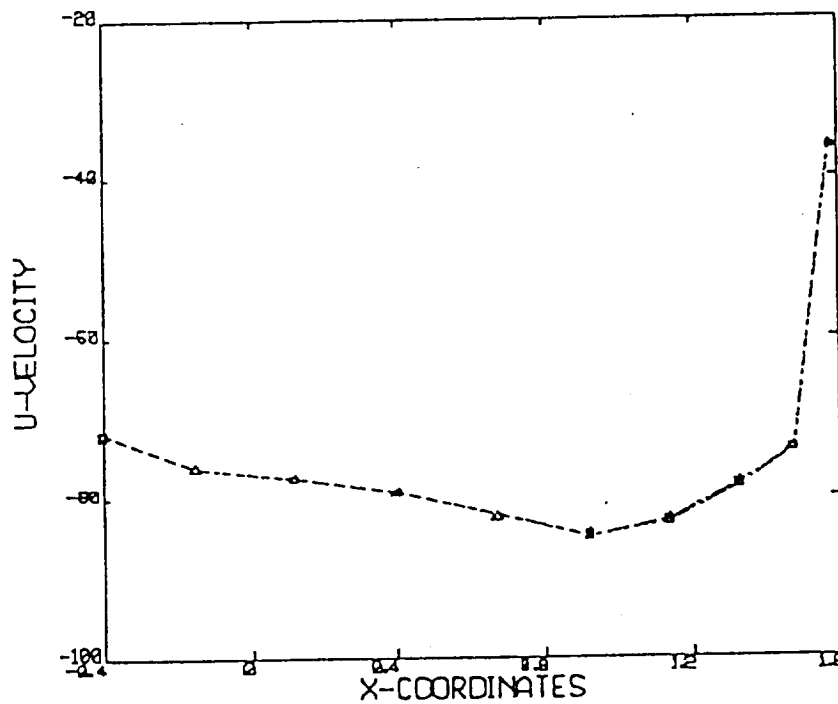

Figure 3-6a. Comparison of u-velocity on fuselage computed using fast vortex method - △ and direct summation - □ .

27
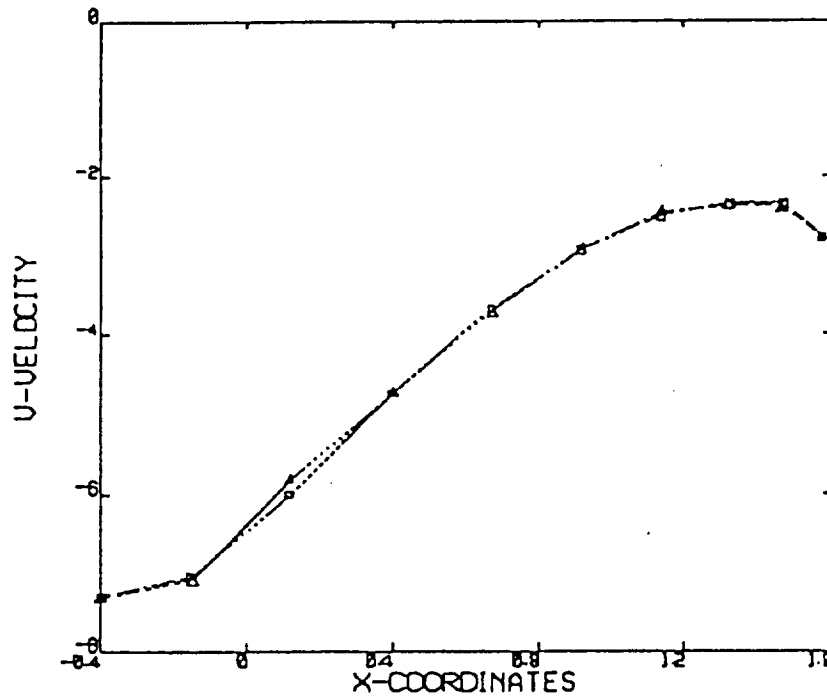
Figure 3-6b. Comparison of v-velocity on fuselage computed using fast vortex method - $\triangle$ and direct summation - $\square$.
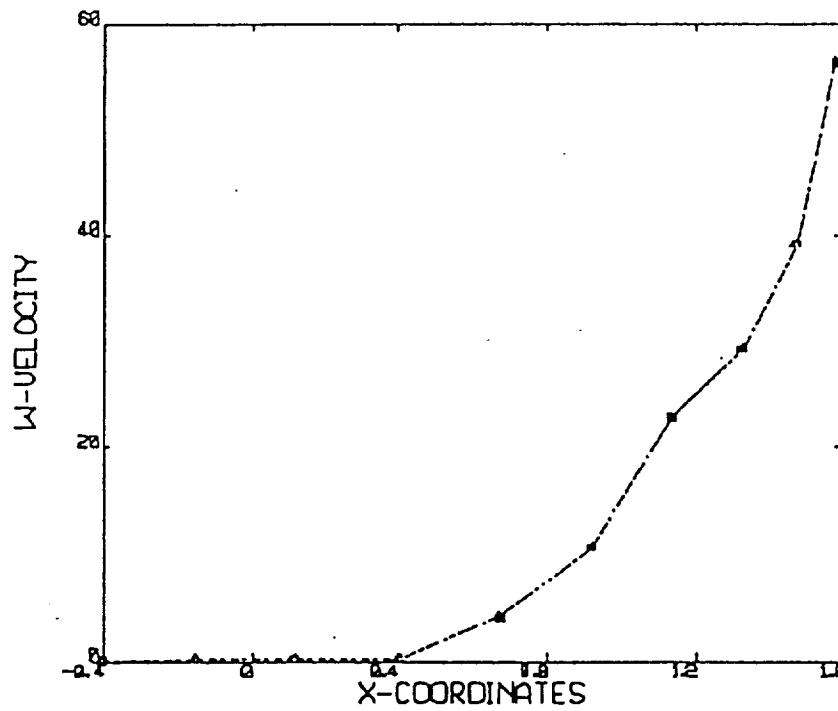
Figure 3-6c. Comparison of w-velocity on fuselage computed using fast vortex method - $\triangle$ and direct summation - $\square$.

28

However, it is important to note that the improvement in computational efficiency of the fast method increases dramatically as the number of elements is increased. From the standpoint of executing calculations with the rotor operating at low advance ratio, this is particularly attractive. A dramatic reduction in CPU time is observed for calculations at low forward speed where several thousand computational elements are typically required.

As to the accuracy of the fast vortex treatment, Figure 3-6 shows the comparison of the velocity components computed using the classical N^2 Biot-Savart summation (square) and the present fast vortex method (triangle) computed at points along the x-axis on the top surface of a fuselage immersed in a helicopter rotor wake (Ref. 28). The fuselage used for this test case was the forebody of the University of Maryland fuselage (Ref. 30). Approximately 1500 curved vortex elements are used in the wake representation and a grid of 180 (15x6x2) cubic boxes is laid in the flow domain. This grid completely covers a physical domain which contains a four-bladed rotor, a body of revolution representing the fuselage, and a free wake consisting of three turns of eight filaments, each filament consisting of 72 curved elements.

Figure 3-6 shows comparisons of the three wake-induced velocity components u, v and w, respectively, on the top of the fuselage. The agreement between the two calculations is very encouraging. This is especially true for the u- and w-velocity components where the two computed curves are essentially the same. A slight discrepancy is observed for the v-component simply because of the low magnitude of the v-component compared to the total velocity. This computation reflects the fact that both the direct Biot-Savart computation using BCVEs and the fast vortex method yield essentially identical results.

Finally, complete calculations of isolated main rotor runs were carried out, using all of the wake acceleration techniques described in this section. A representative sample case was that of the a UH-60 main rotor at advance ratio 0.15 in which 5000 free vortex elements were used. All of the options cited in this section were enabled, i.e., the fast vortex method, limited application of wake updates, and backward difference time stepping. The aggregate acceleration of the computation was a factor of 11; in practical terms, this translated into a calculation requiring only 8 CPU hours on a Silicon Graphics Indigo workstation in place of a 90 hour computation using the direct methods of the original RotorCRAFT code. Still larger computations realize even more of an improvement, a case with 10,000 elements experienced a CPU reduction of a factor of 17. It is difficult to scale these computations in a concise manner, but it is clear that RotorCRAFT/AA can accelerate rotor calculations by over an order of magnitude relative to the original RotorCRAFT code even without the application of reconstruction.

4.0 MODELING OF VORTEX CORE STRUCTURE

A persistent challenge in any study of rotor loading with free wake methods is the characterization of the vortex core. In general, the wake-induced velocity field can be computed through direct application of the Biot-Savart law, but some numerical smoothing must be introduced to remove the singularities present for close interactions of vortex filaments with evaluation points on the blade and in the wake itself.

Clearly, it is desirable to employ a model that resembles as closely as possible the physical swirling velocity distribution within the vortex core. This aim is complicated by a limited understanding, even on an empirical basis, of the actual structure within the core; the experimental information gathered to date (Refs. 31-33) has been instructive, but does not cover the full range of possible combinations of wake age and blade loading that would be needed to parameterize the core structure for general flight conditions. Even with such information in hand, the challenge of "mapping" experimental core information onto the computational filament structure would itself be prohibitive.

Thus, computational modeling of the vortex core properties is necessary. Direct resolution of the process of wake roll-up is still well beyond the scope of engineering analysis methods for routine applications, given the difficulties associated with direct computational attack on even simple model problems (Ref. 34). The majority of methods implemented to date have applied simplified functional forms to smooth the induced velocity fields in the immediate vicinity of Lagrangian wake filaments. Proposed approaches have involved the use of cores involving solid body rotation (Ref. 36), a closely related smooth functional distribution (Refs. 35 and 37), and a Betz roll-up model (Ref. 12). All of these approaches have achieved some limited degrees of success, but all have also shown substantial sensitivity to the particular choice of core size. One of the ongoing objectives of work on the CVC wake model and its successors has been to reduce as much as possible the purely modeling role of core size as a "dial" in typical computations, as well as to introduce more direct physical motivation into the selection of the flow model for the core. Recent work in this area will be addressed after a discussion of the approaches previously taken in this direction.

4.1 Core Modeling in the Baseline CVC Wake Model

One of the objectives in formulating the CVC wake model was to remove as much of the sensitivity of airload results to core size as possible. As long as core radius parameters exist within wake calculations, it will be possible to "dial" or adjust the predicted loads. The discussion that follows outlines an approach that is judged to constitute a reasonable step towards reducing the modeling role of vortex filament cores.

It is first important to appreciate that the full-span CVC free wake model itself contributes substantially to the aim of weakening the modeling role of the core. Alternative models, such as using single free tip filaments, must of necessity use adjustments in the core size to capture flow field effects which are in fact attributable to spanwise and azimuthal loading changes. Since such changes are automatically captured with the CVC wake analysis, one possible ambiguity has been removed. Of course, the solution accuracy will still be dependent on the number of filament trailers, since this is a very basic measure of the numerical discretization of the problem. In most of the cases examined to date, only relatively small differences in airloads are observed once the maximum number of vortex filament trailers is increased above 14. However, since modeling wake-induced blade loading - and particularly BVI- properly is still a topic of research, it is difficult to reach definitive conclusions on this point. As with any

30

numerical method, it behooves the investigator to occasionally increase spatial resolution (i.e., the number of filaments) above the recommended threshold in order to gauge if results are affected.

However, since filamentary vortices are in fact still used, some effective core structure must be imposed to remove the flow field singularities associated with line vortices. The core model used in the baseline CVC model was the one originally proposed by Scully (Ref. 35); the swirl velocity profile is

$$v_\theta = \frac{\Gamma}{2\pi} \frac{r}{r^2 + r_c^2} \tag{4-1}$$

This constitutes an 'algebraic' core model, which retains half of the vorticity associated with the vortex inside the core radius r_c and leaves half outside. Scully notes that this swirl velocity profile has considerable experimental substantiation. Also, this particular core structure is a convenient choice for the implementation of vortex elements based on ANM, as discussed in Section 2.

The issue of the selection of the core radius itself remains. In the basic CVC wake model the core radii are determined by the analysis and not by the user, eliminating the possibility of "dialing" in results. The radii vary from filament to filament and along filaments from azimuth to azimuth. In keeping with the spirit of the discretization of the CVC wake, which places curved filaments on contour lines of constant strength of the wake sheet trailing from each blade, the local core radius is based on the distance between vortex release points at each azimuth. (Note: vortex release points are the points at which the vortex filaments release from the blade, as called for by the circulation distribution on the blade at a given azimuthal location). The core radius becomes the average distance to the neighboring release points on either side (at a given azimuth) with special cases at the root and tip of the blade. That is, for filaments numbered n-1, n, and n+1, the core size of filament n is computed as

$$(r_c)_n = \frac{((r_v)_n - (r_v)_{n-1}) + ((r_v)_{n+1} - (r_v)_n)}{2} \tag{4-2}$$

At the center of the blade circulation distribution, averages are taken between the nearest filament and the maximum circulation line. At the root and the tip, averages are taken using the distance to the blade cutout or the blade tip.

In the current analysis, bounds can be placed on the core size and, if desired, particular core radii can be chosen for each filament. Numerical experimentation has shown that the rotor loading is still sensitive to arbitrary adjustments in core size. However, the mode of operation for the correlation runs discussed in References 3 and 4 (as well as those below) was to allow the core radius assigned to each filament to adjust itself to local conditions as dictated by Eq. 4-2. It is judged that this approach is consistent with the overall aim of removing as much arbitrariness as possible from the analysis of rotor airloads.

One weakness in this treatment, however, is that it does not provide for directly treating rolled-up vortices that are, in fact, well represented by a single filament or that are partially rolled-up yet contain significant vortical structures. Currently, these are modeled as clusters of overlapping filaments with algebraic cores. Such an approach is technically consistent with the structure of the CVC wake model, in that circulation

trailed from the tip region will be conserved, the filament trajectories will trace the position of the centroid of vorticity, and the gross scale of the distribution of vorticity in the wake will be captured. Also, in the limit of a large number of filaments and for a wake trailed from a blade with a steep gradient of circulation near the tip, the CVC wake will form a tightly clustered vortex. However, this approach still leaves out significant features of the inner core structure of the wake where viscosity plays an important role.

Until recently, it has been impractical to consider implementing a model that attempts to capture this behavior except in a very coarse manner. Two circumstances have combined to change this:

- first, the implementation of flow field reconstruction; as noted above, this provides a ready framework for the implementation of sophisticated inner solutions for the vortex core, through the application of ANM

- second, the development of efficient rollup models based on integrated blade properties; this is an extension of early work in Reference 38 on the prediction of wake self-induction, which in turn was related to integral models of wake rollup and core structure in the spirit of Betz (Refs. 39 and 40).

The following section describes the particular rollup model developed for use in the context of rotor wake calculations, while Section 4.3 outlines its implementation in RotorCRAFT/AA.

4.2 Vortex Core Modeling Based on Integrated Blade Properties

As noted above, each rotor blade trails a vortex sheet along its span that is modeled numerically using the CVC wake constructed of curved vortex filaments. In many situations, a peak in bound circulation occurs near the blade tip. The portion of the vortex sheet between the maximum circulation point and the blade tip rolls up into a concentrated vortex structure. The structure of this vortex is treated analytically by a separate procedure, since the basic numerical scheme cannot resolve this region accurately. This analytical approach is also more computationally efficient.

The roll-up of the sheet occurs rapidly and proceeds from the tip region inward. The sheet rolls up into a large, tightly wrapped spiral. The radius of the spiral scales with the spanwise extent of the original sheet, the exact relationship depending on the details of the circulation distribution. In an ideal inviscid flow, at the center of the spiral the velocity would be infinite and the spiral turns infinitesimally close together. Under these circumstances the actual flow is unstable, and a viscous/turbulent core forms in a relatively small region at the center of the spiral vortex. The actual size and structure of this central core depends on the circulation distribution.

The structure of the vortex core must be known to predict the self-inducted motion of curved vortex filaments, and to accurately predict blade vortex interaction. A weakness of prior free-wake analyses has been the arbitrary specification of vortex core size and structure. The present analysis is a significant step towards establishing a sound technical means to characterize the vortex core.

4.2.1 Analysis Method

The vortex core is divided into two parts: an outer spiral region characterized by vortex sheet roll-up, and a viscous/turbulent central core. The structure of the spiral region is governed by the following conditions:

- mass flow conservation
- Bernoulli's equation
- conservation of circulation and vorticity centroid
- conservation of axial flux of angular momentum

Figure 4-1 shows the configuration for spiral roll-up. Each of the above conservation conditions is applied on a station-by-station basis, namely on each of the progression of annular streamtubes beginning at the blade and ending in the formed vortex. At the blade each streamtube is centered on the local centroid of vorticity. The spiral structure is assumed to be sufficiently fine and tightly wound that the final vortex flow is axisymmetric to good approximation. Bernoulli's equation applies because all points in the spiral are in the same domain of irrotational fluid, and can be reached without crossing vortex lines due to the spiral structure. The axial flux of angular momentum is related to the torque applied to the streamtube by the lift on the blade tip region. Application of these conservation conditions leads to a pair of coupled nonlinear ordinary differential equations, as described in Reference 38.

The present model extends the earlier model by using a the turbulent vortex core that is modeled in integral fashion. Functional forms of the swirl and axial velocity distributions are assumed which are consistent with experimental data. The swirl velocity is assumed to be a central region of solid body rotation surrounded by a log-law velocity distribution. The axial velocity is assumed to satisfy a simple power law as a function of radius. This turbulent core is related back to a corresponding streamtube passing over the tip of the rotor blade, as shown in Figure 4-2. The following conservation conditions are applied in integral form:

- net mass flow conservation
- conservation of circulation and vorticity centroid
- conservation of net axial flux of angular momentum
- conservation of net axial momentum

Note that the axial momentum balance replaces the Bernoulli equation, which no longer applies. This momentum balance includes force and fluxes on the vortex streamtube at the wing, in the formed vortex, and on the streamtube sides. Given the assumed functional form of the velocities, the conservation conditions lead to a set of coupled nonlinear algebraic equations.

The solution procedure consists of satisfying the integral conservation conditions for the turbulent vortex core and solving the differential equations for the vortex sheet roll-up. The core radius provides the inner boundary condition for the sheet roll-up equations, and the outer boundary condition is that the axial velocity return to free-stream value. Only one core radius satisfies both these boundary conditions and the integral conservation conditions. The solution procedure is difficult because it involves finding the solution to simultaneous nonlinear equations.

4.2.2 Results of the Rollup Calculation

One case can be solved analytically in closed form. When the bound circulation distribution decreases to zero linearly at the tip, the spiral roll-up equations and boundary conditions can be solved in a fairly simple manner. The problem is then reduced to finding the solution of a system of nonlinear algebraic equations. The radius of the turbulent core, and the radius of the surrounding spiral, are found in terms of a
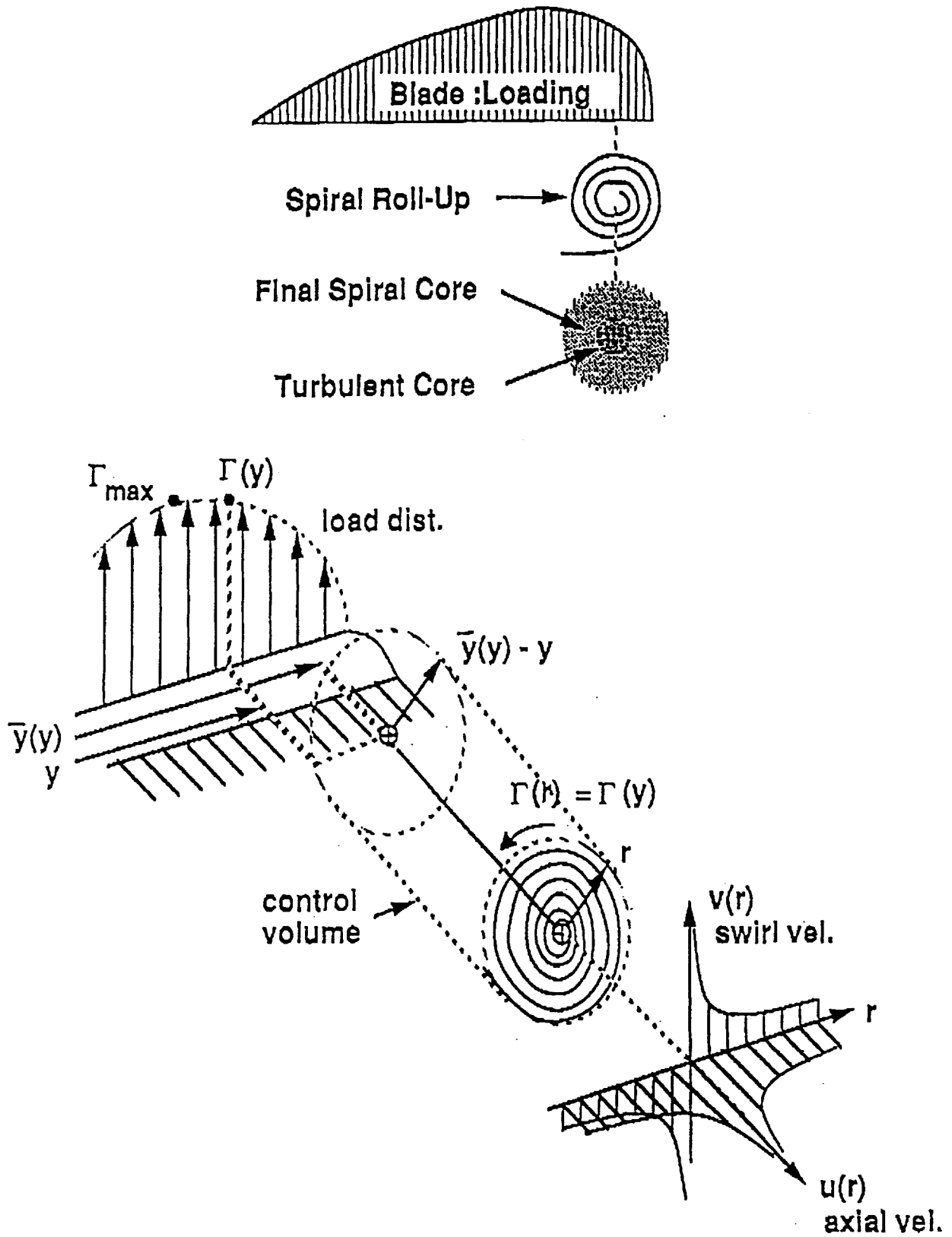
33

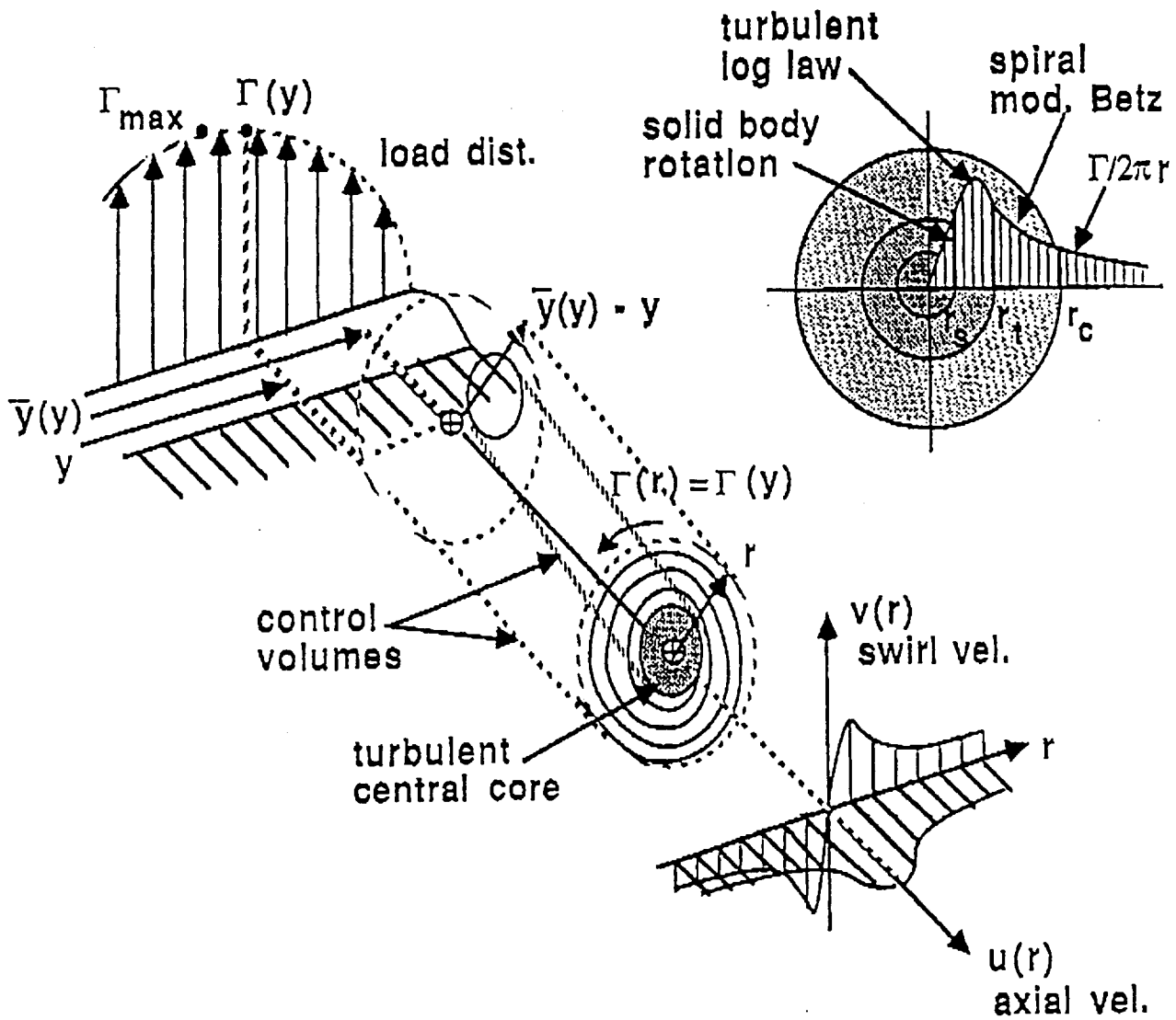Figure 4-1. Schematic of inviscid tip vortex rollup model.

Figure 4-2. Schematic of tip vortex rollup model including viscous core effects.

35

nondimensional loading parameter $\varepsilon = \Gamma/(2\pi s U)$, where Γ is the maximum circulation, U is the average freestream onset velocity in the blade tip region, and s is the span of the tip region (from maximum Γ to the tip). Note that larger ε corresponds to higher tip loading, namely higher lift coefficient in the tip region.

Figure 4-3 shows the dimensionless turbulent core radius r_t/s and the dimensionless spiral core radius r_c/s as functions of ε for the case of linear loading. Note that this nondimensional result is universal in that it applies for all cases having linear tip loading. The physical behavior indicated by this curve is interesting. As the loading parameter, ε, increases, the outer radius of the spiral contracts and the radius of the turbulent core grows. The contraction of the outer radius is associated with increased axial velocity associated with increased loading. This axial velocity draws the spiral structure inward to conserve mass flow as the vortex rolls up. At the same time, greater axial velocity leads to a larger, more energetic turbulent core structure. The swirl and axial velocity distributions for two values of ε are shown in Figure 4-4. The distributions shown here for wing calculations are similar qualitatively to those observed in rotary wing computations in RotorCRAFT/AA; as suggested schematically in Figure 4-2, the peak swirl velocity typically occurs in the turbulent core region, outside of the boundary of the region of solid body rotation.

Other tip load distributions can be solved numerically. Of particular interest is elliptical loading. In these cases the system of nonlinear algebraic equations governing the turbulent core must be solved simultaneously with a shooting problem involving the nonlinear differential equations for the spiral region and their boundary conditions. In each such case, the results are reducible to a single nondimensional curve for the radii r_t/s and r_c/s as functions of ε, similar to Figure 4-3 for linear loading. An elliptic rollup calculation is not presently implemented in RotorCRAFT/AA; this option will be incorporated future versions of the analysis.

However, the solution for the rollup of the linearly loaded blade tip described above can be used to approximate the behavior of the elliptic case. This is done by constructing a loading distribution consisting of a constant lift section followed by a linear roll-off to the blade tip. In this approximation, the size of these regions are chosen such that the same total lift is obtained as in the elliptically loaded tip; this corresponds to a constant-lift section 0.57s followed by a linear roll-off over the remaining 0.43s. Applying the rollup calculation to this roughly equivalent distribution allows the determination of a core size and swirl velocity that approximate those that would be obtained from a direct calculation of elliptic roll-off. This is the approach presently in place and the results shown in Section 7 incorporate this assumption.

To summarize, this portion of the rollup analysis functions as follows: for a given value of bound circulation Γ at a spanwise station a distance $s = k_R R$ inboard of the tip over which the average onset free stream speed is U, a value of ε is computed. This is used to compute core velocity distributions using the procedures and assumptions just described. The remaining issue is how to associate a portion of the wake at a given azimuthal age downstream with a particular region on the blade so as to allow this computation to be carried out. The following section describes this procedure in more detail.
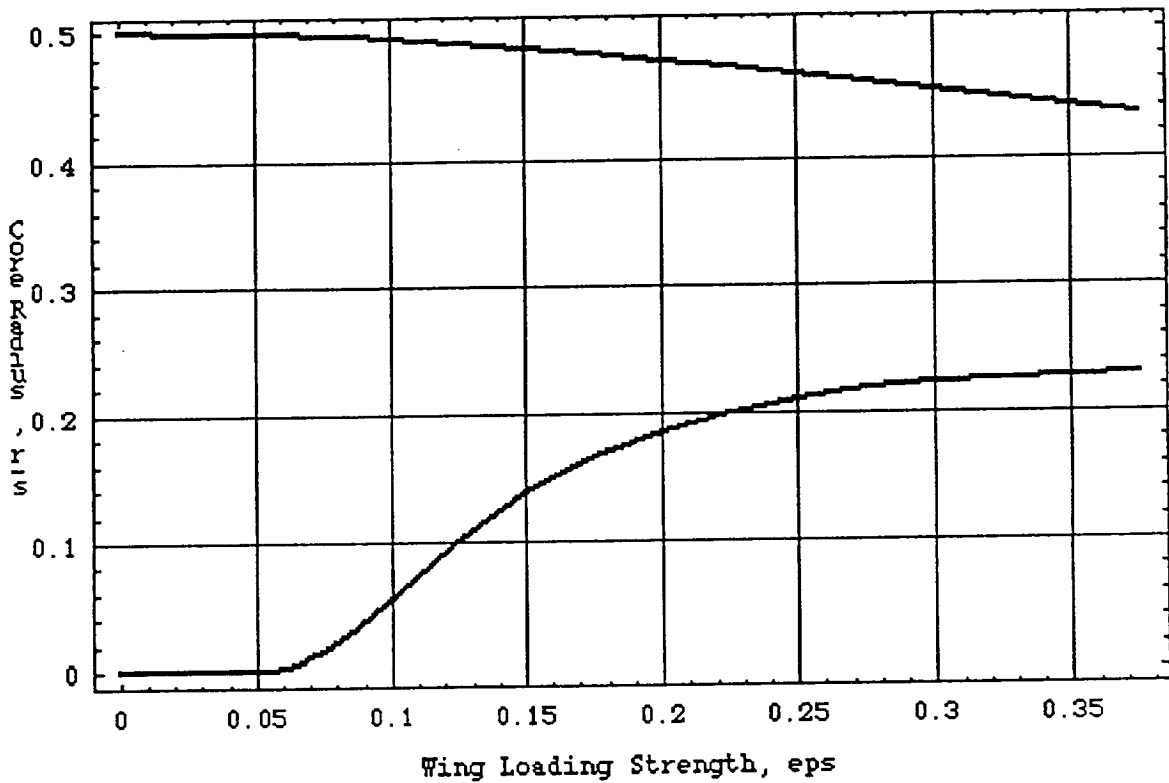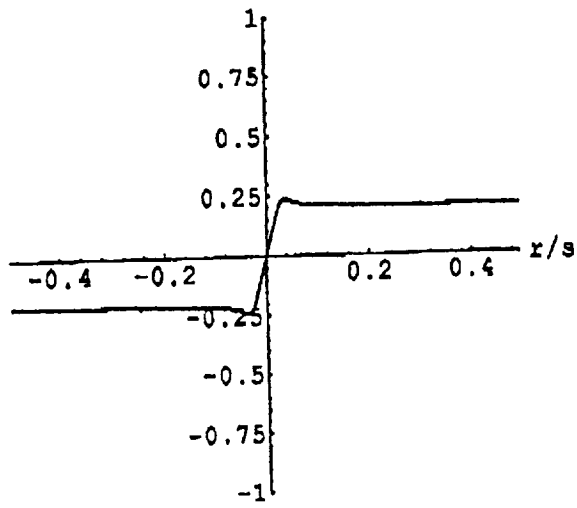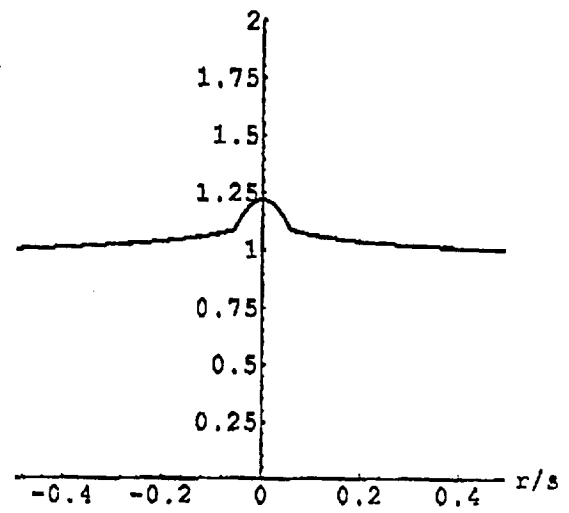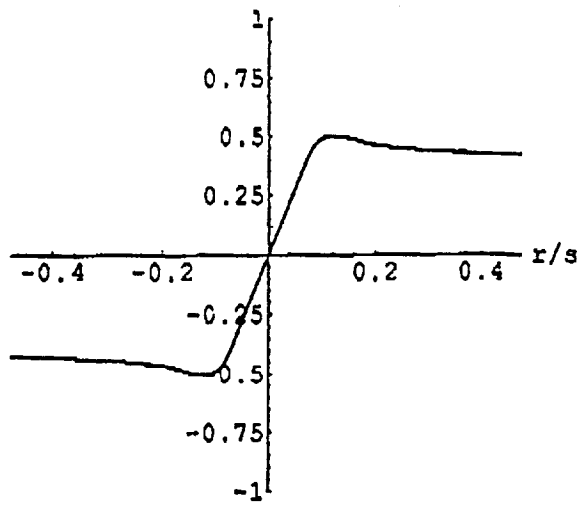
36

Figure 4-3. Analytical solution for the inviscid and turbulent core radii for the linear rollup model: upper curve = inviscid core ; lower curve = turbulent core . Core radii normalized by s , the spanwise extent of the rollup region adjacent to the blade tip.
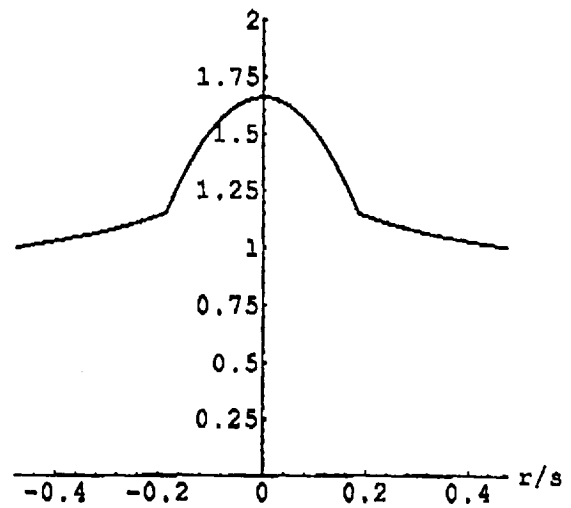
a) v/U , ε = 0.1

b) u/U , ε = 0.1

c) v/U , ε = 0.2

d) u/U , ε = 0.2

Figure 4-4. Detailed swirl and axial velocity distributions as a function of radial distance
from the vortex core (normalized by s) for two values of blade tip loading.

4.3 Implementation in RotorCRAFT/AA

With the model for vortex core properties in hand, it remains to implement it in a manner consistent with the CVC wake model and the reconstruction approach. As noted previously, as part of the reconstruction process the vortex scanning routines capture the filament trajectories in the vicinity of the rotor blades. In the basic approach discussed in Section 2, the inner solution that recovers the "actual core" properties is applied on a filament-by-filament basis, with each constant-strength filament being corrected locally to recover the velocity field induced by the filament with the "actual core". However, to consistently to incorporate the model of the rolled-up vortex just described, several filaments must be "bundled" together and considered effectively merged. It is important to note at the outset that this bundling will not necessarily involve all of the filaments trailed outboard of the peak in bound circulation but may instead reflect a partially rolled-up vortex wake.

Several closely related issues must be addressed to effect this bundling:

- First, for a portion of a vortex filament of a given azimuthal age, the spanwise location of its release from the generating blade must be identified; a criterion must be established to determine whether this filament is to be treated as part of a bundled filament; if so, the spanwise extent of these regions (i.e., the fraction of the bound circulation that is to be rolled up) must be identified and the distribution of circulation within this region stored.

- Second, those filaments trailed from this region must be "tagged" and identified as filaments to be bundled together; those that pass into the scan volume around neighboring blades must be identified for the reconstruction program to be treated as a single rolled-up filament.

- Third, the new core model developed in the previous section must be applied to allow the swirl velocity for this new inner core solution to be computed.

The first of these tasks, effectively establishing a rollup criterion, involves estimating the time required for the wake trailed by a given distribution of circulation to roll up. A useful conceptual framework for this is provided by an existing fixed wing wake rollup analysis (Ref. 41); this reference describes a modified Betz roll-up model, with the downstream state of the vortex (i.e., percentage of strength rolled up) given by a closed form calculation as a function of the initial loading distribution and the downstream distance. In the cases examined here, the outboard portion of the blade is treated as an effective wing, and the distance downstream of this "wing" required for completion of the rollup is converted into an azimuthal increment downstream of the rotor blade, as described below. (Note: though the fixed-wing analysis in Ref. 41 is not strictly applicable to rotary wing tip vortex roll-up (because of the absence of the symmetry of the trailing wake about the peak circulation as well as because of the neglect of the effects of rotation and wake curvature) it was nonetheless judged to provide a useful guide for estimating the degree of roll-up that occurs in typical rotary wing calculations. A model more closely fitted to the rotary wing environment would be a desirable improvement to the current treatment).

Denoting the nondimensional distance from a given radial station to the blade tip as $k_R R$ and nondimensionalizing the circulation Γ at this station by ΩR^2 yields a form for the "vortex age parameter" D as follows:

39

$$D = \frac{1}{2} \frac{\bar{\Gamma}}{k_R{}^2} \varphi \qquad (4\text{-}3)$$

Here, ϕ is the azimuth angle downstream from the generating blade. Note that this parameter incorporates both a measure of the circulation gradient on the generating blade and the azimuthal age of vortex wake, making it a physically plausible descriptor of the rollup process. The motivation for including this parameter is to add some measure of physical motivation to the amalgamation of the trailers, rather than adopting a simpler, more ad hoc approach involving, for example, merging all tip filaments at a given azimuthal age downstream of the blade.

Assuming an equivalence between the rollup of the wake of the blade tip and the wake of a wing, a value of D of 1.0 corresponds to a rollup 90% of the strength of the vortex sheet from an elliptically loaded tip, while a value of D of 0.2 corresponds to roughly a 60% rollup (Ref. 41). For further illustration, consider a limiting case where all of the bound circulation outboard of the peak level on the blade is to be rolled up. For D = 1 and typical values of $\bar{\Gamma}_{max}$ of .01 and k_R of 0.1, ϕ is 2.0 radians, indicating that rollup will take place within roughly 120 deg. downstream of the generating blade. Note, however, that larger values of k_R (corresponding to shallower blade loading gradients near the tip) rapidly increase the value of ϕ; using $k_R = 0.25$ (a quite realistic value for blades in the second quadrant), ϕ increases to 12.5 radians or essentially two full rotor revolutions. This indicates that shallow loading gradients on the rotor blades are associated with protracted rollup processes that may lead to following blades encountering partially rolled up wakes.

In the present implementation, a value of D is selected at the outset of the computation when the integral core model is to be invoked. Given this, all filamentary trailers are checked at each value of ϕ to see if, for the specified value of D, the blade loading on the generating blade (which determines k_R and $\bar{\Gamma}$) was such that the filament should, at an age of ϕ, be considered part of a rolled-up bundle. The actual procedure involves scanning the bound circulation distribution on the generating blade and identifying all filaments that are released outboard of locations where the following test is true:

$$\frac{1}{2} \frac{\bar{\Gamma}}{k_R{}^2} > \frac{D}{\varphi} \qquad (4\text{-}4)$$

Once the outboard portions yielding rapidly rolled-up wakes are identified in this manner, the filaments that trail from them are tagged. These filaments will now act as "markers" that define the position of a "replacement vortex" formed from a bundle of individual filaments; this bundled "replacement vortex" is assumed to lie at the centroid of the bundle of marker filaments. Using the individual filament geometries that pass through scan volumes like those shown in Section 2 (Fig. 2-6), the trajectory of this replacement vortex is computed for use in the reconstruction analysis. The CPU time required for this process is essentially negligible compared to the computation of the motion of the free vortex wake itself.

To complete the implementation, the four-part integral core structure model is applied to this replacement filament, using the strength of the bundled filaments to determine the level of the swirl velocity. This swirl distribution becomes the new inner solution for the ANM treatment of wake-induced velocity.

At present, the choice of the vortex age parameter D produces several distinct effects. Selecting a high value will in general lead to very few or no filaments being treated with the rolled up integral model, since only very "old" filaments will be bundled and these may be downstream of the rotor disk itself (note that in cases where bundling is not invoked, the Scully core acts on each filament). As D is decreased, however, a progressively greater range of younger filaments (i.e., filaments more likely to be close to the rotor disk) are bundled, which will in general lead to a larger number of discrete blade/wake interactions; also, as D is decreased, the strength of the bundled replacement vortices will in general increase as more filaments are lumped into them. A complication can be introduced, however, since the location of replacement vortex is assumed to be at the centroid of the bundled filaments at a given azimuthal age. Thus, as D is altered the replacement vortex may move as the number of filaments bundled together changes, possible altering the relative location of the blade and the filament.

As will be seen below, the present rollup model does allow physically significant mechanisms of blade loading to be captured, though the current treatment, being a relatively simple model of a complex phenomenon, does also introduce some undesirable extraneous loading events. Also, the use of a fixed wing rollup model in a rotary wing context is clearly an approximation, though one that has proved useful in work to date. Thus the analysis underlying this part of RotorCRAFT/AA is a topic of ongoing work; the primary topics being addressed are the extension of the range of core models to accommodate more general tip loadings, alternatives to the current assumption that places the replacement vortex at the centroid of the vortex bundle, and studies of the influence of particular choices for the age parameter D.

5.0 DUAL ROTOR MODELING

The present RotorCRAFT/AA code features substantial capabilities in the analysis of dual rotor systems, of which one particularly common example is the main rotor/tail rotor (MR/TR) combination. One focus of earlier work on flow field reconstruction (Ref. 1) was the analysis of the interaction of the vortex wake of the main rotor on the tail rotor. Owing to the relatively simple geometry of most interactions with the tail rotor, this was a suitable early demonstration of the capabilities of this general approach. Though the primary focus of the present effort has been on main rotor loading, the major capabilities for tail rotor load reconstruction have been retained from earlier coding and in many cases extended. This section describes these capabilities and outlines some of the computational results obtained to date.

5.1 Typical Main Rotor/Tail Rotor Interactions

One of the first tasks undertaken in this area was the execution of sample calculations to investigate the type of MR/TR interactions characteristic of particular flight regimes. Initial results on this topic appear in Reference 42, including a discussion of the impact of climb angle, tail rotor inflow, and forward flight velocity. For that preliminary effort, it was judged appropriate to scrutinize a few representative cases, in particular sample calculations of a "generic" two-bladed rotor at a thrust coefficient of .004 in level flight. The results in Reference 42 include a case at advance ratio 0.3, with a tail rotor located 1.3R downstream of the main rotor (hub to hub distance) with a radius of 0.2. The top and side views of the main rotor wake shown in Figure 5-1 indicate the vortices being swept through the tail rotor disk The dense cluster of positive filaments that form the tip vortex are evident in Figure 5-1a; succeeding plots show these positive vortices being convected through the tail rotor disk, along with the more highly distorted inboard filaments.

This particular case is representative of the results of other similar computations, which have indicated that the primary type of interaction characteristic of single-rotor helicopters is the near-normal intersection of relatively "young" tip vortices trailed from the main rotor blades just upstream of the tail rotor disk. In addition, wake geometry plots such as Figure 5-1 make it clear that the inboard wake can impinge on the tail rotor in many flight conditions, particularly at high forward speed. Plots of the velocity field in and around the tail rotor disk (shown in Refs. 1 and 42) also indicate that this portion of the wake can make significant contributions to the local flow field, particularly the component normal to the disk.

As a result of these initial calculations, it was concluded that the convection dominance of the high speed cases will cause discrete filaments from the CVC wake to transit the disk in a narrow "corridor", though the intensity of the vortex interactions will depend not only on the intersection trajectories but on the relative phasing of the main rotor and the tail rotor as well. At lower speed, the high downwash along the wake centerline sweeps most discrete filaments away from the disk, leaving only a relative few trailed immediately upstream to undergo interactions. For low as well as high speed, the tip vortices intersect the disk at angles very near ninety degrees (deviations from this in typical calculations are no higher than 15 degrees, and changed only minimally during the transit).

Additional computations carried out as part of the present effort reinforced these conclusions. The calculations are based on the flight test experiment of the Aerospatiale Puma helicopter documented in References 43 and 44. This work involved the
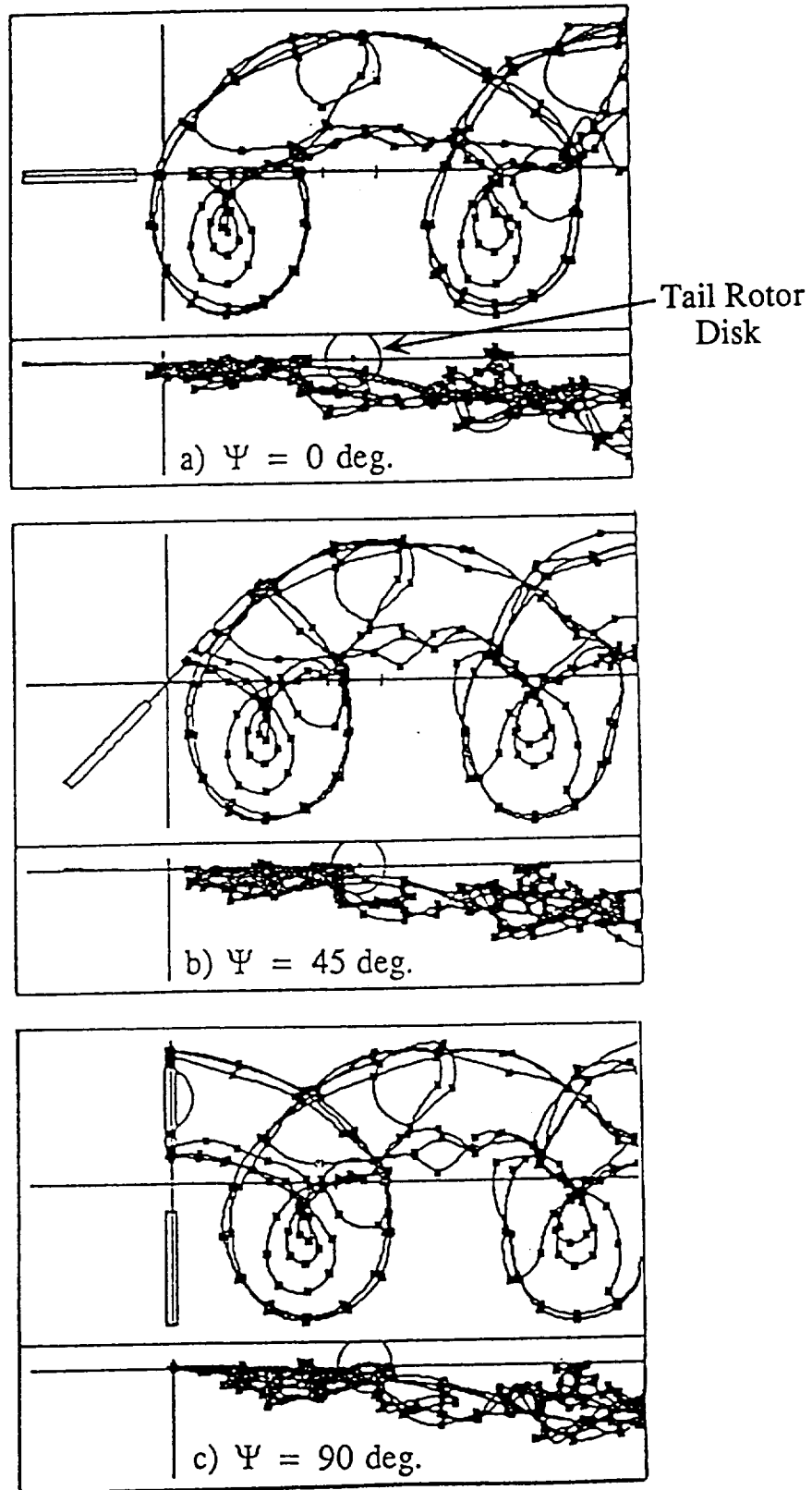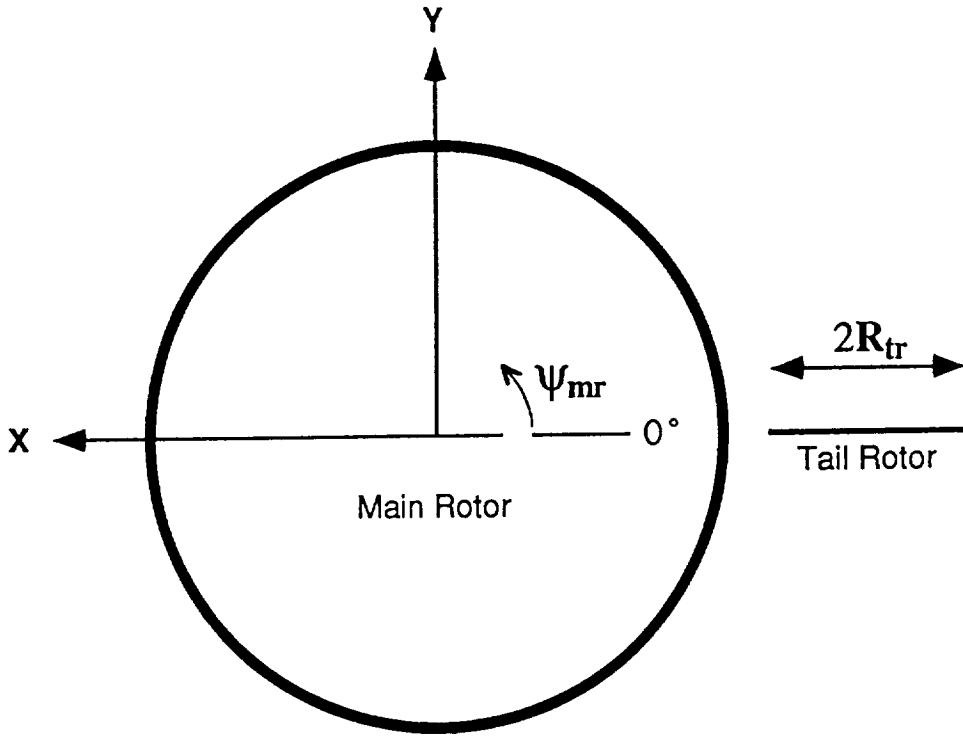
Tail Rotor
Disk

a) Ψ = 0 deg.

b) Ψ = 45 deg.

c) Ψ = 90 deg.

Figure 5-1. Top and side views of MR wake geometry and tail rotor position for a typical two-bladed rotor, advance ratio = 0.3 .

43

acquisition of a unique body of data on the unsteady surface pressure on tail rotor blades in the presence of the main rotor wake. The data was taken on one blade of the tail rotor of a Puma in hover and in forward flight at 10, 20, and 30 knots. The tests measured the instantaneous pressure coefficient at 2% chord; this local value of C_p has been found to be a suitable indicator of the sectional lift coefficient. With the assistance of RAE personnel, data containing the unsteady pressure measurements for the 30 knot case was obtained for use in correlation studies with the RotorCRAFT/AA code.

The sign conventions and the co-ordinate system adopted here are defined as shown in Figure 5-2. The gear ratio of the tail rotor to the main rotor is 4.82, and therefore the azimuth angle of the tail rotor is not necessarily in phase with that of the main rotor. To date, only the case in forward flight with a free stream velocity of 30 knots (advance ratio 0.072) has been considered. In the calculations that follow, the azimuth of the instrumented tail rotor blade is initialized to be $\Psi_{tr}=67.22°$ when the reference blade of the main rotor is at 0° azimuth. In this case there will be three complete revolutions of the instrumented tail rotor blade in the revolution of the main rotor. The first complete revolution of the instrumented tail rotor blade starts when the main rotor reference blade is at $\Psi_{mr}=60.74°$; the second begins when the reference blade is at $\Psi_{mr}=135.43°$ and the third begins when it is at $\Psi_{mr}=210.12°$.

The first calculation is arranged such that the tail rotor blade can only "see" the wake of one blade of the four-bladed main rotor. The intersections between the blade tip filament and the tail rotor disk for the three complete revolutions of the instrumented blade are shown in Figure 5-3a. The symbols showing filament intersections with the scan plane are each one main rotor time step apart, and different symbols are used for each tail rotor revolution. Forty time steps are used in each main rotor revolution, yielding between eight and nine time steps per tail rotor revolution. The azimuthal scanning polar plot of the z-component velocity evaluated at one tail rotor blade are given in Figure 5-3b. (It is important to note that this does not represent an instantaneous "snapshot" of pressure over the disk but rather a continuous sweep of a single blade over the disk, representing a complete tail rotor period. Because the tail rotor rotation frequency is not an integral multiple of the main rotor frequency, these plots repeat themselves only over very large numbers of tail rotor periods; thus, time domain simulations must be carefully phased with the position of the generating blade on the main rotor). It is observed from Figure 5-3a that for the second revolution, the filaments (square symbols in Fig. 5-3a) have been convected further downstream and are found intersecting the tail rotor disk; this event is captured by a high velocity gradient shown in Figure 5-3b. As the wake is convected further downstream and gets closer to the hub in the third revolution (diamond symbols in Fig. 5-3a), the region of high velocity gradient will shift correspondingly.

In a second set of calculations, the induced velocities at the moving plane include the contributions from the wake of all of the main rotor blades. In Figure 5-4a, the location of the tip filaments from all four main rotor blades during the third revolution of the tail rotor blade are shown on the plane of the tail rotor disk. The azimuthal scanning polar plots of the z-component of the flow field evaluated at the tail rotor blade surface are presented in Figures 5-4. It is shown that the reference blade first encounters the wake of main rotor blade #4 in the first quadrant of the cycle and then encounters the wake of blade #2 in the third quadrant. This causes two regions of high velocity gradients in Figures 5-4, one in the first quadrant and the other in the third quadrant. These plots clearly associate the transit of vortices across the disk with rapid pressure disturbances, and confirm the earlier observations regarding wake vortex geometry.

[Top View]

R_{mr} : radius of main rotor disk
R_{tr} : radius of tail rotor disk
α_s : main rotor shaft angle
ψ_{mr} : azimuth of the reference main rotor blade
ψ_{tr} : azimuth of the instrumented tail rotor blade
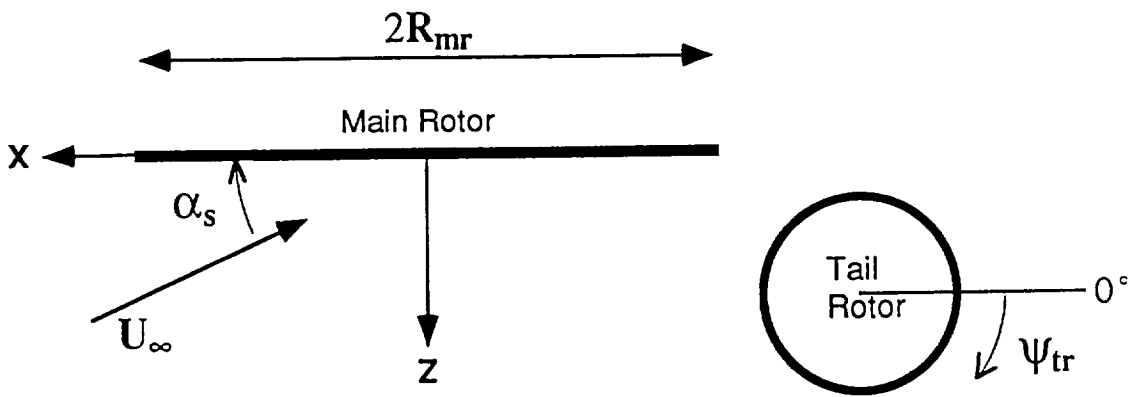
[Side View]

Figure 5-2. Co-ordinates and sign conventions of a typical main rotor and tail rotor system.
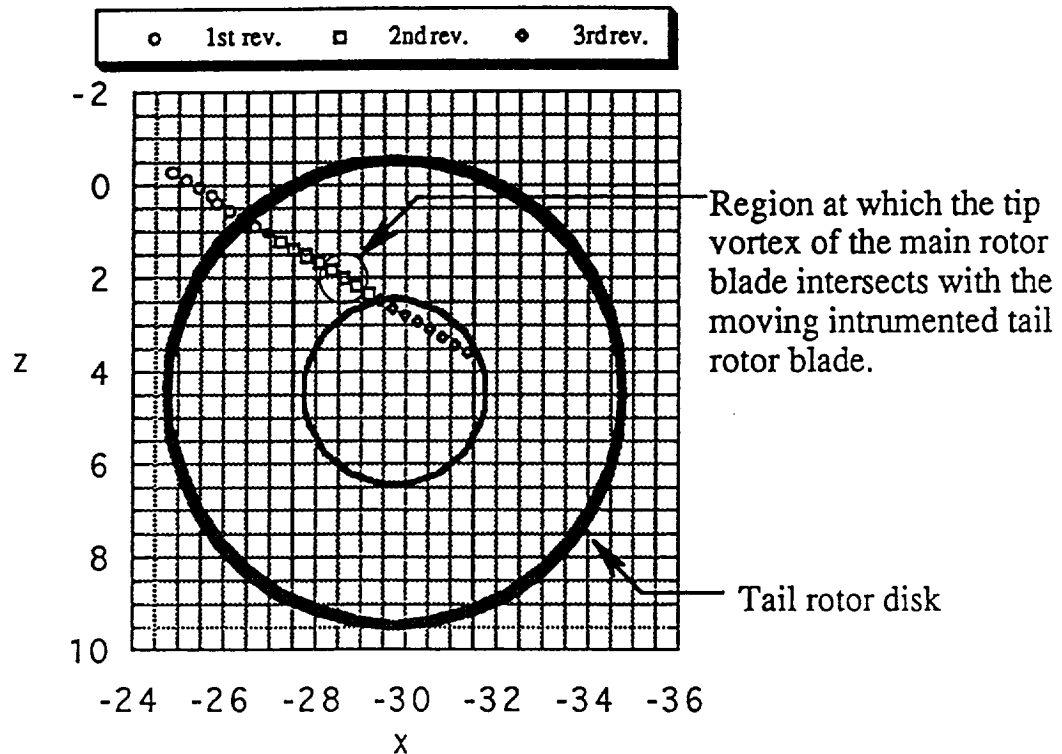
Figure 5-3a. Intersections of the tip vortex of the main rotor reference blade with the Puma tail rotor disk for three complete revolutions of the instrumented tail rotor blade.
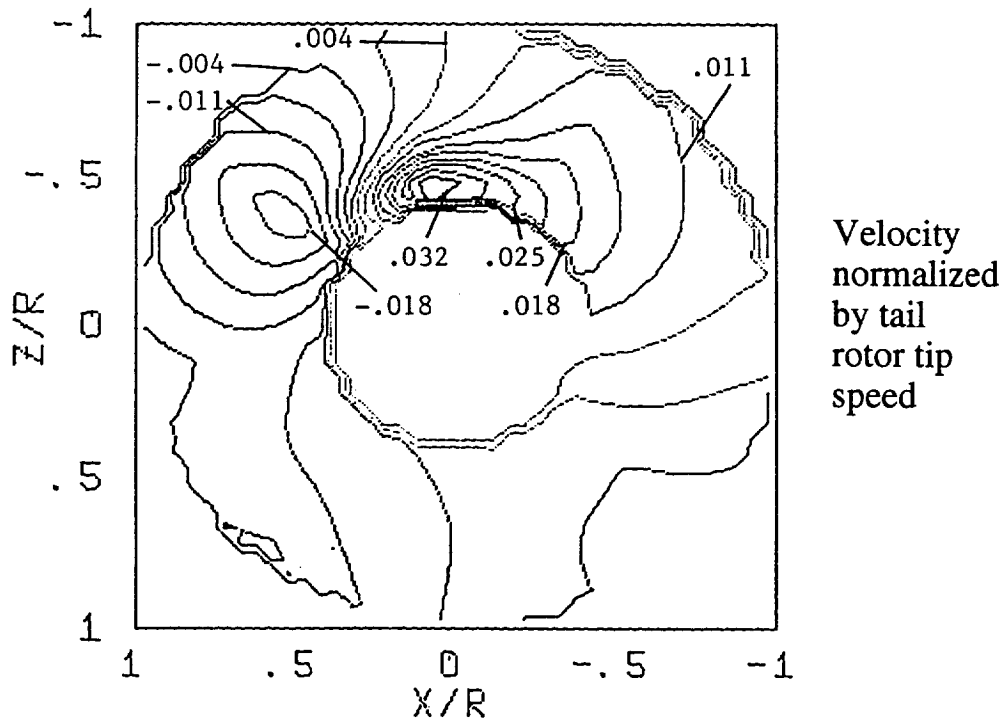
Figure 5-3b. Azimuthal scanning polar plot of the z-component velocity calculated at the instrumented tail rotor blade in its second complete revolution. (Only the wake of the main rotor reference blade is included in the calculation.)

46
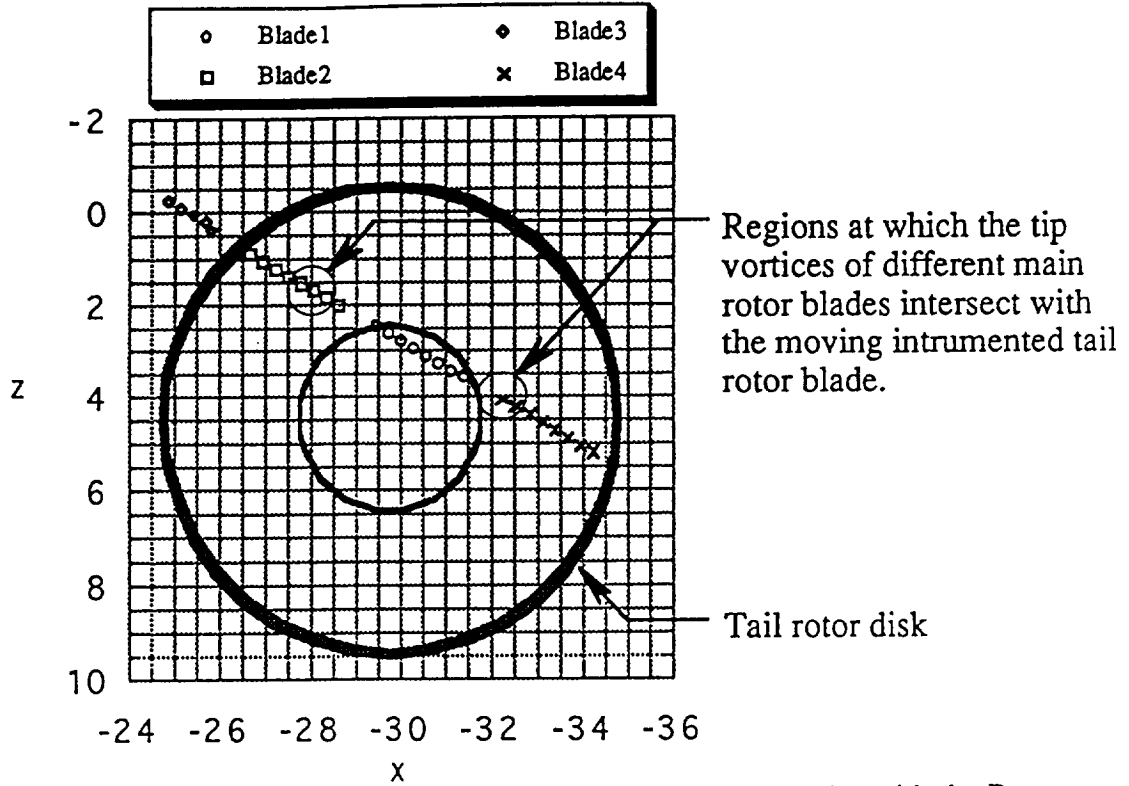
Figure 5-4a. Intersections of the tip vortex of all four main rotor blades with the Puma tail rotor disk at the third revolution of the instrumented tail rotor blade.
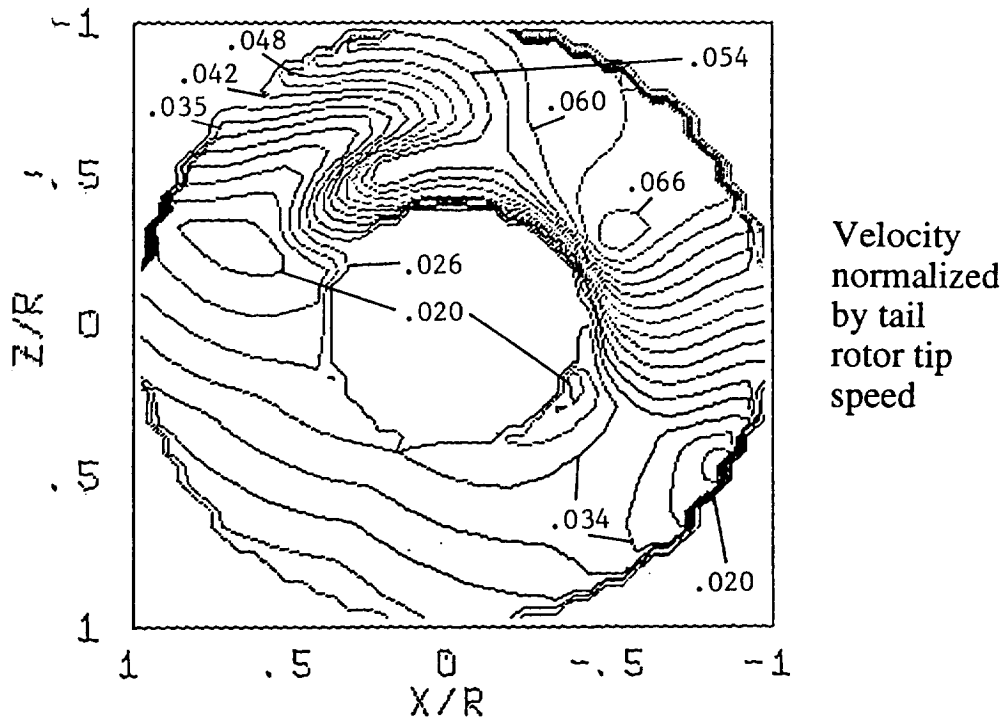
Figure 5-4b. Azimuthal scanning polar plot of the z-component velocity calculated at the instrumented tail rotor blade in its third complete revolution. (The wake of all four main rotor blades is included in the calculation.)

47

5.2 Tail Rotor Flow Field Reconstruction

The results just discussed and those generated in previous research motivated the approach to tail rotor flow field and airload reconstruction presently in place. It follows the outline of the general reconstruction techniques discussed in Section 2, though it is somewhat simpler in that the scan volume typically is fixed in space, and encompasses the entire tail rotor, as sketched in Figure 5-5. This figure schematically depicts both major classes of interactions experienced by the tail rotor, namely the transit of tip vortices across the disk and the close passage of inboard filaments. Using a scan volume type of method is necessary to capture the full range of such wake interactions.

As with main rotor calculations, vortex trajectory information is used to reconstruct the incident flow field at the tail rotor disk with a higher level of temporal resolution than that available from a direct calculation. The aerodynamic loading on the tail rotor blade can then be carried out in the presence of this flow field, assuming that it is "frozen", i.e. that the subsequent evolution of the tail rotor's own wake does not affect the main rotor wake trajectories. As will be discussed below, the present analysis allows quite general computations of MR/TR interaction within these restrictions, though during the course of this effort the "self-interaction" of the tail rotor with its own wake was investigated.

5.3 Modeling of Tail Rotor Aerodynamics

5.3.1 Tail Rotor Wake Effects

Initial investigation of tail rotor wake effects in Phase I involved a simplified model, consisting of a set of skewed vortex rings, as discussed in Reference 42. The thrust on the rotor was set at a value that would counteract the torque of the rotor, and the wake skew angle was set based on the free stream convection and an estimate of the self-induced velocity of the tail rotor wake. Even for this simple model, the wake of the tail rotor itself made significant contributions to the inflow at the disk. In view of the disparity of time scales for the main rotor and tail rotor, an approach was sought that would incorporate an accurate treatment of local effects on the tail rotor without the complication and computational cost of running two complete, fully coupled free wake calculations. To support an assessment of this issue, "stand alone" free wake tail rotor computations were executed.

To help assess the importance of rotor wake effects, it was useful to employ a representative pressure plot from the RAE Puma flight test data discussed above. Figure 5-6a shows a representative plot of the pressure data discussed in Reference 19; this figure is an azimuthal scanning polar plot which represents a complete time history of the pressure coefficient at 2% chord for a full rotor rotation. Also, the time increments in the measurements correspond to roughly 100 steps per tail rotor revolution, indicating that a high temporal interpolation factor must be used to obtain appropriate resolution. This calculation also provided a framework for exploring the application of reconstruction to the prediction of surface pressures on the instrumented tail rotor in the presence of the main rotor wake.

Flight test data and geometric layout information supplied by the RAE allowed the trim condition of the aircraft to be estimated. The computational model of the main rotor wake used four turns of free CVC wake; a baseline calculation was carried out involving forty time steps per main rotor revolution, corresponding to roughly eight time steps per tail rotor revolution, given the 4.82:1 gear ratio. To obtain reasonable reconstruction of the tail rotor loading, at least 40 time steps per tail rotor revolution are
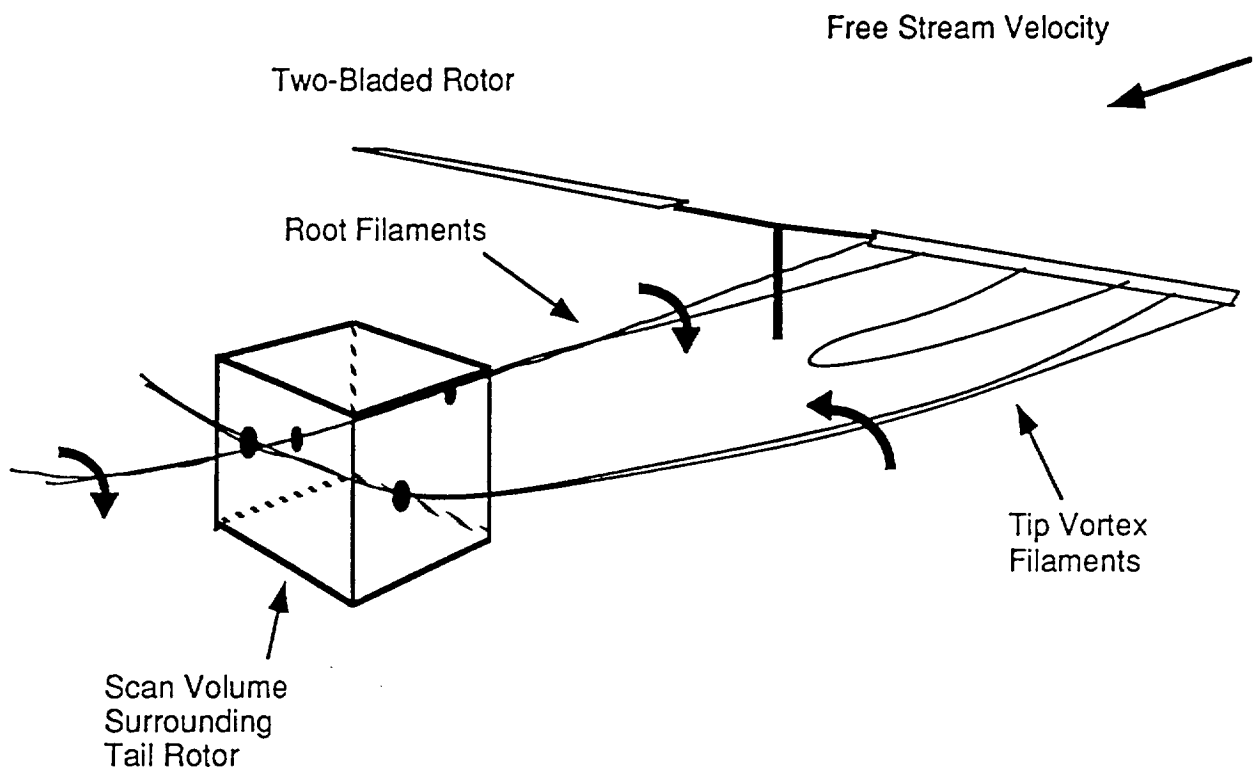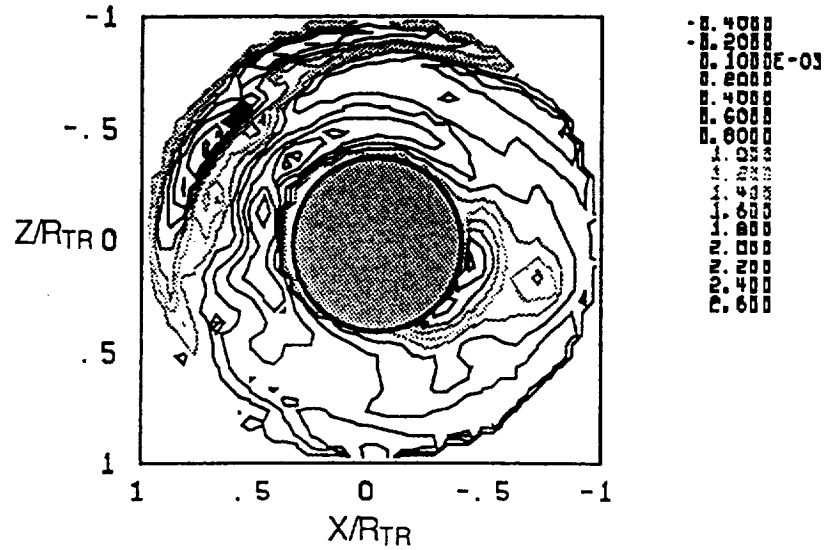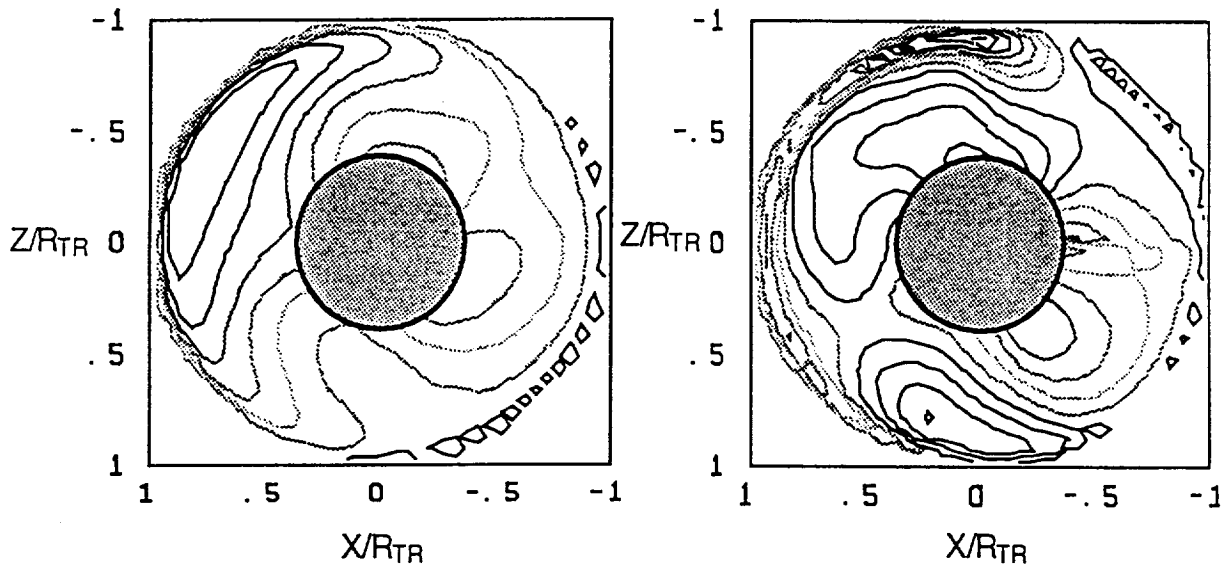
Free Stream Velocity

Two-Bladed Rotor

Root Filaments

Tip Vortex
Filaments

Scan Volume
Surrounding
Tail Rotor

Figure 5-5. Schematic depicting typical interactions of the main rotor wake with the scan volume surrounding the tail rotor.

49

a) Measurement (flight test)

b) Calculation using simple wake model to compute tail rotor self-induced downwash

c) Computation using a free wake model to determine the tail rotor downwash

Figure 5-6. Azimuthal scanning polar plot of C_p at 2% chord on the Puma tail rotor at advance ratio 0.072. (40 steps per TR revolution in the computations.)

50

required, thus requiring roughly 5:1 time interpolation in the reconstruction. The reconstruction procedure outlined above was used to yield a high resolution description of the inflow induced by the main rotor wake on the tail rotor. By using reconstruction with 5:1 time interpolation, a reduction in CPU of over a factor of 100 was obtained relative to a direct calculation of the velocity field at the tail rotor disk.

The measured pressure at 2% chord over one revolution of the Puma TR blade is shown in Figure 5-6a, while the calculation for the initial case assuming a prescribed wake consisting of a skewed vortex helix (outlined above) is shown in Figure 5-6b. To supplement these results, a second calculation was undertaken using a freely distorting CVC wake to compute the influence of the tail rotor's wake; the result of using this downwash in the TR pressure calculation in place of the simple inflow is shown in Figure 5-6c. Clearly, the calculation using the free wake option produces a considerably more realistic prediction of the pressure coefficient than the simple inflow model, reflecting the importance of including the tail rotor's own wake in this calculation. This result is not surprising, given the relatively heavy loading on the tail rotor at the low advance ratio. This computational result confirms the experience of experimentalists working with the Puma TR data (Ref. 44), who have identified many distinct loading events in the Puma data that clearly arise from interactions of the tail rotor with its own wake.

The correlation achieved here is encouraging, though the differences with the measured results are clearly still substantial. These may well be due in part to the effect of the vertical fin, which lies roughly $0.5R_{TR}$ above the tail rotor disk and whose effect cannot be conveniently included in calculations of this type.

5.3.2 Correction for the Effect of the Main Rotor Shaft

One potentially important feature of MR/TR interaction involves accommodating the main rotor shaft effects on the wake. Such effects are especially significant for the wake filaments shed from the leading edge of the main rotor disk and convected downstream to impinge on the rotor shaft. This kind of vortex/surface interaction could in principle be modeled with a combination of an inner viscous region wrapping around the shaft surface and an outer inviscid region. Although there is presently no intention of resolving such complex interactions in the current context, it is important to take into account some of the gross rotor shaft effects on the wake filaments. Thus, a zone has been defined around the main rotor shaft such that any wake filaments convected through it will be removed permanently from the calculation. (This can be thought of as if defining a viscous zone around the shaft in which the vortex filaments are simply merged with the surface of the zone during the interaction). This crude model has been employed to delete spurious vortex/surface interactions in recent research of rotor-wake/fuselage interaction (Ref. 28) and has been adopted in RotorCRAFT/AA to delete spurious tail rotor interactions.

5.3.3 General Dual Rotor Capabilities

Though the discussion to this point has dealt primarily with tail rotor aerodynamics, the procedures evolved here can be applied to general dual rotor calculations. Tandem, side-by-side (tilt rotor), and coaxial configurations can be accommodated, within the restriction that a full dual free wake computation is not presently possible. The present method for dealing with such cases is an extension of the logic of the tail rotor case discussed above, though obviously the orientation and dimensioning of the rotor must be altered to suit the case of interest. Either rotor may adopt clockwise or counterclockwise rotation. Additional discussion is provided in Reference 45.

6.0 SURFACE PRESSURE COMPUTATIONS FOR ROTOR NOISE PREDICTIONS

The development of an efficient and accurate method for computing rotor noise was a topic of research at NASA/Langley in the 1980's (Ref. 15). One of the primary objectives of the present effort was to produce surface pressure output from RotorCRAFT/AA compatible with the input requirements of the acoustic program, WOPWOP, that resulted from this earlier work. WOPWOP was selected because of its robustness in analyzing general helicopter rotor configurations, and previous investigators have effectively validated WOPWOP by using experimentally measured pressures to accurately predict far field noise (e.g., Ref. 10).

The fundamentals of WOPWOP's acoustic analysis are based on Farassat's subsonic formulation of the Ffowcs Williams-Hawkings equation derived for the noise generated by surfaces in arbitrary motion. Assuming that the surface loading distribution is known beforehand, Farassat's scheme provides an effective prediction of noise generated by surfaces in subsonic flow. The scheme implemented in WOPWOP was specially tailored for the helicopter rotor acoustic problem, and both the blade motions and surface pressures are required inputs to the program. The surface pressures, in particular, must be accurately specified to a high degree of resolution to obtain good noise predictions.

Since prior versions of RotorCRAFT focused largely on the prediction of integrated aerodynamic loading that contributes to vibratory airloads, only a modest level of chordwise resolution was employed in these early calculations (typically one to five chordwise stations). A substantial increase in refinement is required to determine the detailed chordwise pressure distribution for input to WOPWOP. Substantial research work has been done to develop practical models for the accurate solution of high resolution surface pressures for acoustics applications (Refs. 46-49). Since many issues pertaining to the creation of a generally applicable model for unsteady loading remain unresolved, it was judged appropriate for current purposes to adopt a relatively simple model based on extending the existing vortex lattice blade load model to predict high resolution chordwise distributions of pressure. The following discussion provides background on prior investigations of this topic as well as on the distinctive new features of the current implementation.

6.1 Background

Investigations into the prediction of unsteady blade loading in the context of rotor aeroacoustics have been underway for several years. A variety of approaches have been taken for tackling this issue, including transfer function methods (Refs. 46 and 47) and computational analyses using full potential solvers (Refs. 48 and 49). Earlier in the development of the RotorCRAFT code, relatively simple analysis methods were implemented to allow a preliminary assessment of the ability of the code to predict rotor acoustics. A routine designed to provide the necessary interface was implemented in RotorCRAFT Mod 1.0 (Ref. 4) as a post-processor to the rotor wake calculation and was invoked after the convergence of the blade motion and loading solutions. The converged unsteady upwash predicted on each rotor blade (composed of the time-varying free stream and the unsteady wake contribution) was treated as an arbitrary gust. To find the lift response, each blade was segmented in the spanwise direction and each segment was treated as a two-dimensional flat plate airfoil. The Kussner function was used with the Duhamel superposition integral to evaluate the loading response of the airfoil to this simplified problem, in which the wake-induced velocity was treated as a time-varying gust.

This initial, simple model had several important limitations. For example, the basic transfer function approach assumed a two-dimensional linear wake extending far downstream of the airfoil. This particular limitation was relaxed by approximating the effect of the skewed helical wake of a rotor blade; the latter folds back on itself rather than extending to infinity, and thus adjustments were made to the analysis that effectively truncated the wake at a finite distance downstream of the blade. These adjustments were fairly crude, however, and a more refined approach has subsequently been implemented, as will be described shortly.

Moreover, the transfer function itself was essentially two-dimensional and thus was inappropriate for capturing tip effects or for modeling close blade/wake interactions. Finally, both the amplitude of the pressure response and the scaling of the nondimensional time were adjusted for compressibility using a Prandtl-Glauert type correction. In sum, this approach clearly required many approximations, but it did provide a useful first approximation to the unsteady surface pressure distribution on the rotor blades suitable for direct input to WOPWOP.

The present effort involved several steps designed to relieve these limitations. The surface pressure computation carried out here captures full 3D effects through the application of a refined vortex lattice treatment, employing additional quadrilaterals along the chord to yield sufficiently high resolution for input to WOPWOP; near wake terms were added to account for unsteady loading and improve the handling of wake truncation; a 3D version of the Prandtl-Glauert correction appropriate for a vortex lattice was used to address compressibility effects; and finally, an option for incorporating the effect of thickness was made available, building on a 2D source panel model. Additional research was carried out on still more advanced and novel methods for rotor blade load calculations that are candidates for follow-on implementation. The sections that follow address the major features of these modeling methods.

6.2 Unsteady Near Wake Effects

As discussed in Reference 2, the original model of the near wake just downstream of each rotor blade consists of a set of straight vortex trailers that are extended back into the wake from the bound vortices on the blade. The orientation of these trailers may adjust with the local free stream direction at a given radial station (Fig. 6-1), thus providing a coarse approximation of the behavior of the near wake suitable for the resolution of low-frequency loads; however, any other structure of the shed vorticity within this overlap region is neglected. The effect of the shed vorticity in the wake far downstream of the rotor blade is of course captured with the full-span CVC free wake model.

As part of the improvement of the aerodynamic model of the blade, a more refined treatment of the unsteady loading due to shed vorticity in the near wake has been incorporated, building on the preliminary studies described in Reference 4. The approach presently in place involves adjusting the downwash used to compute the loads on the vortex lattice with an approximate indicial function that captures the near wake effects. In principle, the downwash could be adjusted by explicitly including vortex elements in the near wake and laying out components of shed vorticity parallel to the blade span to supplement the trailers shown in Figure 6-1. This approach would involve a variety of computational difficulties, including the need to carefully position the discrete shed vorticity as a function of time step, and the necessity to incur a computational penalty associated with retaining high-resolution discrete vortex representations of the wake.
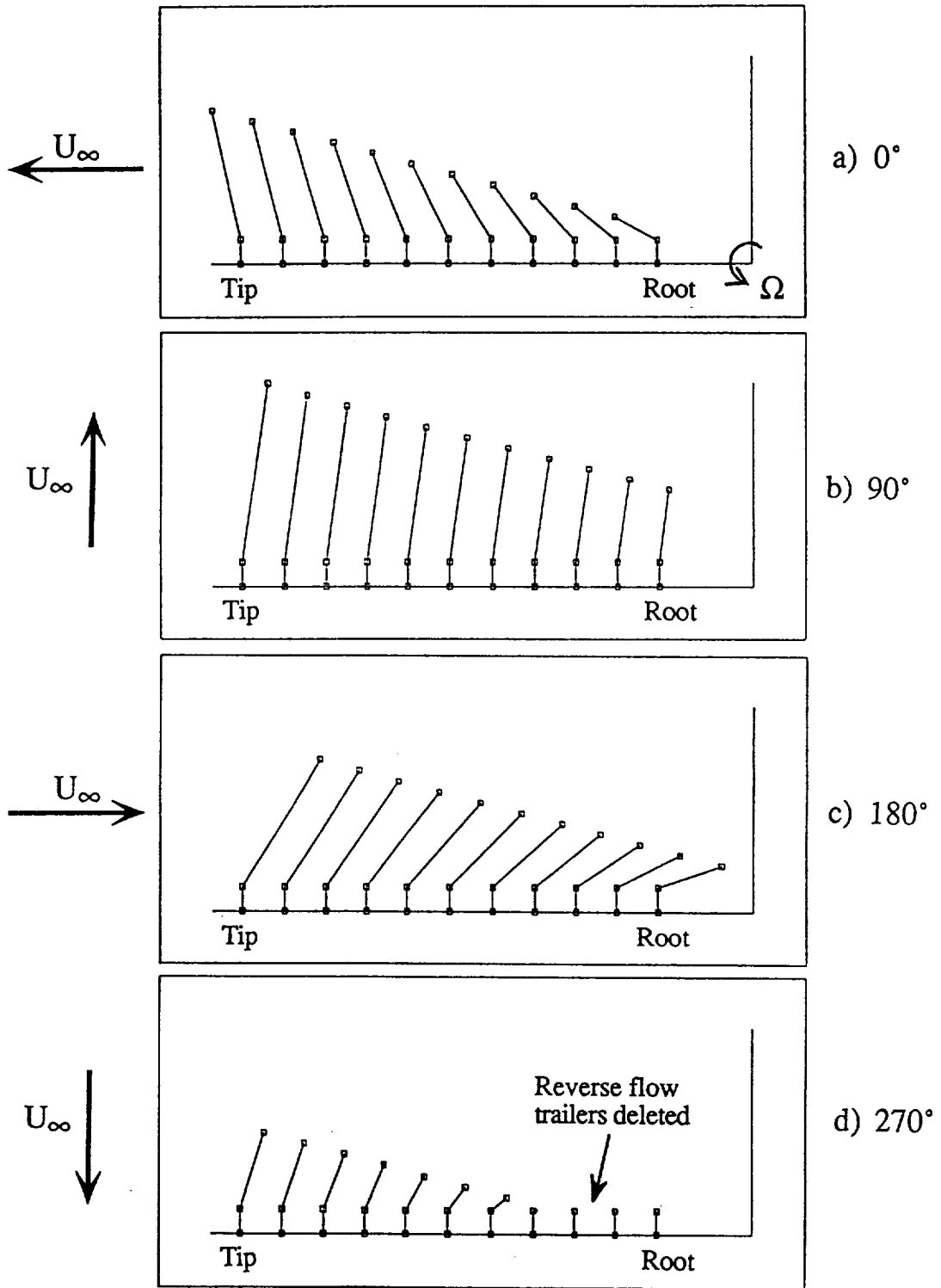
53

Figure 6-1. Schematic of bound vortex lattice and moveable near-wake trailing vortices in the overlap region: four azimuth angles for a rotor at advance ratio 0.4 .

54

Given this, it was judged desirable to use an indicial function to compute the lift response of the rotor blade to the shed vorticity in the near wake. This approach is implemented in the vortex lattice method as part of the calculation of the induced velocity at a control point. Let w represent the downwash at a typical control point due to the influence of the wake and the blade motion. The modification required to take account of near wake unsteady effects can be formulated as a correction to the downwash w ; the resulting quantity w* will be used to compute the bound circulation distribution and can be stated as:

$$w^*(s) = w \; \Phi_{rt}(s, s_T, N) \qquad (6\text{-}1)$$

where s is the nondimensional time and Φ_{rt} is an indicial function that reduces to 1.0 in the case where near wake shed vorticity is omitted. The nondimensional time here is s=(Ut/c), where the reference velocity U is assumed to be

$$U = \Omega r + U_\infty \sin\psi \qquad (6\text{-}2)$$

for a given radial position r and azimuth station ψ, and U_∞ is the free stream velocity. If ψ_{ovl} is the extent of the overlap near wake (Fig. 6-1), then s_T is the nondimensional time at which the blade occupied the azimuthal position ψ - ψ_{ovl}. T is the time elapsed during one blade azimuth increment and N is the number of azimuth increments contained within the overlap region.

The indicial function assumes that the downwash at the control point varies linearly from zero over the time step T, reaching its full value at that point. The present vortex lattice scheme assumes essentially a step increase in downwash at each time step that does not generate any shed vorticity in the overlap near wake. The indicial function Φ_{rt} is designed to add in the effect of this near wake while also including the effect of its truncation beyond ψ_{ovl} so as not to double-count the wake that is captured by the CVC model.

In the case of the present rotor wake analysis, the downwash is desired at discrete multiples of the time step T (which is assumed to be ramp time s_T) :

$$w^*(ns_T) = w \; \Phi_{rt}(ns_T, s_T, N) \qquad (6\text{-}3)$$

The indicial function can be constructed from

$$\Phi_{rt}(0, s_T, N) = 0$$

and

$$\Phi_{rt}(ns_T, s_T, N) = \Phi_0(ns_T, s_T) + \sum_{m=1}^{\infty} \Phi_m(ns_T, s_T, N) \qquad (6\text{-}4)$$

55

where

$$\Phi_0 (s, s_T) = 0$$

for $s < s_T$ and

$$\Phi_0 (s, s_T) = 1 + \frac{1}{s_T} \ln \left(\frac{s-s_T+2}{s+2} \right) \tag{6-5}$$

for $s \geq s_T$. The term Φ_m is determined by a recursion relation

$$\Phi_m (ns_T, s_T, N) = \sum_{k=1}^{n-mN} \left\{ \Phi_{m-1} ([k+(m-1)N]s_T, s_T, N) - \Phi_{m-1} ([k-1+(m-1)N]s_T, s_T, N) \right\} *$$

$$\Phi_w ([n-mN+1-k]s_T, s_T, N) \tag{6-6}$$

for $n > mN$ and

$$\Phi_m (ns_T, s_T, N) = 0$$

for $n < mN$. The term Φ_w in Equation 6-6 is given by

$$\Phi_w (s, s_T, N) = 0$$

for $s < s_T$, while the term

$$\Phi_w (s, s_T, N) = \frac{1}{(2N+1)s_T} \left[1 + \frac{1}{s_T} \ln \left(\frac{s-s_T+2}{s+2} \right) \right] - \frac{2}{(2N+1)s_T} \frac{(2s + 2 + (2N-1)s_T)}{(2s + 4 + (2N-1)s_T)} \frac{(s - s_T)}{(2s + (2N-1)s_T)} +$$

$$\frac{2 (\ln [(s - s_T+2) (2s + 2 + (2N-1)s_T)] - \ln [2(2N+1)s_T])}{4(s+2)^2 + 4(s+2)(2N-1)s_T + (2N-1)^2 s_T^2} \tag{6-7}$$

The primary effect of this type of indicial function is to introduce a phase delay into the response of the aerodynamic loading while also decreasing the magnitude of the response to a given upwash or blade motion input. It has been included in the sample computations discussed in Section 7.

6.3 Extended Lifting Surface Modeling

A variety of options were considered for the prediction of the chordwise distribution of pressure on the blade surface, including transfer functions more sophisticated than the flat plate treatment mentioned in Section 6.1. These methods are fundamentally 3D extensions of the Sears function, long used to compute the lift response of 2D airfoils to sinusoidal gusts. Later investigators (e.g., Ref. 50) extended this work to infinite span wings immersed in an oblique gust field. Typically, such fields are characterized by characteristic wavelengths or frequencies in the directions parallel and

perpendicular to the span of the wing (Fig. 6-2). The form of the pressure response function for a rectangular planform is

$$\Delta p(x,y,k_x,k_y) = 2\pi\rho U W(k_x,k_y)\, G(x,k_x,k_y)\, e^{i(k_y y - k_x U t)} \qquad (6\text{-}8)$$

for any point (x,y) on the planform surface. Here, U is the local freestream velocity, ρ is the free stream density, W is the Fourier decomposed vertical gust velocity, and G is an airfoil response function. A modified form derived for use in rotors and propellers is given by Amiet in Reference 46. Amiet's model has been applied both to rotors and to main-rotor/tail-rotor interaction by Tadghighi (Ref. 47), and taking this approach to pressure prediction here was one possible approach to the prediction of unsteady surface pressures.

In general, linearized unsteady flow analyses evolve from the imposition of flow tangency conditions on lifting surfaces, along with appropriate companion conditions on conservation of circulation in unsteady flow and the Kutta condition. It was noted during the course of this effort that an extension of the existing vortex lattice model would be a candidate approach for chordwise resolution of loads due to the vortex passage; moreover, implementation would be simplified since a time domain formulation could be retained. The solution method used to find the bound circulation given this lattice is similar to classical approaches described in the literature on lattice methods for fixed wing and rotary wing applications (e.g., Refs. 51 and 52). Each of the quadrilaterals is examined individually and a mean vector normal to the quadrilateral surface is established as shown in Figure 6-3, which also shows the location of the 'control point' associated with the quadrilateral. Given this and the location and orientation of each of the quadrilaterals on the blade, the velocity induced by the blade lattice on each of the control points is determined, assuming unit strength for each quadrilateral. Then the resulting velocity is resolved in the normal direction at each control point, yielding an array of influence coefficients relating the vector of bound circulations, γ , to the downwash, w , at each control point:

$$\mathbf{w} = A\gamma \qquad (6\text{-}9)$$

where

$$A = \frac{\partial w_i}{\partial \gamma_j} \qquad i,j = 1,....n \qquad (6\text{-}10)$$

Here, n is the number of vortex quadrilaterals on the blade.

This array of coefficients is stored and the velocity induced at each control point by the free stream, the blade rotation and deflection, and the rotor wake are summed and resolved into 'normal-wash' velocities that are then used to find the vector γ of bound circulation values on the disk as follows:

$$q_j = (q_{\text{free stream}})_j + (q_{\text{wake}})_j + (q_{\text{blade}})_j \qquad (6\text{-}11)$$

57

$$k_x \equiv \frac{2\pi b}{\lambda_x}$$

$$k_y \equiv \frac{2\pi b}{\lambda_y}$$
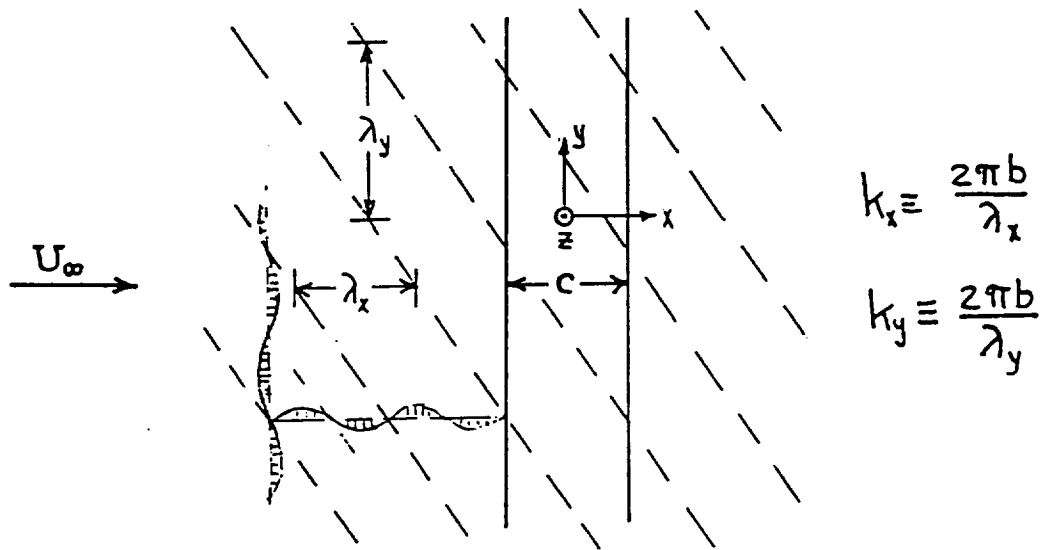
Figure 6-2. Plan view of wing orientation and characterization of the incident gust field for typical unsteady aerodynamic transfer function analyses for lifting wings of chord c(=2b).

Normal vector at $\vec{X}_c$ is $\vec{n} = \vec{R}_1 \times \vec{R}_2$

$$\vec{X}_c = 0.25\left(\vec{X}_1 + \vec{X}_2 + \vec{X}_3 + \vec{X}_4\right)$$
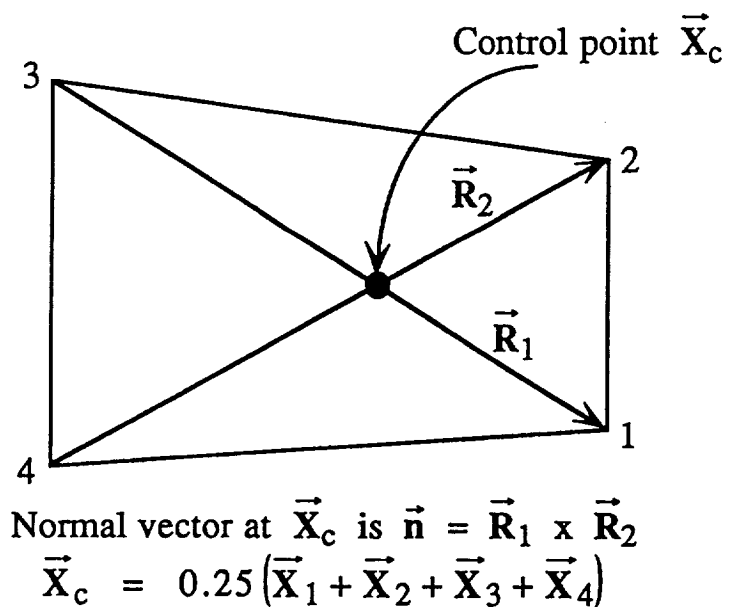
Figure 6-3. Typical vortex quadrilateral, showing the corner indices and diagonal vectors. Control point found using the mean of the corners. Normal vector defined as indicated.

58

The wake-induced velocity computation of course includes the unsteady velocity due to the vortex passage.

$$w_j = q_j \cdot n_j \tag{6-12}$$

$$\gamma = A^{-1} w \tag{6-13}$$

The vector γ can then be used to solve for the load distribution on each segment of the blade by applying the following expression for each the four edges of the vortex quadrilaterals, i.e.,

$$F_{jk} = \rho \, \gamma_j (q_{jk} \times s_{jk}) \ell_{jk} \, , \qquad j = 1,...n \qquad k = 1, 2, 3, 4 \tag{6-14}$$

Here, s_{jk} is the unit vector directed along edge k of quadrilateral j ; ℓ_{jk} is the length of this side, while γ_j is the strength of the quad. The reference velocity q for the evaluation of forces is computed at the midpoint of the edge k. This velocity contains all the components deriving from the free stream, the wake, the motion of the blade, and the velocity induced by the entire vortex quadrilateral grid, though the influence of the segment on which a particular point lies is deleted. The pressure distribution over the surface is obtained summing the total force on each quad F_j and dividing by the area of the quadrilateral.

This approach was judged to be convenient and desirable in view of the pre-existing lattice analysis within the RotorCRAFT/AA code, as well as the recent addition of the unsteady near wake model described in the previous section. One potential drawback to this is that conventional vortex lattice computations become computationally expensive when applied to blade surfaces with a high density of chordwise vortex quadrilaterals (e.g., ten or more). Since such densities are required to yield adequate resolution of chordwise pressure distributions for WOPWOP, this can pose a fundamental constraint, owing to the high computational cost of computing the wake-induced flow field at each control point, as well as the inversion of the matrix A required to find the circulation strength of each quadrilateral. These costs can be circumvented as follows:

- first, flow field reconstruction is applied to compute the wake-induced velocities; this greatly reduces the number of full wake-on-blade velocity evaluations required to complete a full revolution;

- second, the matrix inversion for the high density lattice is only performed over one blade revolution during reconstruction once the wake configuration and blade dynamics have already converged to the final result. In this way the reconstructed airloads and surface pressures both gain improved resolution without incurring the huge increase in CPU that would be associated with utilizing the high density lattice throughout the original RotorCRAFT calculation.

This approach has made practical calculations involving up to 500 vortex quadrilaterals distributed over the blade surface. This allows adequate resolution of the major features

59

of blade/vortex interaction events, though further improvements are required, as will be discussed in Section 7.

6.4 Corrections for Thickness

The thin surface analysis described above solves for the difference in upper and lower surface pressure on the airfoil. However, it is of interest in some circumstances to directly compute the pressure on these surfaces. This option has been provided through the implementation of a 2D source panel program that computes the pressure perturbations due to the local section profile. The panel code used is drawn from Reference 53 and has been validated for several NACA profiles. The implementation of this feature of the model is discussed in Reference 45.

6.5 Alternate Singularity Methods for Unsteady Compressible Blade Modeling

As part of the present effort a compressible unsteady lifting surface method was examined for applicability to rotorcraft blade aerodynamics calculations. The point-doublet method (Refs. 54 and 55), which is basically an acceleration potential method, was studied. In its basic form this method uses aerodynamic doublet singularities with an infinite flat wake. Previously, point-doublet had been used successfully to analyze oscillating wings in subsonic and supersonic flow, though prior to this work, the oscillation frequencies to which the method had been applied were relatively low.

To apply the method to rotor blades several issues needed to be addressed. In the present CVC method, a prescribed near wake is used to assure the proper relationship between the blade aerodynamics control points and the near field of the CVC trailing vortices. When the blade is modeled by a vortex lattice of this type, the prescribed wake models only trailed vorticity, and the shed wake is handled by a local quasi-two-dimensional transfer function that includes the effect of prescribed wake truncation. Compressibility is handled by a local Prandtl-Glauert stretching. The advantages of the point-doublet method are that unsteadiness and compressibility are handled more formally and consistently within the context of linear potential flow aerodynamics. To apply point-doublet to rotor blades, the infinite wake must be replaced by a truncated wake (Fig. 6-4) and the effects of blade rotation should be incorporated.

As part of the current effort, research was undertaken to apply the point-doublet method to rotor blade aerodynamics. As a first step, a wing aerodynamics code using point-doublet was implemented. Test cases with this wing code indicated some significant shortcomings of the method originally described in Reference 54 in the parameter range suitable for rotorcraft applications. Although the point-doublet method is fairly simple in principle, there are several mathematical subtleties associated with the derivation of the kernel function. In previous work the doublet distribution was first integrated in the chordwise direction, thereby constructing the doublet equivalent of horseshoe vortices. The resulting kernel function involves integrals that could not be evaluated directly but were evaluated by a series expansion method. In addition, for control points directly behind upstream doublets the integral exists only in the Mangler sense. It was found that the series representation of the kernel function behaved poorly in terms of convergence for higher oscillation frequencies and for high aspect ratio wings. The high aspect ratio and higher frequency cases are in the range applicable to rotorcraft. Apparently, this parameter range had not been previously tested, since the original interest in the method was associated with low aspect ratio wings at relatively low induced frequency (less than unity). Failure of the series representation of the kernel function was associated with the need to take a very large number of terms in the series,

Taken together
these two look
like a vortex, net
circulation $+\Gamma_4-\Gamma_3$

Taken together
these two look
like a dipole, net
circulation $+\Gamma_2-\Gamma_2 = 0$

Horseshoe Vortex

Vortex Quadrilaterals
approach a dipole (or
doublet) row in the limit
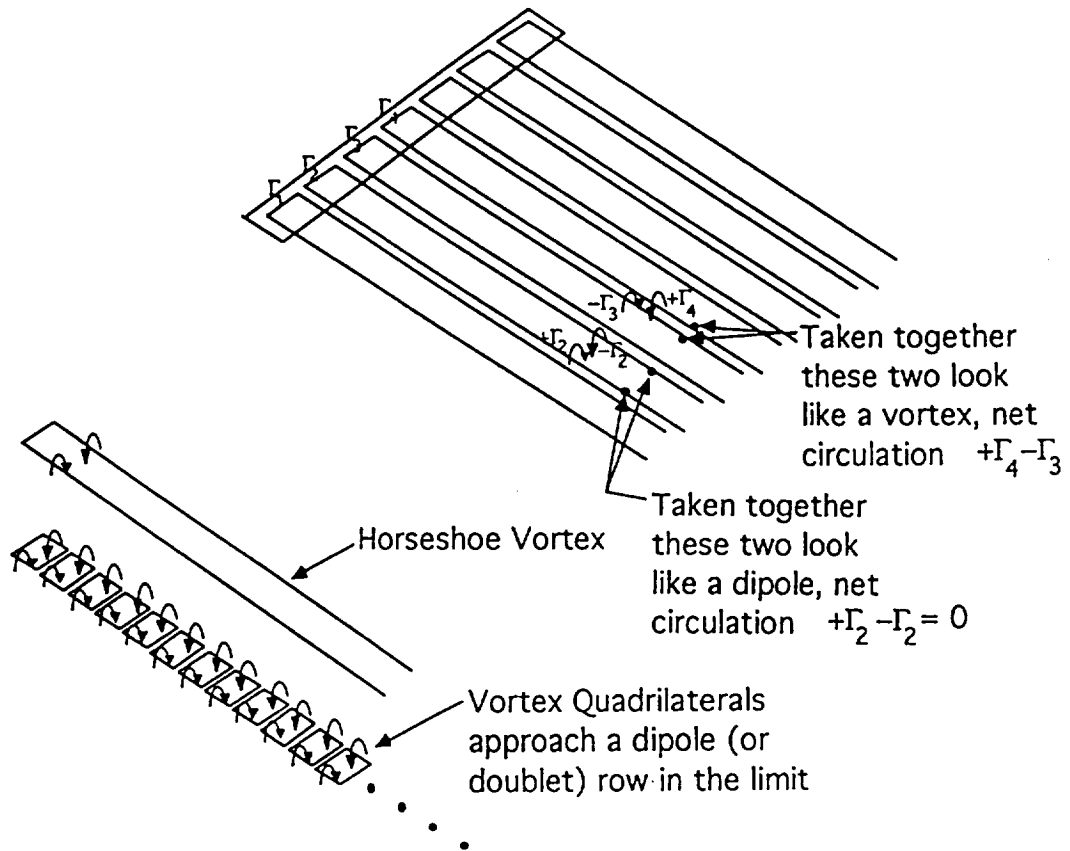
a) Equivalence between vortices and doublets on lifting blades

Point Doublets

Const. Vorticity Contour
Free Wake Model
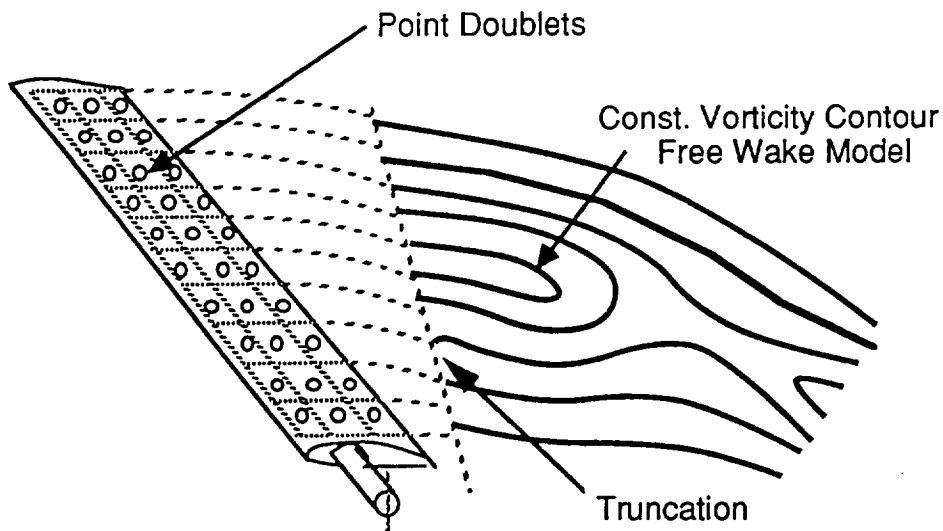
Truncation

b) Truncation of the near wake for coupling to rotor wake model

Figure 6-4. Schematic of the application of point doublet methods to calculation of rotor blade loading.

61

extremely rapid divergence of the series, and difficulty in quantifying the parameter space in which this failure occurs.

After considerable study, it was concluded that the above shortcomings of the method could only be resolved by a basic reformation of the kernel function. The original series approach responsible for the difficulties was replaced by a new treatment in which a portion of the integrand in the kernel function representation was replaced with a curve fit. This curve fit employed functions that rendered the integrand. This undertaking amounted to a redevelopment of the entire point-doublet method. The new kernel function has been extensively checked-out over a wide range of frequencies and aspect ratios and behaves well everywhere. Because of the closed-form nature of this new solution there are no issues of convergence or range of applicability. In addition, the new kernel function expressions are of a fairly simple form, and are computationally very efficient.

Because of a need to redevelop the entire method, it was not possible to implement the point-doublet method into the present version of RotorCRAFT/AA. However, the method is now ready for implementation in follow-on versions of the code. If this implementation is undertaken, the results should be an improved treatment of blade compressibility and unsteadiness, particularly in the tip region where the combined effects of three-dimensional flow and compressibility are particularly pronounced..

7.0 EXAMPLE PROBLEMS IN FLOW FIELD AND AIRLOAD RECONSTRUCTION

7.1 Summary of Test Database Configurations

To demonstrate the capabilities of the reconstruction analysis, several sample calculations have been undertaken. Previous efforts in this direction (Ref. 3) focused on correlating RotorCRAFT predictions with available wind tunnel and flight test data (Refs. 19-21). Results obtained from these correlation studies provided encouraging evidence of the ability of the RotorCRAFT code to capture important features of vibratory airloads and illustrated the importance of applying appropriately sophisticated models to the prediction of wake-induced loading.

Since the completion of the baseline RotorCRAFT version, two comprehensive data sets have become available that contain combined airload, noise, and structural data on modern rotor designs. The first of these was drawn from tests carried out in the DNW tunnel on a 1/5th scale model of the Boeing Model 360 main rotor (Ref. 56). This rotor is a four-bladed design with -9.32 degrees of nonlinear twist as well as a planform that tapers .321:1 outboard of 0.9R. Major characteristics of the planform and the test are shown in Table 7-1. The tests covered a wide variety of flight configurations, but the results made available for correlation work here included three test points: Test Point 63, advance ratio 0.2 with a shaft angle of attack of 0 deg.; Test Point 66, advance ratio 0.2 with a shaft angle of attack of 4 deg.; and Test Point 193, advance ratio 0.3 with a shaft angle of attack of -3.4 deg. The former two points simulate moderate advance ratio cases in descent, with substantial BVI loading; the latter is representative of a high speed cruise flight condition.

TABLE 7-1

Model Blade Geometry for the Boeing 360 Rotor

Radius (in.)	=	60.619
Inboard chord (in.)	=	5.285
No. blades	=	4
Tip taper	=	.3206
Taper initiation (r/R)	=	0.9
Cutout, r/R	=	.268
Airfoils:		
Tip r/R = 1.0		VR-15
r/R = .268 to .85		VR-12
Hover M_{TIP}		0.636
Natural freqs.:		
1st flap		2.62P
2nd flap		4.68P
3rd flap		7.52P
1st torsion		5.25P

The second rotor test was described in References 57-59, and was also carried out in the DNW tunnel. Here, a 1/5.73 scale model of the four-bladed Sikorsky UH-60A

main rotor was tested. The planform and twist distribution are sketched in Figure 7-1 (from Ref. 59). The blade planform has 20 deg. of sweep outboard of 0.929R and a nearly constant chord. Other major characteristics of the planform and the test are shown in Table 7-2. The flight conditions tested featured a wide range from low advance ratio in descent to high speed cruise. The cases tested here focused on advance ratios 0.15, 0.2, and 0.3.

TABLE 7-2

Model Blade Geometry for the Sikorsky UH-60A Rotor

Radius (in.)	=	56.28		
Chord (in.), airfoil:				
r/R	=	.122 to .466	3.625	SC1095
r/R	=	.497 to .823	3.661	SC1095R8
r/R	=	.854 to 1.0	3.625	SC1095
No. blades	=	4		
Cutout (r/R)	=	0.122		
Hover M_{TIP}	=	0.636		
Tip sweep (deg.)	=	20		
Sweep initiation (r/R)	=	0.929		

Test computations that follow focus on integrated normal force and sectional thrust predictions, first undertaken for cases without the application of airload reconstruction, then with reconstruction in place to address the resolution of selected high frequency loading events. Following this, predictions of noise will be described using the interface with NASA's WOPWOP code.

7.2 Rotor Load Correlation Studies: Baseline Cases without Reconstruction

The initial calculations carried out here were designed to be representative of the results that could be expected from the RotorCRAFT/AA code without the application of airload reconstruction. For some of the cases studied, the additional time resolution offered by the application of reconstruction is necessary to resolve certain high frequency events in the rotor blade loading.

7.2.1 Boeing 360 Model Rotor

The test calculations undertaken for the BV360 rotor focused on two flight conditions, corresponding to Test Points 63 and 66 for the experimental study described in Reference 56. The actual test data was obtained with the aid of Boeing Helicopters personnel. The major model inputs for this case were as follows:

- each blade was represented by a lattice of 34 vortex quadrilaterals distributed across the span, with one chordwise. Sensitivity studies suggested this to be adequate for resolution of predicted airloads consistent with the time steps used in these initial computations.

Upper Planform

Lower Planform

0.0   0.2   0.4   0.6   0.8   1.0

Radius, r/R

· Pressure Transducers
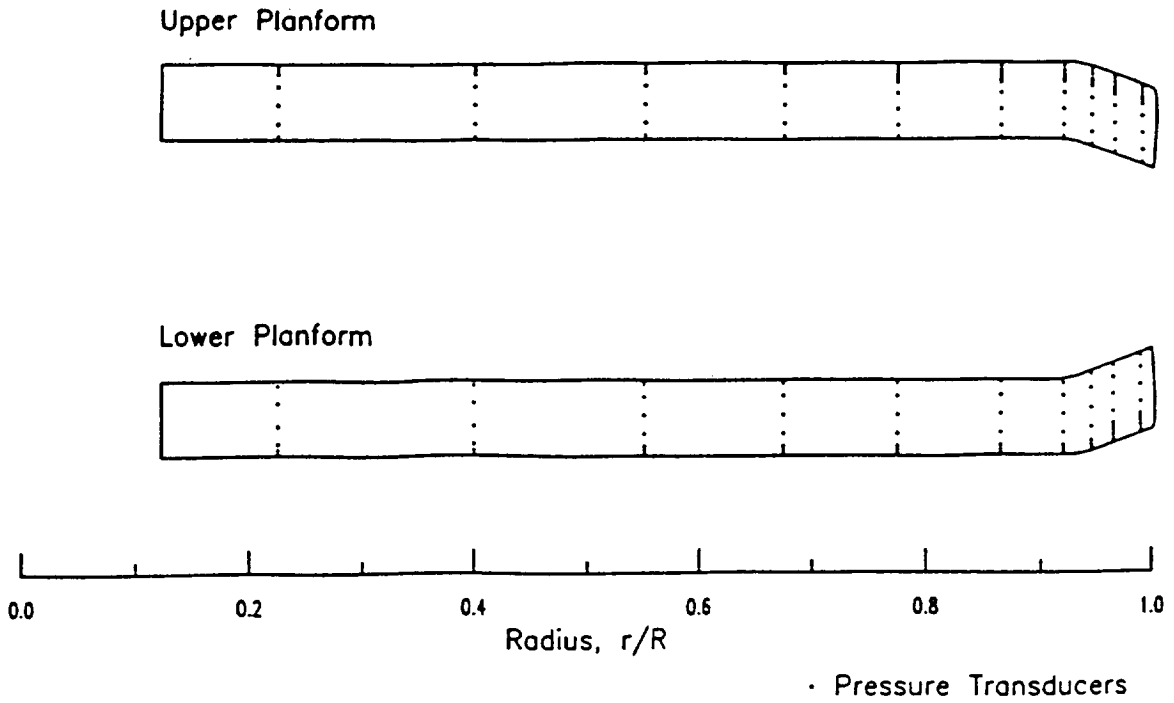
a) Plan view
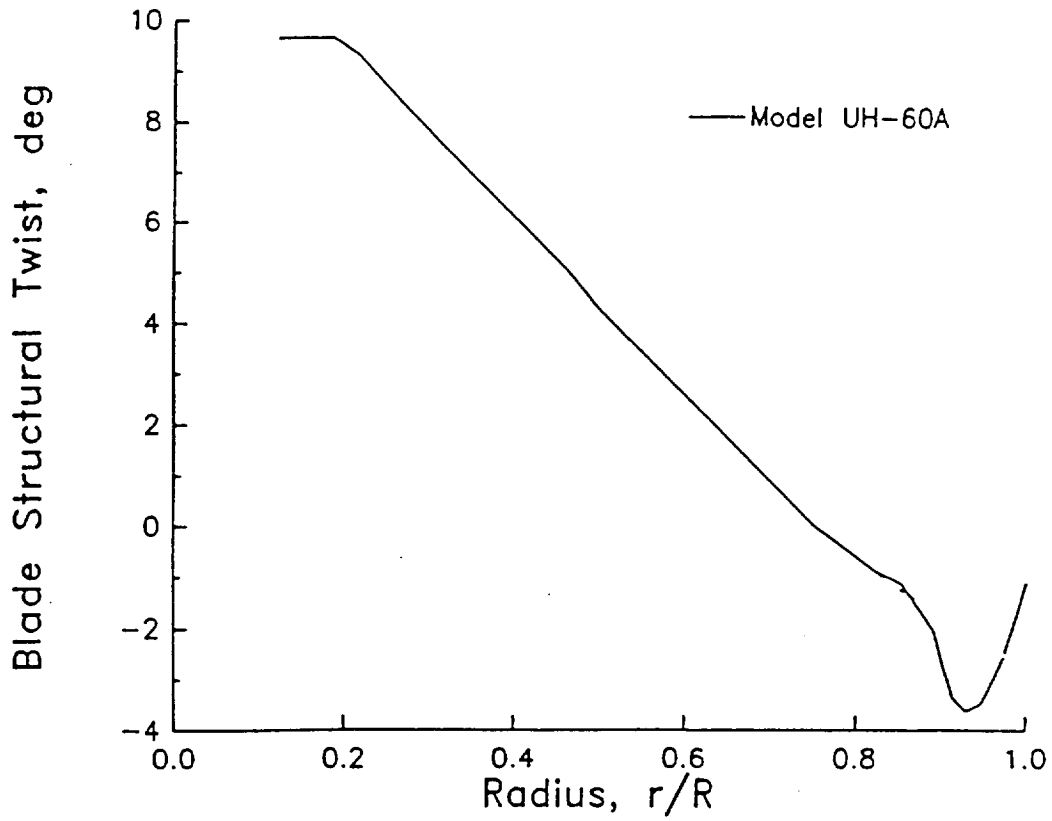
b) Geometric twist distribution

Figure 7-1. Planform characteristics of UH-60A model rotor blade.

- the blade dynamics model included six dynamic modes, four for out-of-plane bending, one in torsion, and a rigid lag mode. The computed natural frequencies compared favorably with those shown in Table 7-1.

- the wake was discretized by using two turns of full-span CVC wake. A maximum of fourteen CVC trailers was used for the Zone 1 wake (see Ref. 22), with default vortex core sizes (Ref. 3).

For the cases discussed, a time resolution of 48 steps per blade revolution was used. Though four to five rotor revolution periods typically sufficed to allow the calculation to converge, ten revolutions were used as a matter of course.

Figure 7-2 shows the comparison of measured and predicted normal force coefficient for three radial stations (r/R = 0.8, 0.88, and 0.95) for Test Point 63, which involves an advance ratio of 0.2, a thrust coefficient of 0.00694, and a shaft angle of attack of 0 deg. The comparison of the data at r/R = 0.8 shows close agreement, while the comparison becomes less favorable for stations farther outboard. Note, however, that the shape of the predicted and measured loading is quite similar in all three cases. This type of offset in loading suggests that it may be some gross aspect of the blade motion that is not captured by the computation. It is clear, however, that an abrupt loading event occurs in the third to fourth quadrants, and that the phasing and magnitude of this event is well captured.

Figure 7-3 shows the comparison for the same advance ratio and thrust but for a shaft angle of attack of +4 deg., a setting that promotes close wake interaction with the rotor blade. This again is particularly evident in the fourth quadrant, where several sharp spikes in loading are clearly evident. Smaller "ripples" in the loading appear in the first quadrant. This type of feature is clearly a candidate for improved resolution through the application of reconstruction. The 7.5 deg. azimuth step used here captures the gross features of the unsteady loading but fails to reproduce these high frequency events. The overall correlation with test data has been found to be quite good at this level of temporal resolution.

Figure 7-4 presents snapshots at four different azimuths of the wake trailing from one of the 360 model rotor blades for Test Point 66. These snapshots illustrate BVI events that are likely causes of the high frequency loading ripples observed in the data shown in the previous figure. The darker vortex filaments represent vorticity trailing from the tip region of the rotor blade while the lighter filaments represent vorticity trailing from the inboard wake. The inboard and outboard wake filaments have opposite sign vorticity.

Figures 7-4a and 7-4c show typical BVI events associated with high frequency loading response in the fourth quadrant of the data. These BVI occur when an individual blade successively passes through the tip vorticity trailed from the preceding blades. The parallel encounter shown in Figure 7-4c causes the large high frequency perturbation near azimuth angle 315 degrees found in the prediction and the data.

Figures 7-4b and 7-4d show BVI events associated with high frequency loading response in the first quadrant of the data. Figure 7-4d shows that in the first quadrant, unlike the fourth quadrant, the trailed root vorticity contributes to the interaction as well as the tip vorticity. Though the magnitude of the high frequency peaks are smaller in this quadrant, (as seen in Fig. 7-3), the acoustic response has been found to be quite sensitive to high frequency events occurring at this location in the blade azimuth. Therefore,
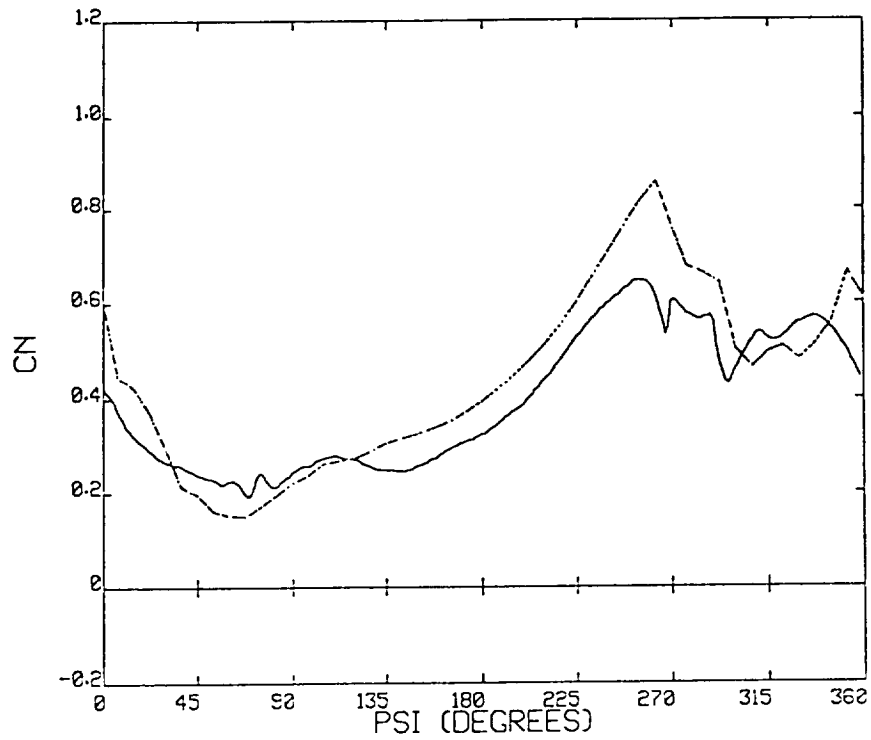
a) r/R = 0.80
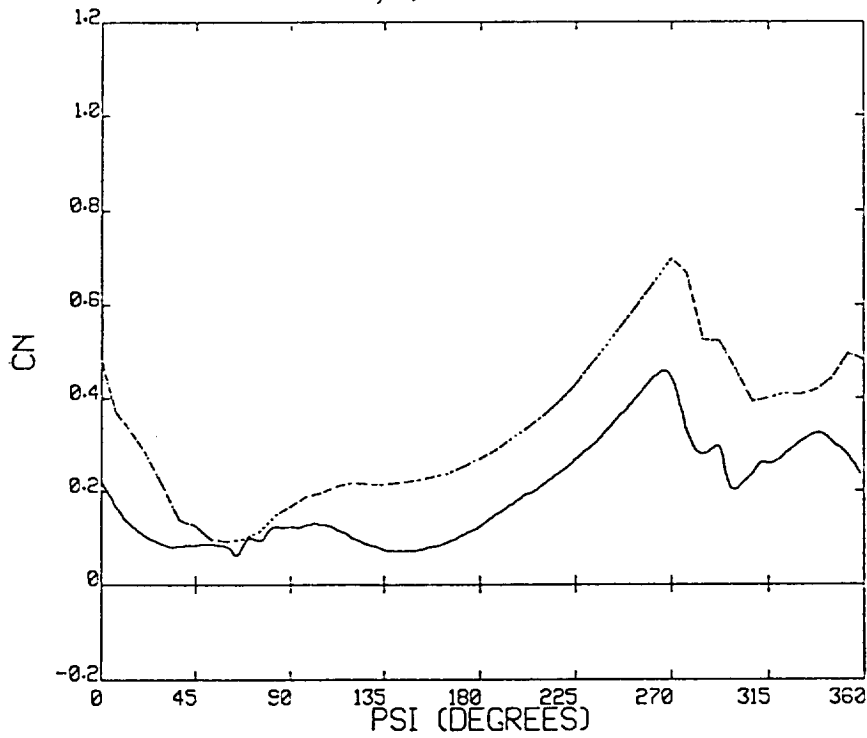
b) r/R = 0.88

Figure 7-2. Boeing 360 rotor normal force coefficient calculations, Test Point 63: advance ratio . 0.2 , shaft angle = 0 deg. (solid = measured, dotted = predicted).
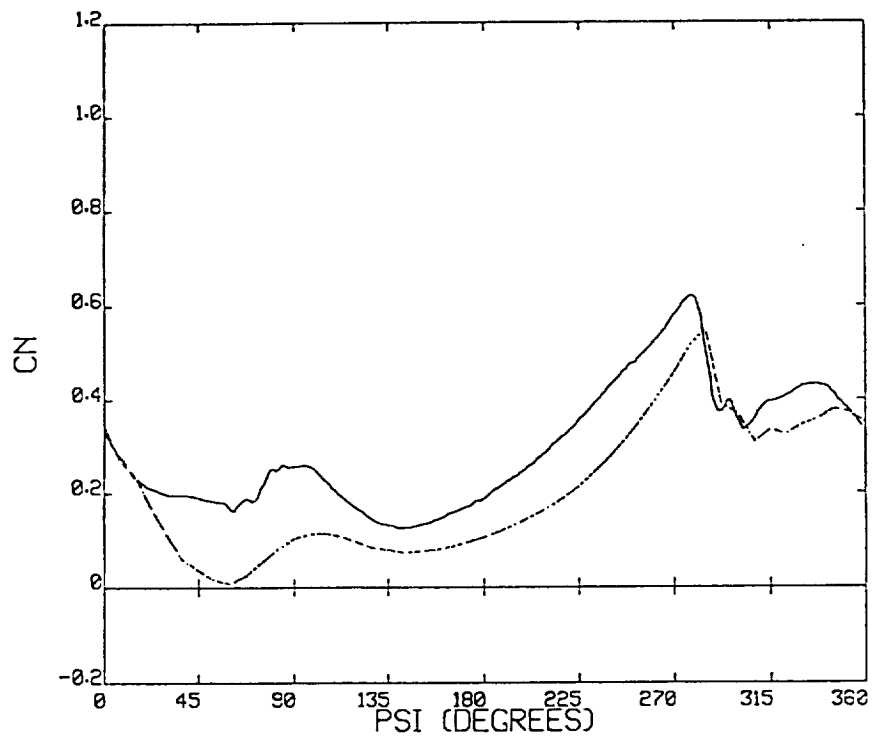
c) r/R = 0.95

Figure 7-2 (Cont'd). Boeing 360 rotor normal force coefficient calculations, Test Point 63: advance ratio 0.2 , shaft angle = 0 deg. (solid = measured, dotted = predicted).

68
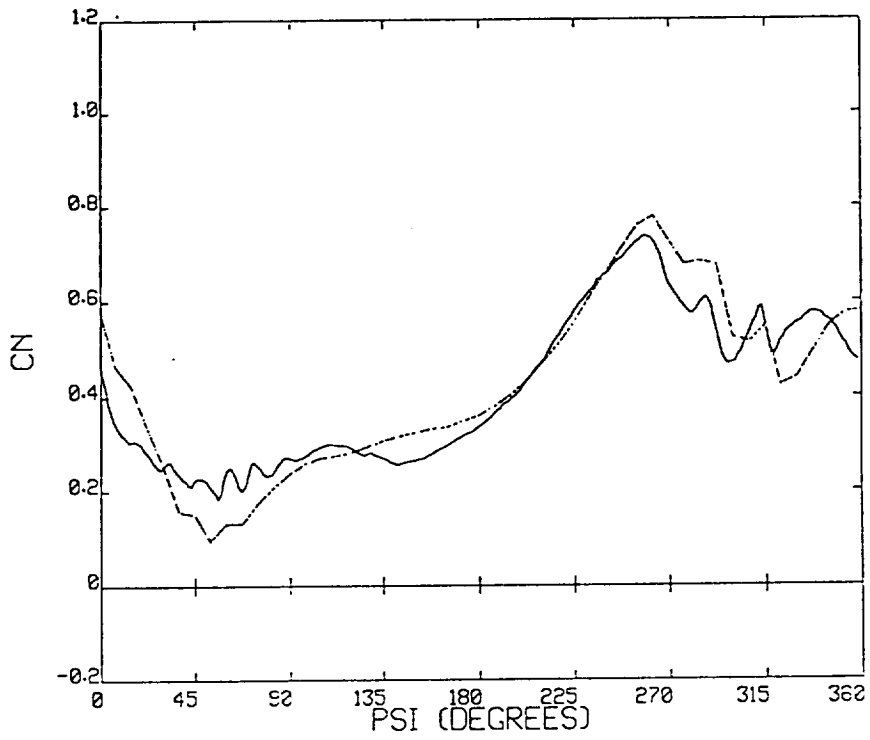
a) r/R = 0.80
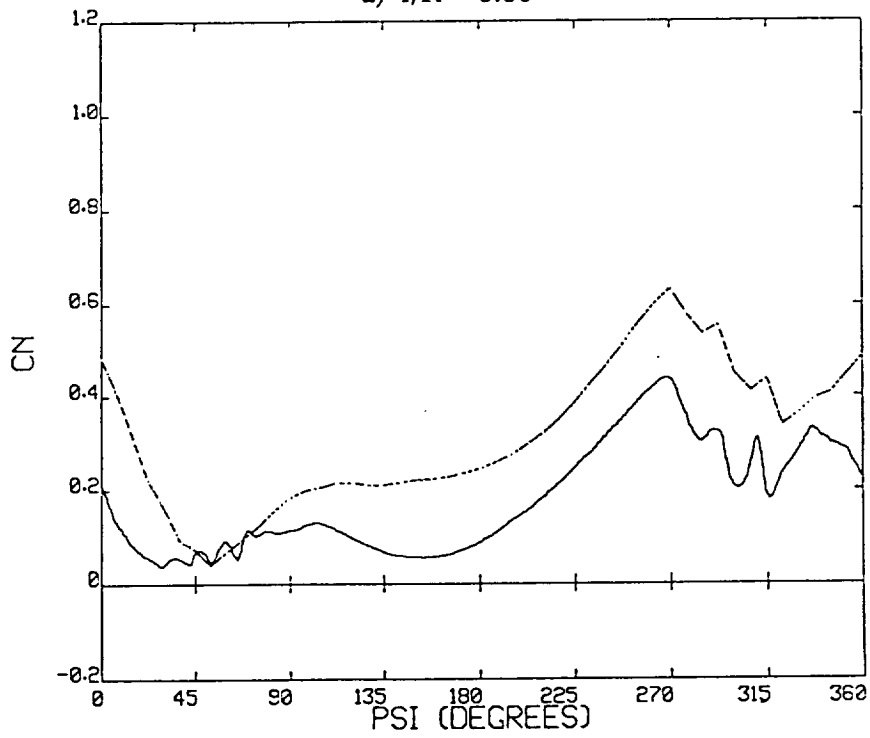
b) r/R = 0.88

Figure 7-3. Boeing 360 rotor normal force coefficient calculations, Test Point 66: advance ratio 0.2 , shaft angle = 4 deg. (solid = measured, dotted = predicted).
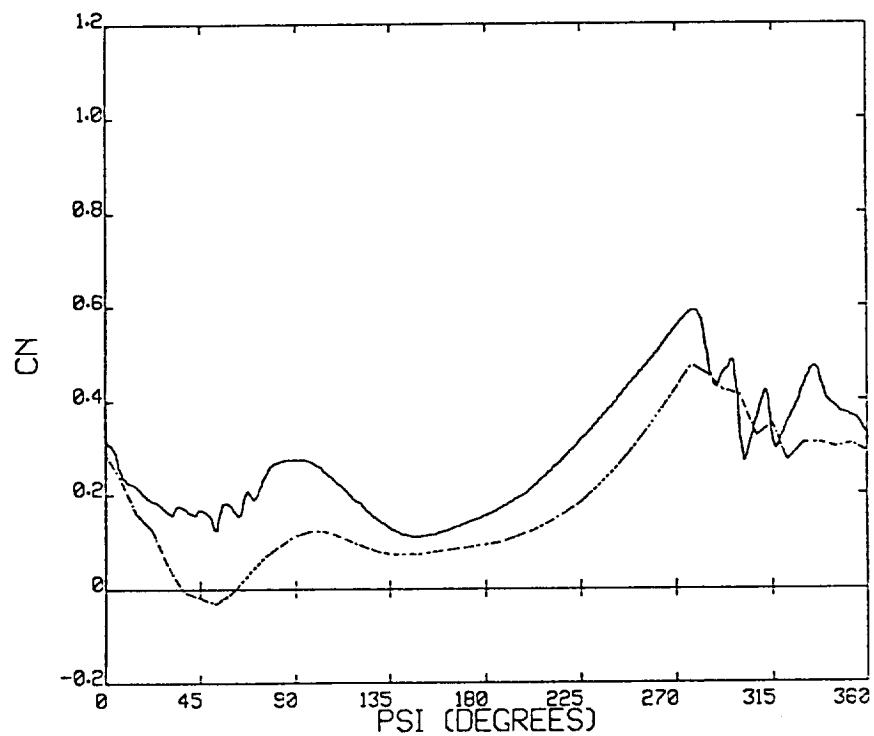
c) r/R = 0.95

Figure 7-3 (Cont'd). Boeing 360 rotor normal force coefficient calculations, Test Point 66: advance ratio 0.2 , shaft angle = 4 deg. (solid = measured, dotted = predicted).
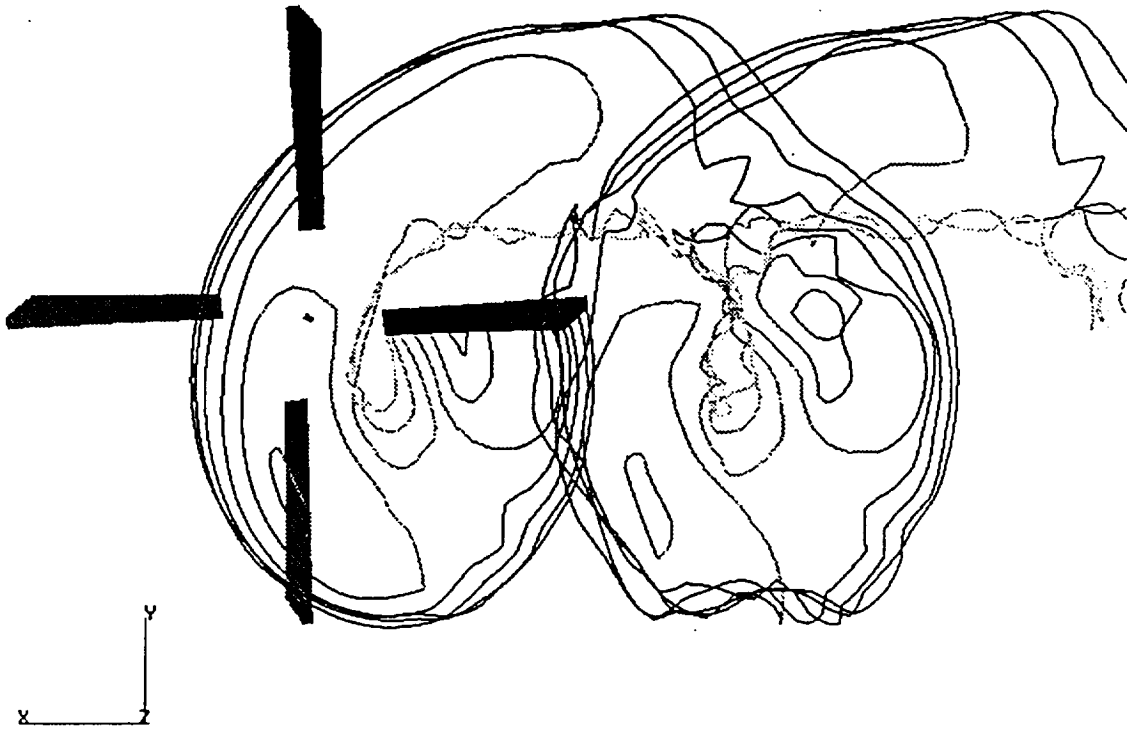
a) Reference blade at $\Psi = 0°$
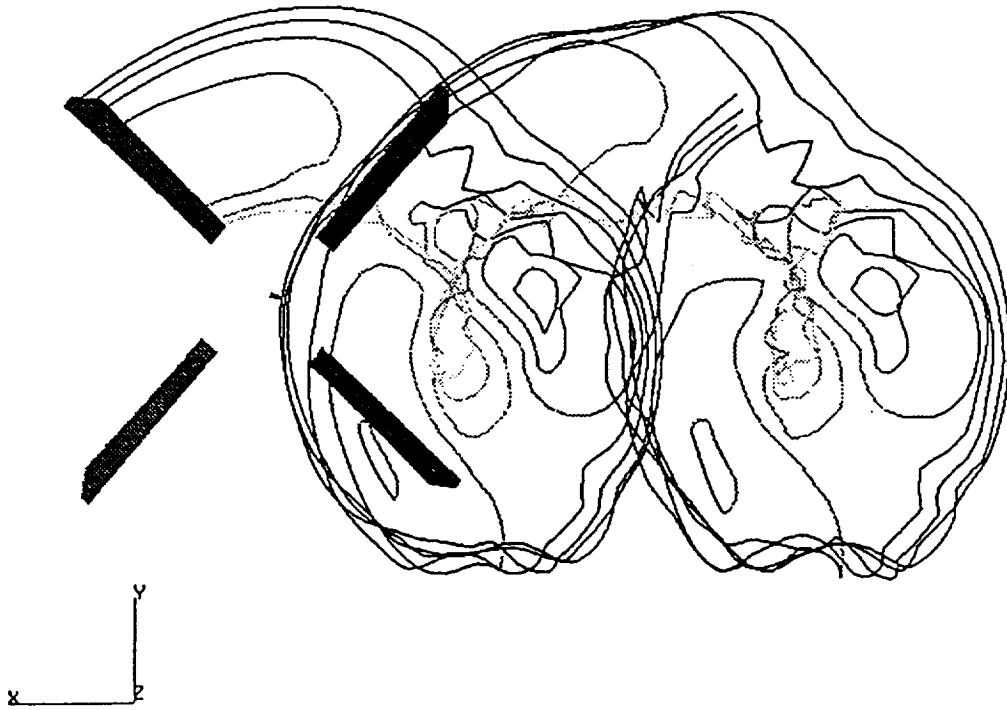
b) Reference blade at $\Psi = 135°$

Figure 7-4.   Top view of CVC wake for the Boeing 360 rotor, Test Point 66.
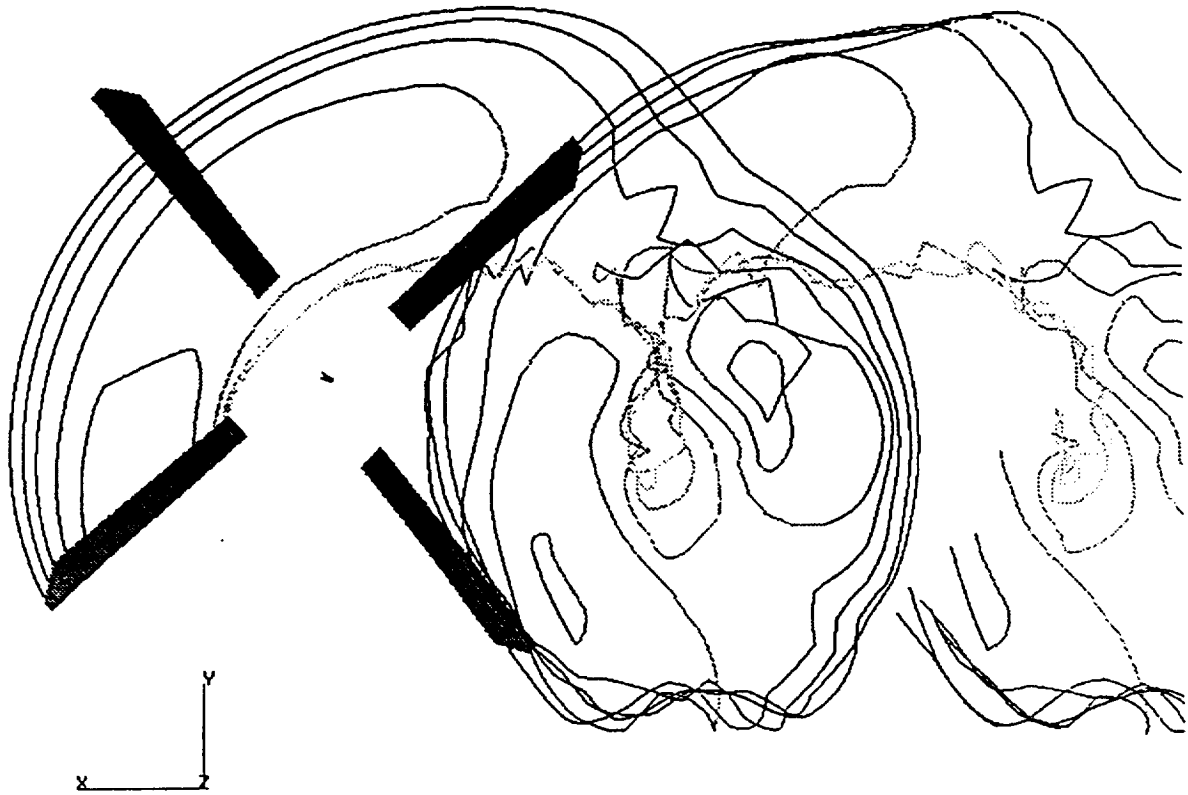
c) Reference blade at $\Psi = 225°$
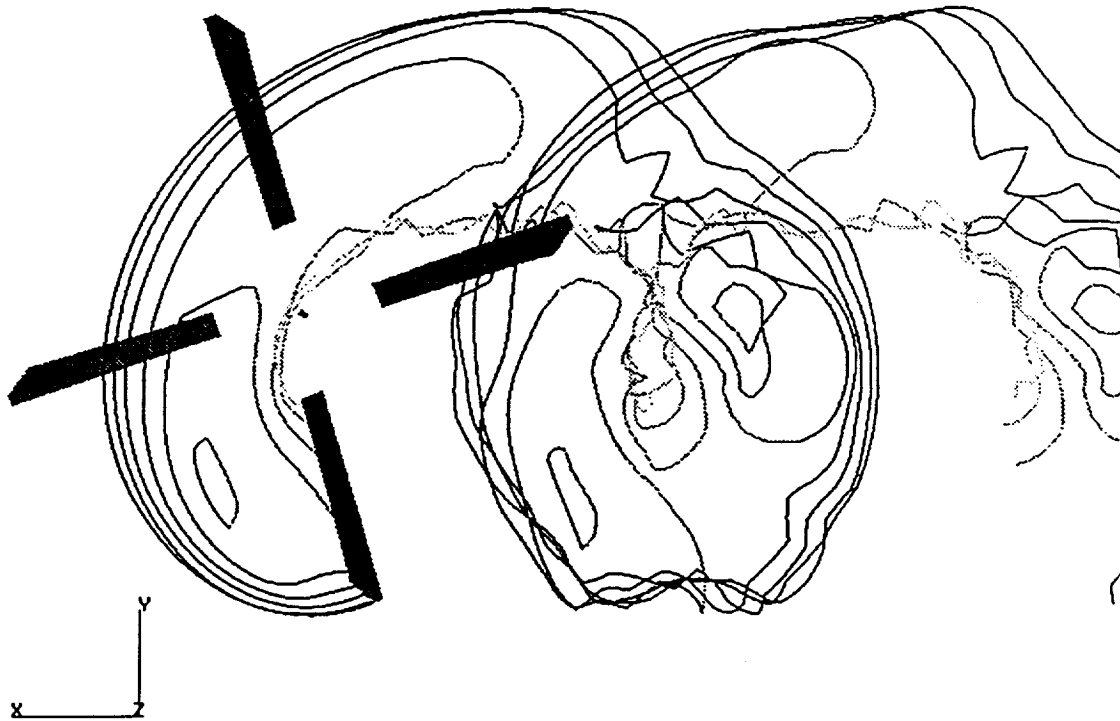
d) Reference blade at $\Psi = 292.5°$

Figure 7-4 (Cont'd).   Top view of CVC wake for the Boeing 360 rotor, Test Point 66.

accurate modeling of these first quadrant events is essential for effective prediction of rotor generated noise.

7.2.2 UH-60A Model Rotor

For the case of the UH-60A model rotor, the computations carried out below modeled the planform with 15 segments of piecewise linear twist to represent the distribution shown in Figure 7-1. The rotor blade planform has a nearly constant chord with the tip section outboard of the 92.9% radial station swept back 20 deg. The computations used 46 vortex quadrilaterals on the blade span to capture the aerodynamic loading, with one in the chordwise direction. The structural model of the blade included 16 finite elements using cross-sectional properties taken from Reference 59. A total of six dynamic modes were included in the model. The presence of substantial tip sweep caused the torsion and flap modes to be coupled. Thus, though the model nominally uses four flap (out-of-plane bending) modes, two torsion modes, and one (rigid) lag mode, the highest frequency "flap" mode and the two torsion modes are in fact coupled flap-torsion modes.

Several operating conditions were examined to study the ability of RotorCRAFT/AA to capture the major features of rotor blade loading. The three conditions to be shown here are from runs 1126, 1137, and 1311. The flight conditions in detail were:

- 1126: advance ratio 0.15, $C_T/\sigma = 0.071$, shaft angle = 5.5 deg.
- 1137: advance ratio 0.20, $C_T/\sigma = 0.070$, shaft angle = 4.0 deg.
- 1311: advance ratio 0.30, $C_T/\sigma = 0.071$, shaft angle = 1.0 deg.

The hover tip Mach number for the rotor was 0.636 in each case.

The first computation focused on advance ratio 0.15. The correlation of airload predictions with test data is shown in Figures 7-5a to 7-5c for three radial stations. With the exception of the boundary between the second and third quadrants ($\Psi = 180$ to 225 deg.), the overall correlation is very good. However, once again several of the high frequency ripples in the first and fourth quadrant are not captured. The discussion later in this section will illustrate the utility of reconstruction for this purpose.

Figure 7-6 shows the results obtained for the case of advance ratio 0.2 (Test Point 1137). Again, the major features of the rotor loading are captured around the azimuth, with the exception of loading far around in the second quadrant. Also evident here is some evidence of a possible role played by the inboard wake in determining unsteady loads in the first quadrant. Careful correlation of wake visualization and blade loading time history has established that the loading events in the first quadrant are due to encounters with rolled-up vorticity trailing from both the tip and the inboard portion of blades upstream of the interaction. The wake geometry evident in Figure 1-1 suggests this type of feature. The ability to resolve such structures is one of the strengths of the CVC wake model, a strength that has been noted in prior data correlation efforts (Refs. 12 and 60).

Figure 7-7 addresses Test Point 1311, a rotor at advance ratio 0.3. Here, an important and apparently intractable issue becomes apparent. It has been noted in previous studies of rotor airload correlation with the UH-60 data base (Ref. 48) that predicted rotor blade loading at cruise conditions becomes inaccurate in part because of
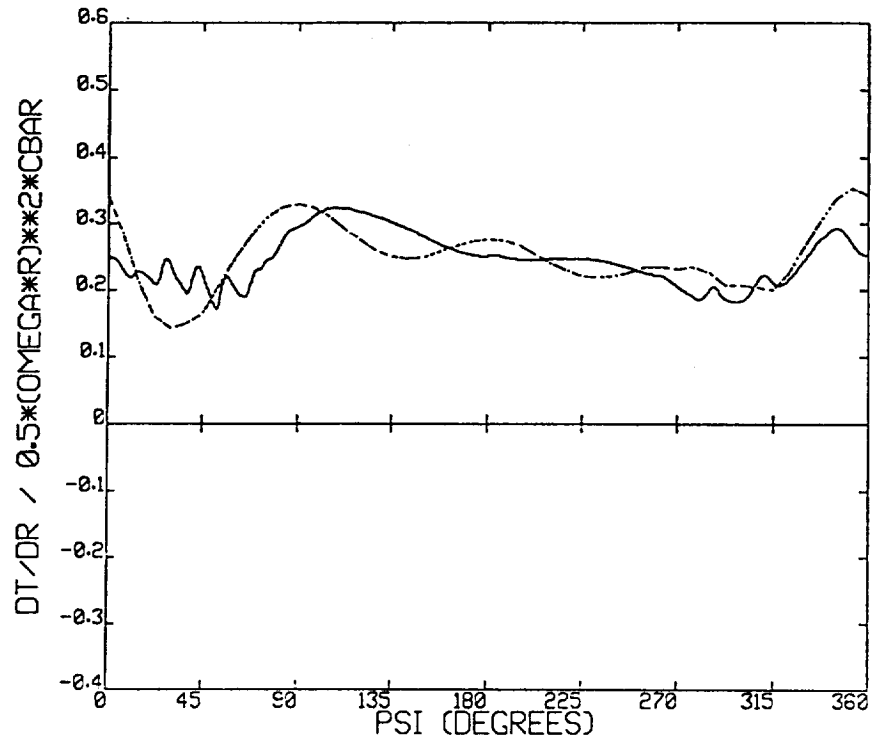
a) r/R = 0.675
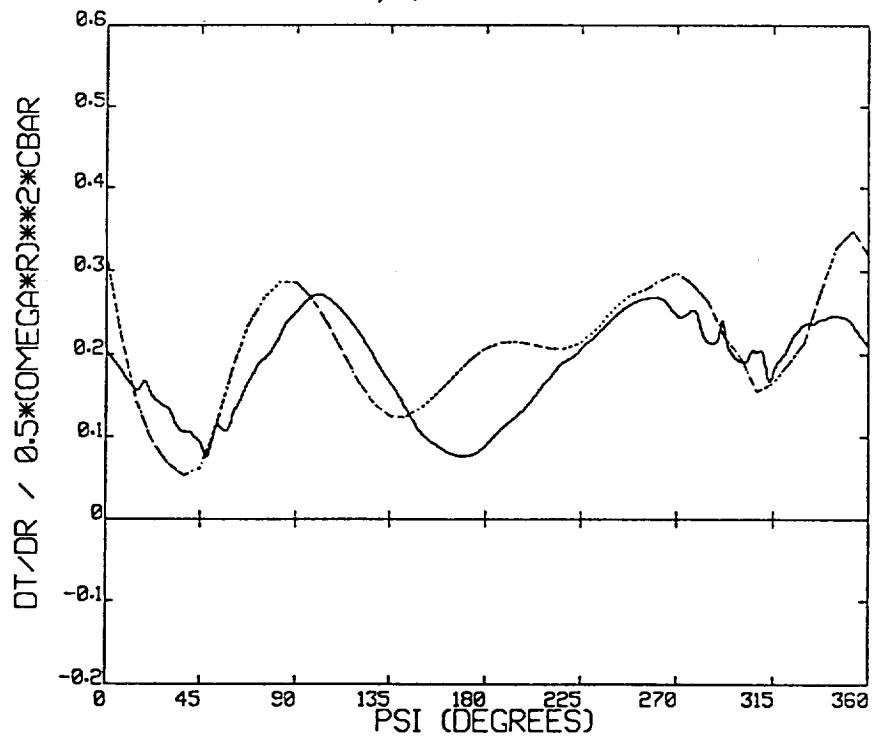
b) r/R = 0.865

Figure 7-5. Sikorsky UH-60A model rotor nondimensional thrust coefficient dC_T/dx, Test Point 1126: advance ratio 0.15, C_T/σ = .070 (solid = measured, dotted = predicted).
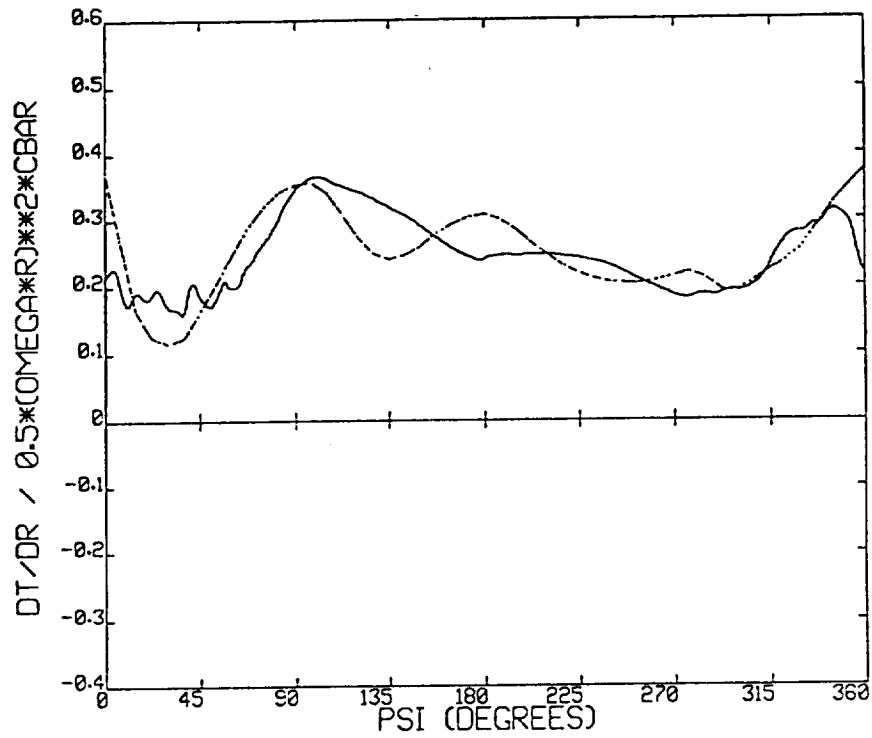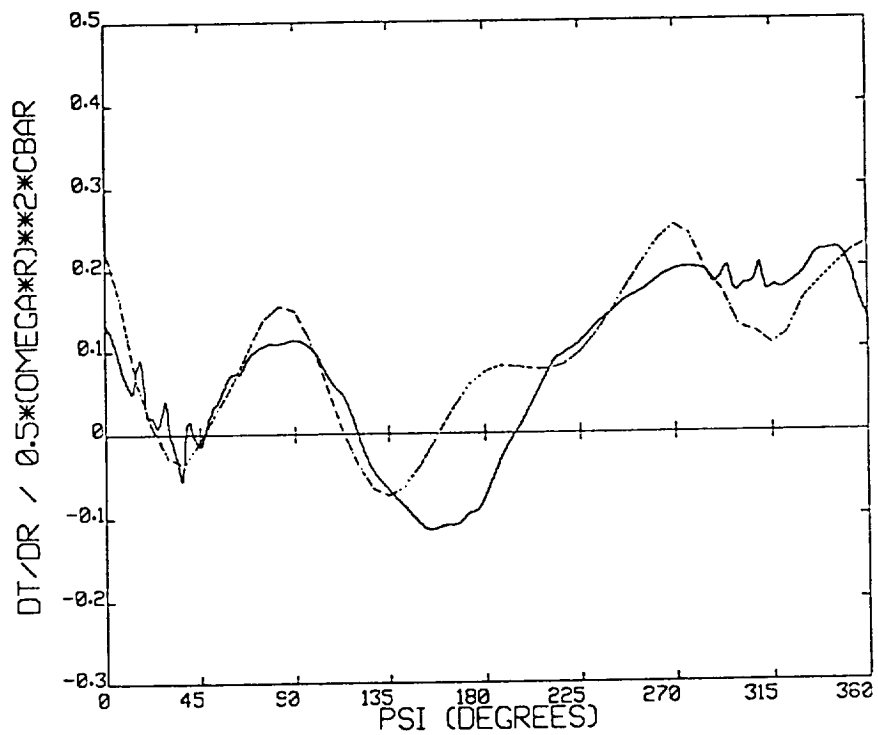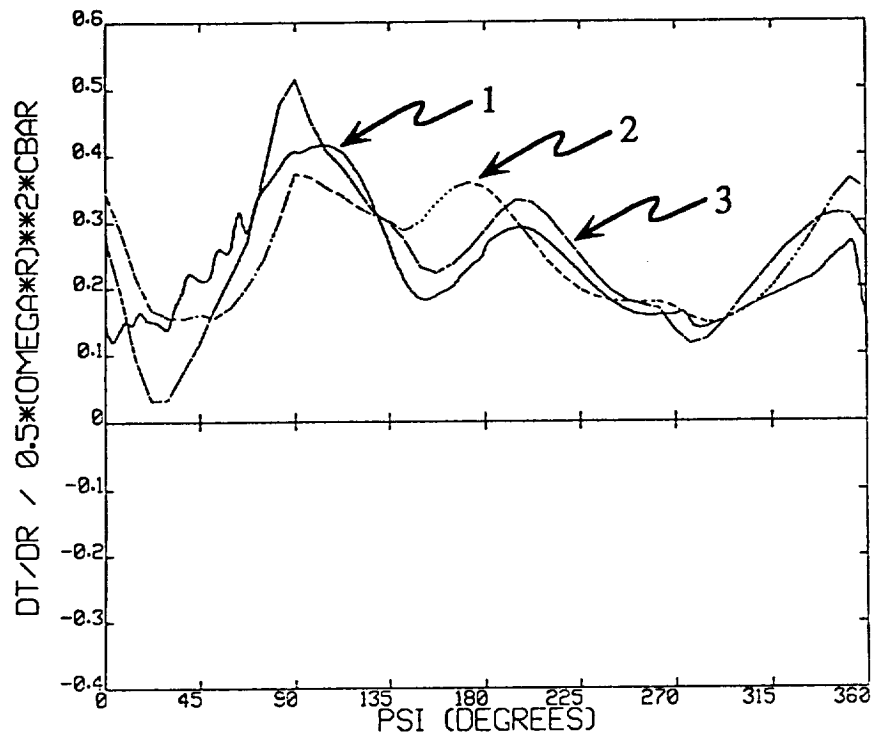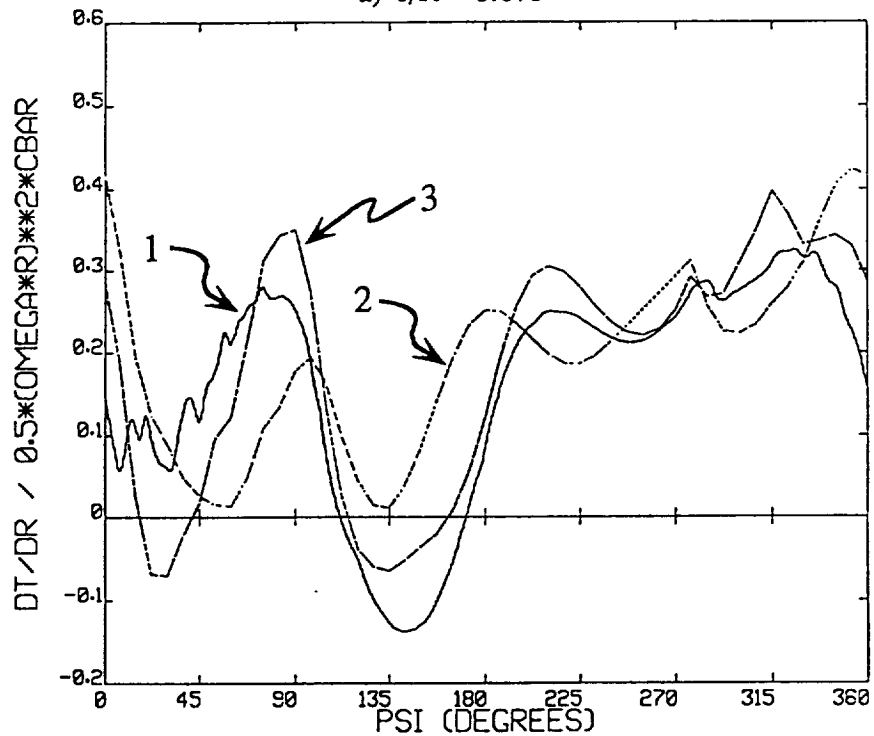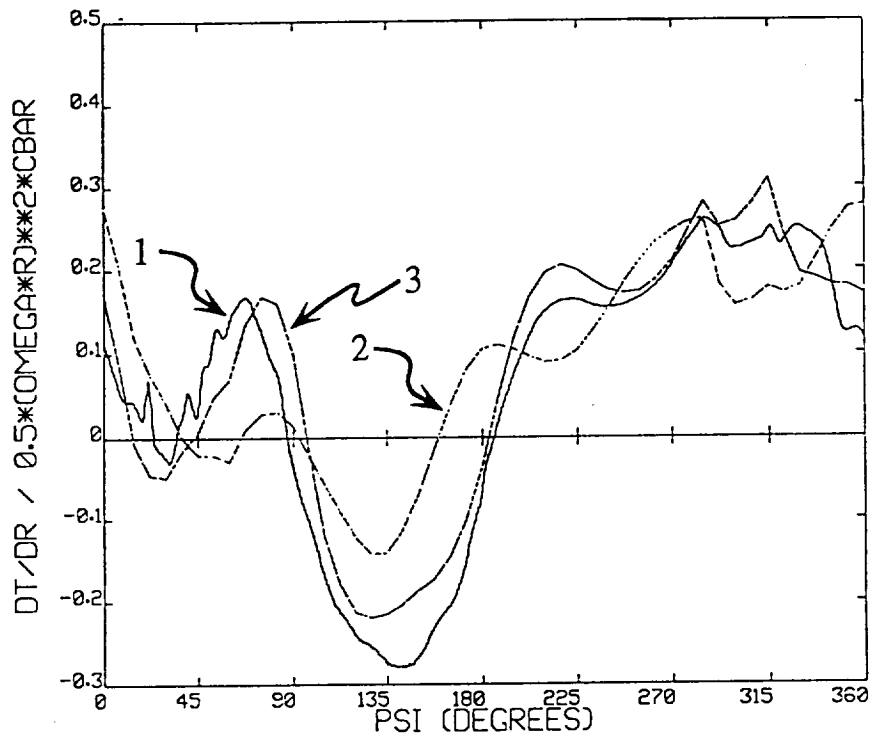
c) r/R = 0.965

Figure 7-5 (Cont'd). Sikorsky UH-60A model rotor nondimensional thrust coefficient dC_T/dx, Test Point 1126: advance ratio 0.15, $C_T/\sigma = .070$ (solid = measured, dotted = predicted).

a) r/R = 0.675

b) r/R = 0.865
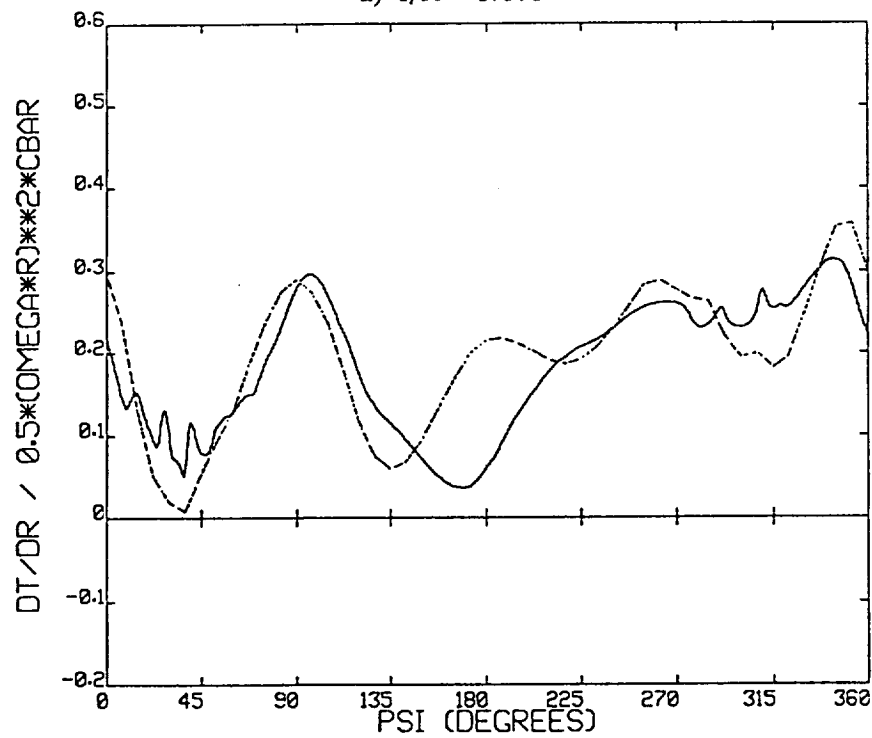
Figure 7-6. Sikorsky UH-60A model rotor nondimensional thrust coefficient dC_T/dx,
Test Point 1137: advance ratio 0.20, $C_T/\sigma = .070$ (solid = measured,
dotted = predicted).

c) r/R = 0.965

Figure 7-6 (Cont'd). Sikorsky UH-60A model rotor nondimensional thrust coefficient dC_T/dx, Test Point 1137: advance ratio 0.20, $C_T/\sigma = .070$ (solid = measured, dotted = predicted).

a) r/R = 0.675

b) r/R = 0.865

Figure 7-7. Sikorsky UH-60A model rotor nondimensional thrust coefficient dC_T/dx, Test Point 1311: advance ratio 0.30, $C_T/\sigma = .070$ (1 = measured, 2 = predicted, 3 = predicted with measured torsion).

c) r/R = 0.965

Figure 7-7 (Cont'd). Sikorsky UH-60A model rotor nondimensional thrust coefficient dC_T/dx , Test Point 1311:   advance ratio 0.30 , C_T/σ = .070 (1 = measured, 2 = predicted, 3 = predicted with measured torsion).

the inability to accurately predict the blade's torsional deflection. Moreover, it has been shown that even given the measured airloads, industry-standard dynamics analyses do not produce satisfactory predictions of torsional stresses or deflections for the UH-60A model blade (Ref. 61). The plots in Figure 7-7 show clearly that the baseline prediction using RotorCRAFT/AA shares this type of difficulty. However, if the predictions are modified by prescribing the blade motion to the extent of specifying the torsional deflection, then the overall agreement improves dramatically. Take particular note of the markedly improved correlation at r/R = .965.

The ultimate source of this problem is at present unclear; it may be attributable to a shared but subtle shortcoming in the dynamic models applied to date, or it may reflect an undocumented or unappreciated feature of the fabrication or deflection of the UH-60A wind tunnel model. In any event, recent flight tests on a full-scale UH-60 aircraft may shed light on this issue.

It is of interest to note the effect of selective refinement of the wake model. Consider, for example, the prediction of loading for Test Point 1126. There exists within the RotorCRAFT/AA code an option to suppress the interaction of the wakes of each blade on each other while retaining the effect of the wake of a given blade on other filaments trailed from that blade; the flag used within the code to denote this expression is NWAKES = 0. It was noted during the course of the investigation that for rotors at moderate forward speed, it is important to use the full free wake calculation to ensure maximum accuracy in the blade loading prediction. Figure 7-8 is included to illustrate this point. It shows the considerable improvement in the magnitude and phasing of first quadrant loading if NWAKES=1 (full free wake calculation) is used.

Figure 7-9 presents snapshots at four different azimuths of the wake trailing from one of the UH-60A model rotor blades for case 1137, (advance ratio = 0.2). These snapshots illustrate BVI events similar to those previously discussed for the 360 model. Figures 7-9a through 7-9c offer excellent examples of the successive fourth quadrant blade/vortex interactions responsible for the rippling effect seen in the data. Also evident is the first quadrant BVI with both root and tip vorticity which is important when predicting rotor unsteady loading. The oblique views in Figure 7-10 show the intensity of the BVI associated with the root vorticity for this rotor configuration.

7.3 Airload Computations with Reconstruction

Several calculations were undertaken to illustrate the application of the analysis with airload reconstruction in place. As is evident from the results already presented, the low-resolution computations have captured many of the major features of loading of the rotor blades. However, certain features of the high frequency loading characteristic of close wake/rotor interaction have been missed in many of these cases. The application of reconstruction provides the opportunity to capture these events.

The computations carried out typically used 32 to 48 time steps per revolution to set up the low resolution solution. For N time steps, a smoothing core of $(2\pi/N)R$ was used on all wake filaments to set up the low-resolution velocity field, the point of departure for the reconstruction calculations. The ANM procedures described in Section 2 were then invoked to recapture the flow field due to the smaller 'actual' vortex cores using temporal interpolation factors ranging from 8:1 to 20:1. This represents levels of azimuthal resolution ranging from 0.94 deg. to 0.375 deg. The former is essentially the minimum level of temporal resolution appropriate for BVI studies, while the latter is a
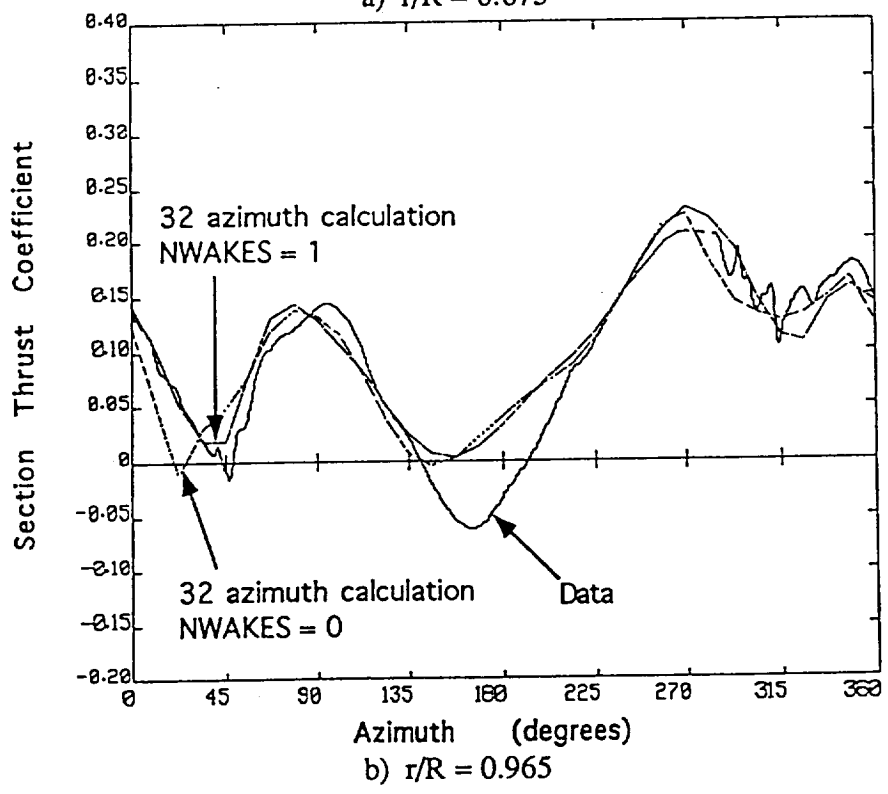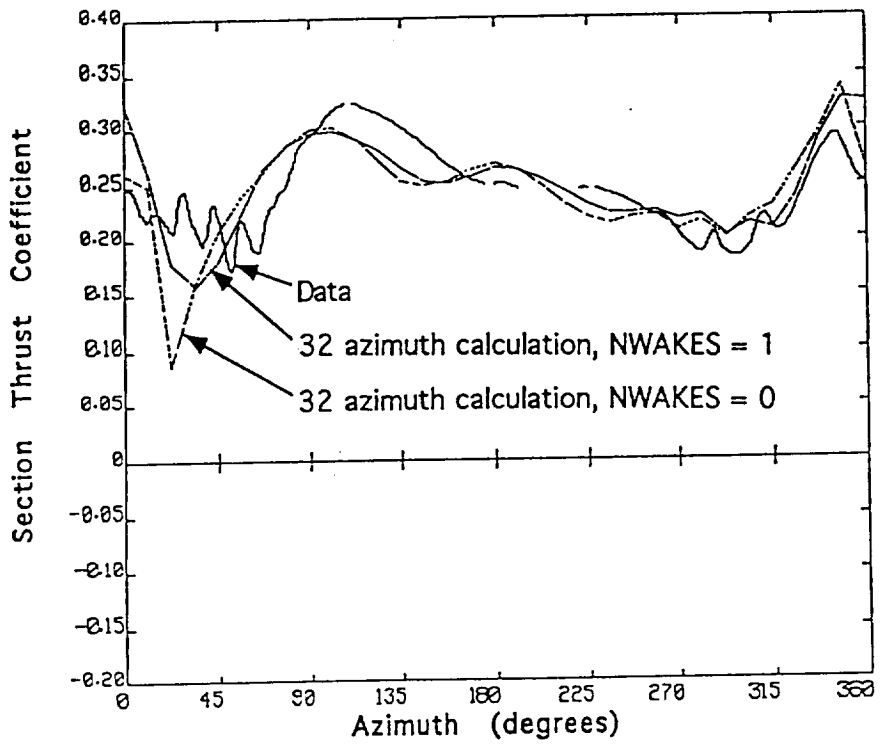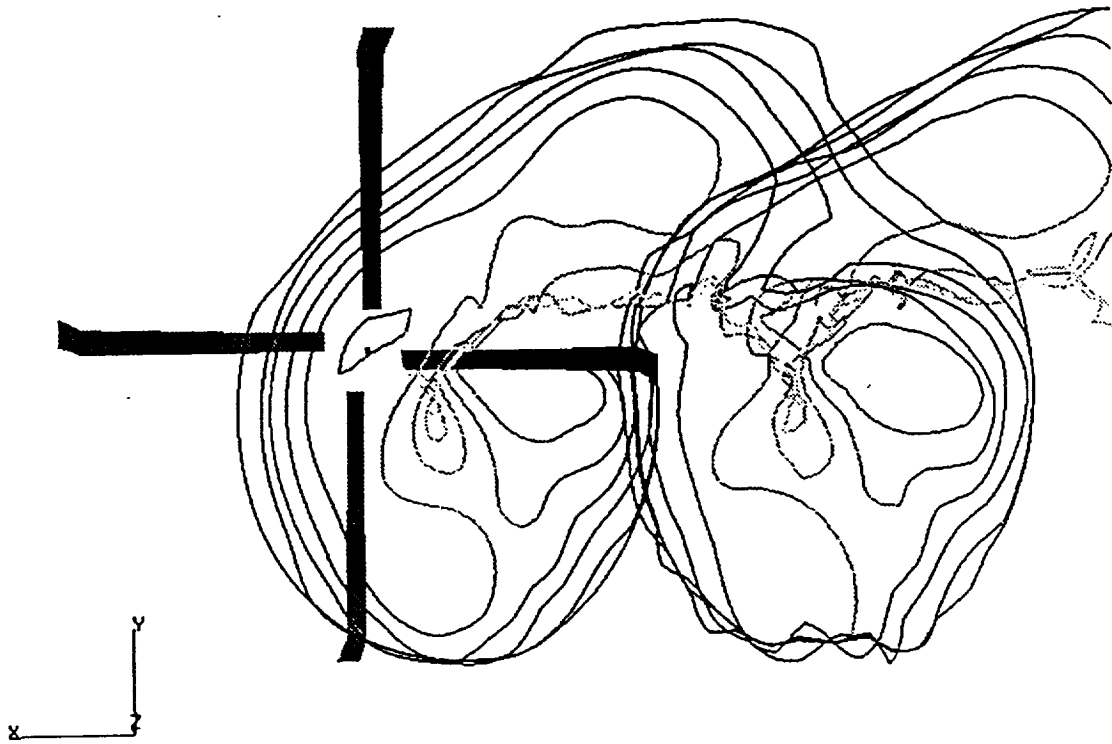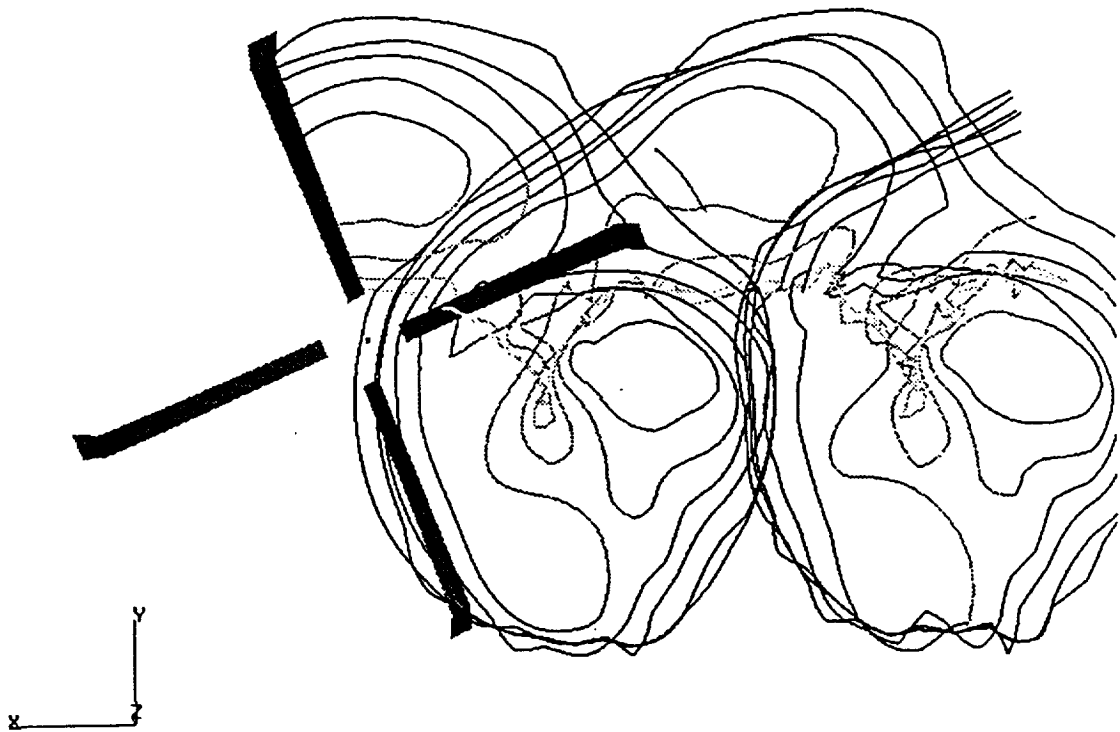
Figure 7-8. Sikorsky UH-60A model rotor dC_T/dx for Test Point 1126: comparison of measured data. and predictions with and without full wake-on-wake influence.
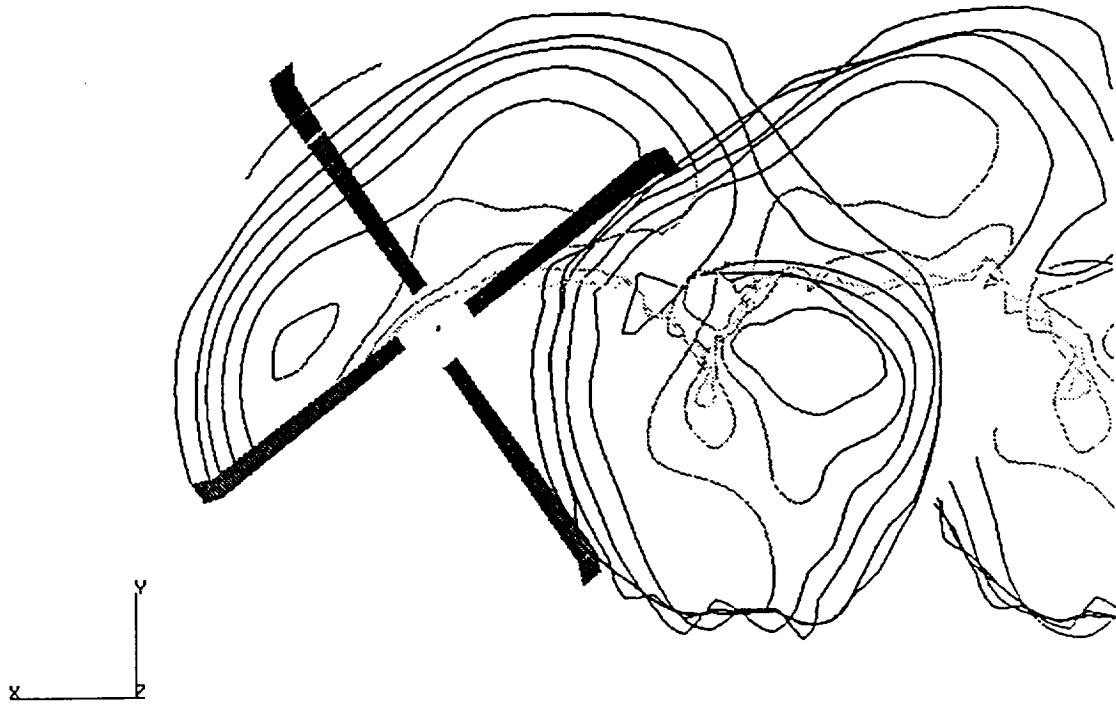
a) Reference blade at $\Psi = 0°$

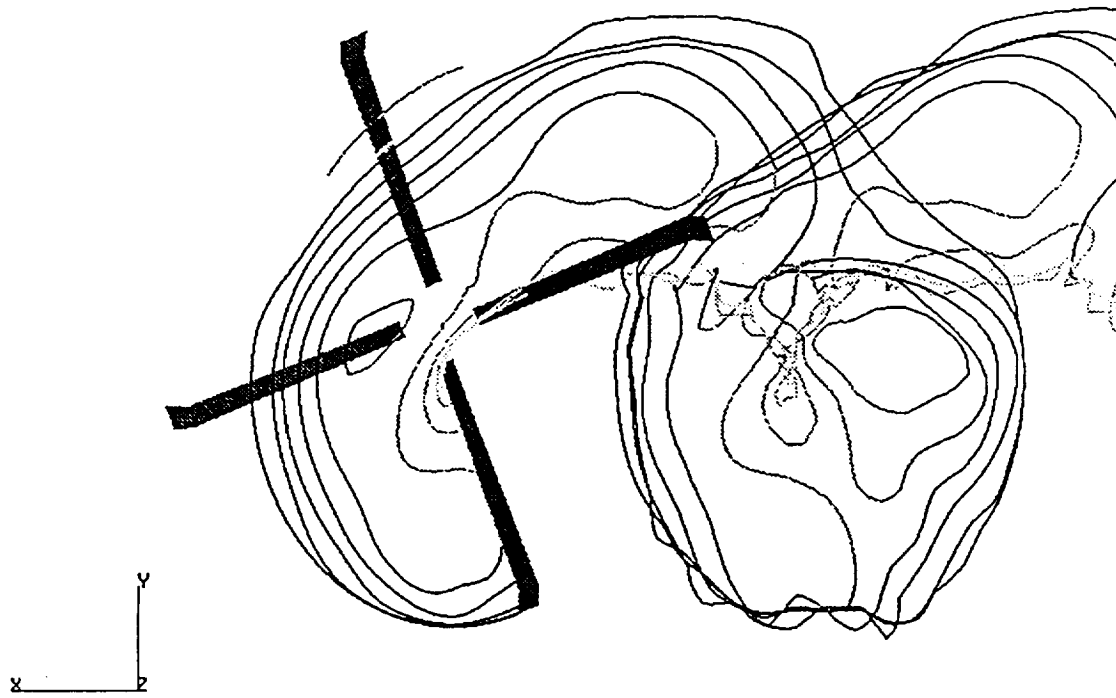
b) Reference blade at $\Psi = 105°$

Figure 7-9.   Top view of CVC wake for the UH-60A rotor, Test Point 1137.

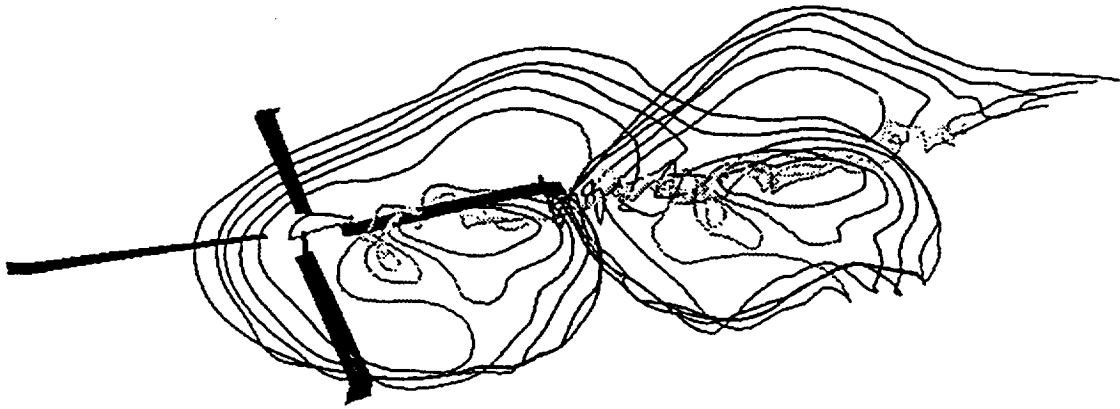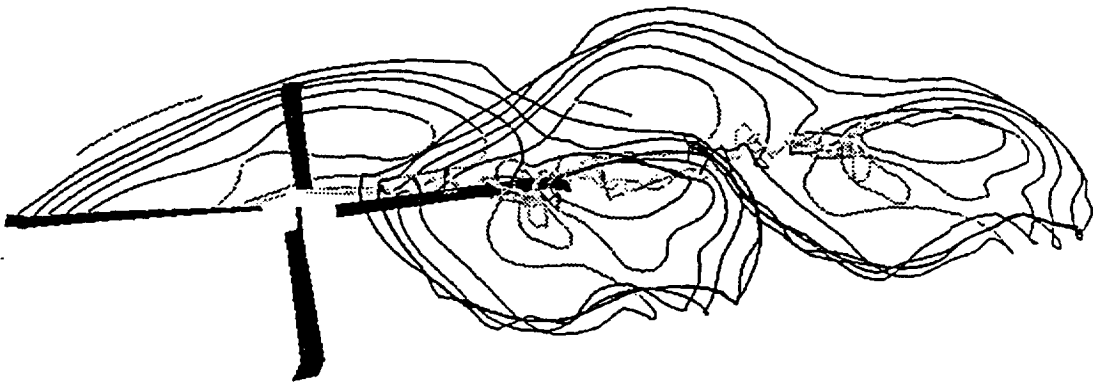c) Reference blade at $\Psi = 217.5°$

d) Reference blade at $\Psi = 292.5°$

Figure 7-9 (Cont'd). Top view of CVC wake for the UH-60A rotor, Test Point 1137.

a) Reference blade at $\Psi = 0°$

b) Reference blade at $\Psi = 180°$

Figure 7-10.   Oblique view of CVC wake for the UH-60A rotor, Test Point 1137.

conservative choice for good resolution of the pressure transients that lead to BVI noise in the far field.

It is difficult to confirm the CPU reduction associated with this level of temporal interpolation, because of the extreme difficulty of running a direct calculation to completion, even with 1.0 deg. time steps. However, the CPU savings estimated for 8:1 reconstruction is conservatively estimated at a factor of 100, and probably closer to 500, while for 20:1 the CPU savings is probably an order of magnitude higher still.

7.3.1 Boeing 360 Model Rotor

As noted above, Test Point 66 for the Boeing 360 model rotor contains a substantial BVI signature, both in the first and fourth quadrants. The present discussion will focus primarily on the fourth quadrant events, since these are due primarily to interactions of the blade with tip vortices. The treatment of advancing side blade interactions and encounters with the root vortex system will be addressed later.

Figures 7-11 and 7-12 show the results of the application of 8:1 reconstruction to this flight condition for a baseline run with 32 steps per blade revolution. Figure 7-11a shows the comparison of the complete time history of normal force coefficient at the $r/R = 0.8$ station. The presence of large "background" loading levels tends to mask the details of the high frequency loading component that is to be resolved by reconstruction; in order to make this clearer, the same time histories were filtered by removing the first ten harmonics of rotor frequency. This filtered signal allows a much improved view of the high frequency components characteristic of blade/wake encounters. Figure 7-11b shows the comparison of this portion of the signal, and it is evident that the agreement is excellent in both magnitude and phase in the fourth quadrant. Repeating the same exercise for the station $r/R = 0.95$ (Fig. 7-12) indicates that the phasing of the loading is still very well captured, though here the magnitude of the loading is underpredicted by 30-40%.

Despite some quantitative errors, these results are judged to be very encouraging, in that the high frequency events are occurring at very nearly the correct amplitude and phase while no attempt has been made to "fine tune" the computation. The precise magnitude of the loading is, of course, somewhat sensitive to details of the vortex core modeling, i.e., the issues discussed in Section 4. The reconstruction procedure here was set to use the baseline variable-core Scully model (described in Section 4.1) as the inner solution. The next section discusses the application of the more advanced integral rollup model to this problem, as well as issues relevant to improved resolution of first quadrant loading.

7.3.2 UH-60 Airload Reconstruction

Correlation calculations similar to those carried out for the Boeing 360 were executed for the UH-60A rotor, exploiting the reconstruction capabilities of RotorCRAFT/AA. The same three flight conditions used in Section 7.2 will be discussed, though here the emphasis will be on computing the aerodynamic loading with high temporal resolution. Each of the three flight conditions modeled features some events that require very small time steps for effective resolution, though this by itself does not guarantee good correlation, as will be seen. A combination of good temporal resolution of blade/wake interaction events and accurate spatial resolution of the vortex core structure was required.
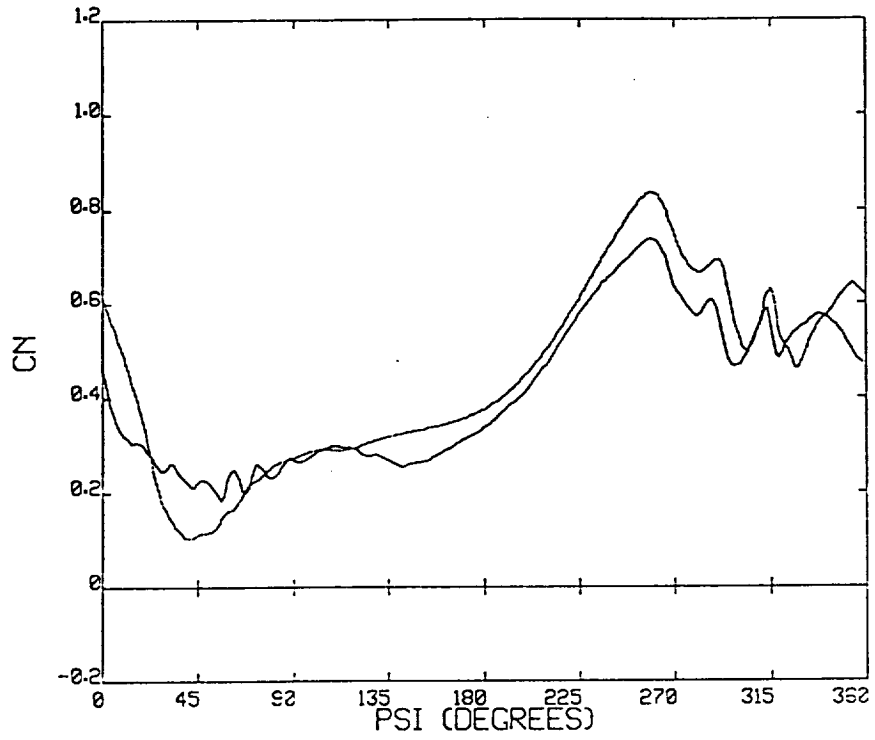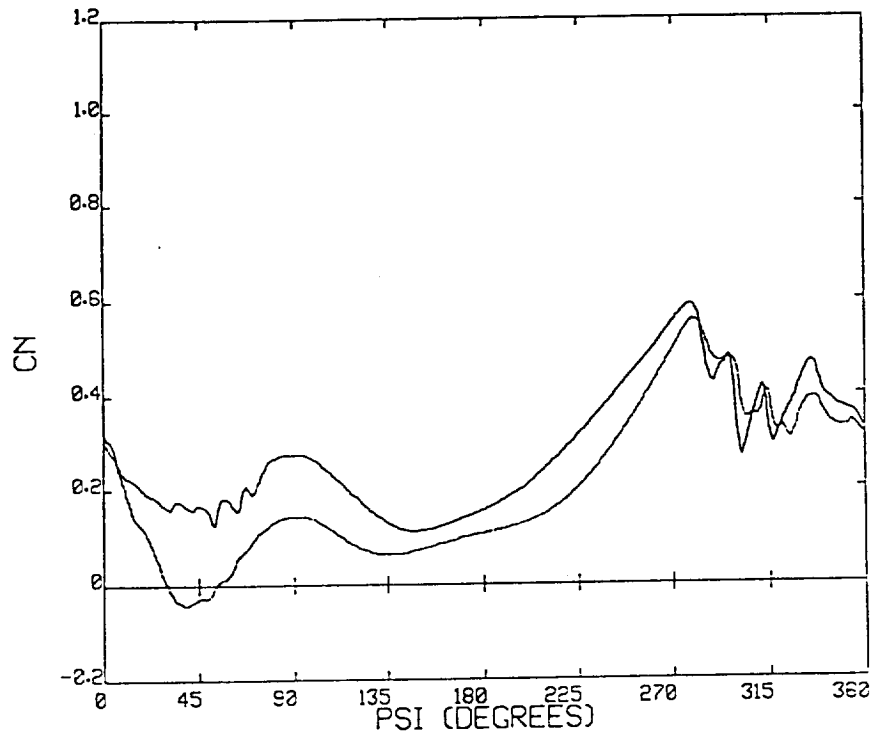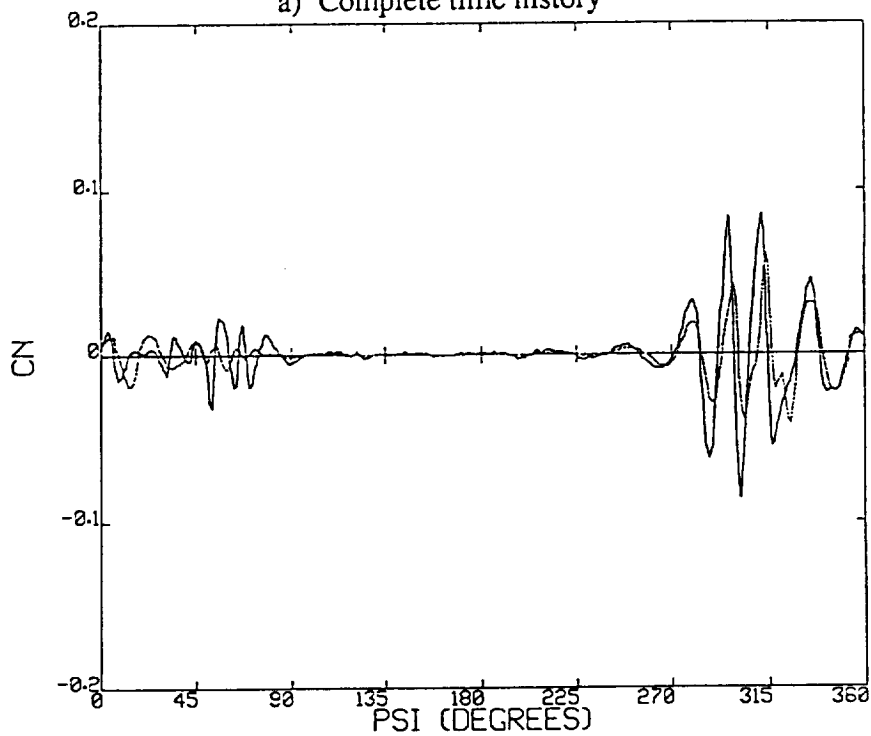
a) Complete time history
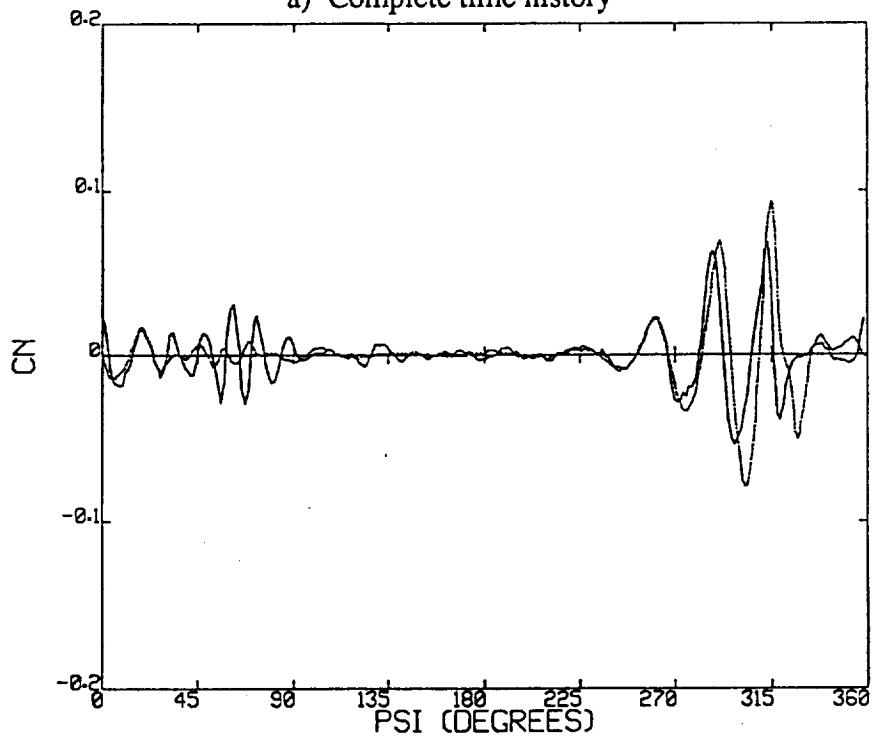
b) Harmonics 0-10 removed

Figure 7-11. Measured and reconstructed normal force coefficient for the Boeing 360 rotor at r/R = 0.80 : Test Point 66.

a) Complete time history

b) Harmonics 0-10 removed

Figure 7-12. Measured and reconstructed normal force coefficient for the Boeing 360
rotor at r/R = 0.95 : Test Point 66.

The UH-60A Test Point 1126 (advance ratio = 0.2) will be used as an example case for discussing the roles of refined temporal and spatial resolution in predicting higher harmonic airloads and noise. The baseline "low resolution" solution is the calculation discussed previously with 10 complete blade revolutions, 48 time steps per revolution and 2.5 turns of free wake with a maximum of 14 vortex filaments spanwise at any azimuth. This calculation was reconstructed with a multiplier of 20:1 to obtain a "high resolution" solution with 960 time steps per blade revolution. This high multiplier was chosen because a minimum of roughly 720 time steps per revolution (i.e., 0.5 degree steps) are necessary in order to accurately predict noise generation. The low resolution calculation took roughly 14 hours to complete on C.D.I.'s Iris workstation with the subsequent reconstruction requiring an additional 2 hours. A direct calculation of 960 time steps without the use of reconstruction would optimistically require roughly 20,000 hours (2 years) of CPU to complete and is therefore not included here for comparison.

Figures 7-13 and 7-14 compare airload predictions obtained with the low resolution and high resolution calculations at two spanwise locations near the tip. A slight improvement can be seen in the correlation with the high frequency ripples in the fourth quadrant. However, even with the extremely fine temporal resolution there is still room for further improvement. Similar statements can also be made concerning the other UH-60A Test Points 1137 (advance ratio = 0.2) and 1311 (advance ratio = 0.3), especially with regard to high frequency events in the first quadrant that are not recovered by simply increasing the time resolution. It was discovered that extremely fine spatial resolution is also necessary in order to precisely model these high frequency events, i.e., it appears necessary to recover the exact location and strength of the rolled-up tip vortex and to use the refined core model for the internal structure of the tip vorticity to properly model the higher harmonic airloads. This level of refinement was expected to be necessary in order to accurately predict noise generation, however, it is apparently also required to recover the high frequency airload events present in the UH-60A data. Other possible causes are being investigated, though evidence to date supports this conclusion as will be discussed in the following section.

7.3.3 Application of Refined Core Models

In order to examine the anticipated need for a refined tip vortex core model, consider that the calculations discussed above contained a maximum of 14 filaments spanwise at any azimuth. Even when tightly packed, these filaments still have a core radius of roughly 5%R near the blade tip based on the code's default core model. As noted above, correlations with data using this default core model have been excellent for numerous studies. However, the present effort is attempting to model very high frequency events previously unstudied. A 5%R core radius near the blade tip would correspond to an azimuth step of roughly $360*0.05/(2\pi) = 3$ degrees, far greater than the 0.5 degree accuracy required for predicting noise generation, though not unreasonable for expecting to capture the high frequency airload events. While increasing the number of filaments trailed from the rotor blade may improve results somewhat, this could still fail to accurately model the structure of the rolled-up tip vorticity. In principle, the CVC model could directly compute the vortex filament rollup through the use of an arbitrarily large number of filaments and very small time steps. This is obviously impractical if reasonable computational efficiency is to be retained. The most appropriate approach within the context of the reconstruction method is to apply a refined core model like that outlined in Section 4.

The core model described in Section 4 was thus implemented in conjunction with reconstruction in order to improve the prediction of high frequency airloads and far field
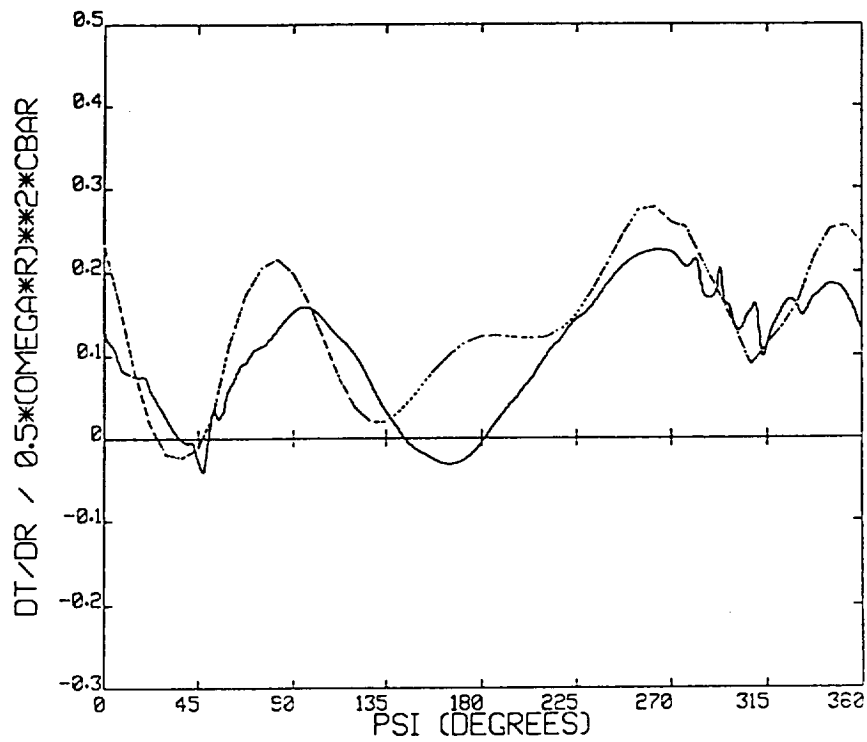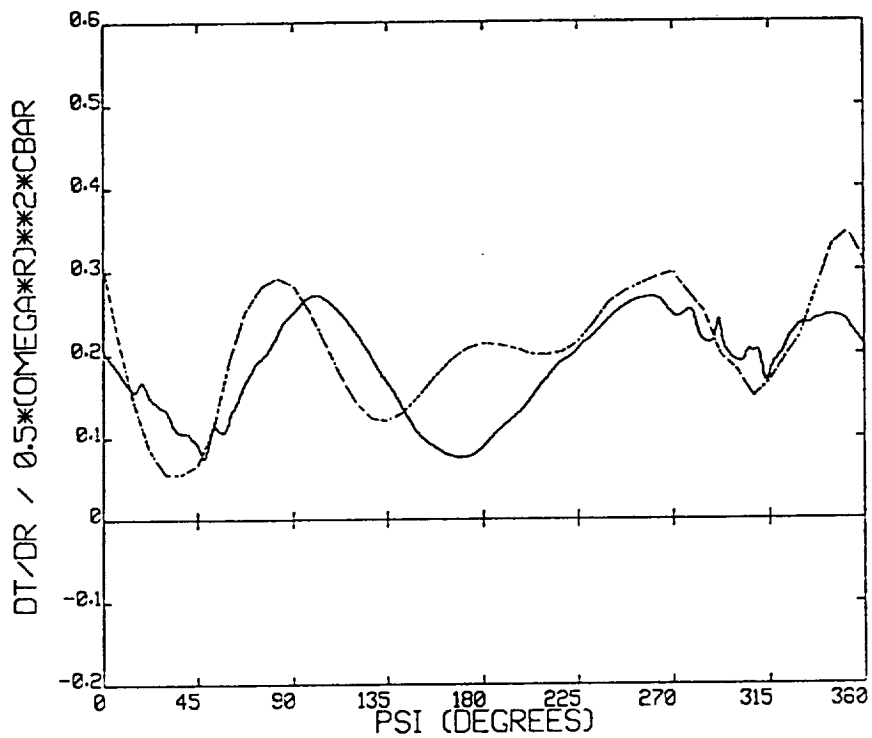
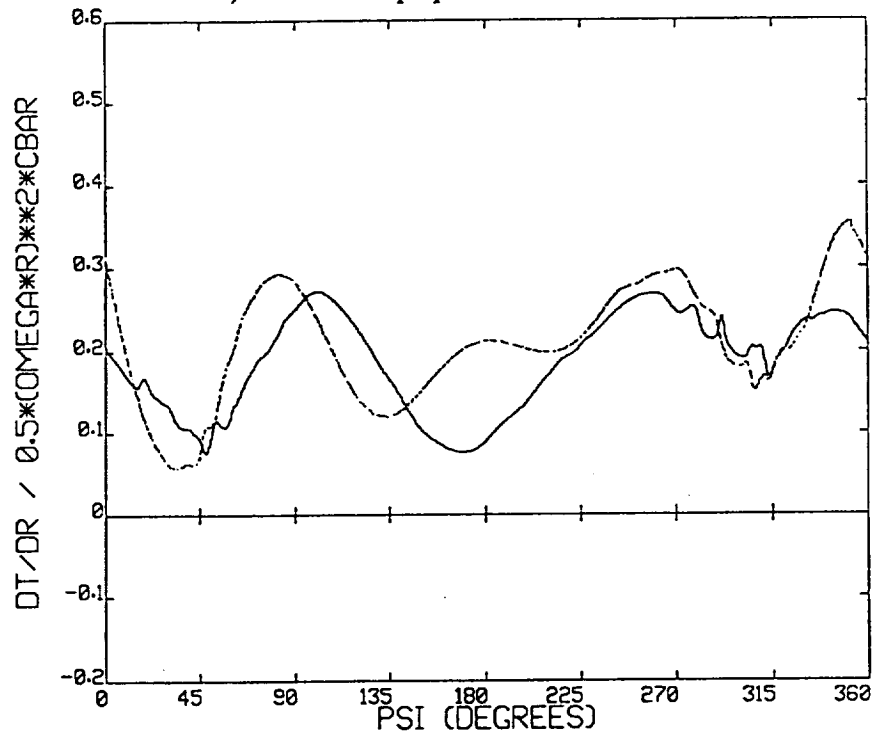a) 48 time steps per blade revolution
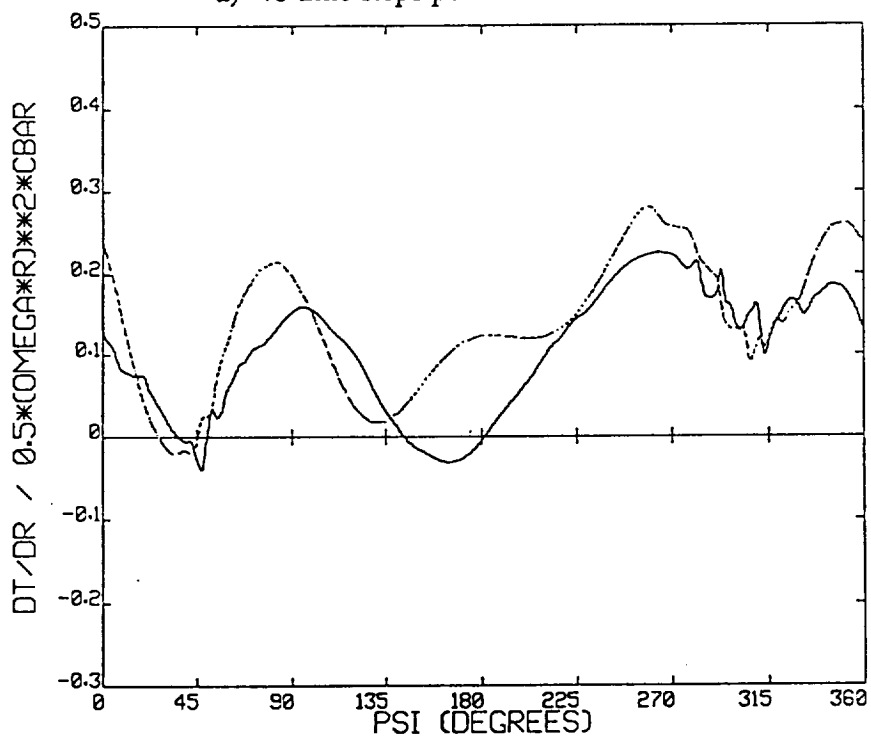
b) 960 time steps per blade revolution

Figure 7-13. Sikorsky UH-60A, dC_T/dx for Test Point 1126 at r/R = .920 ; 48 time steps versus 960 time steps per blade revolution (solid = measured, dotted = predicted).
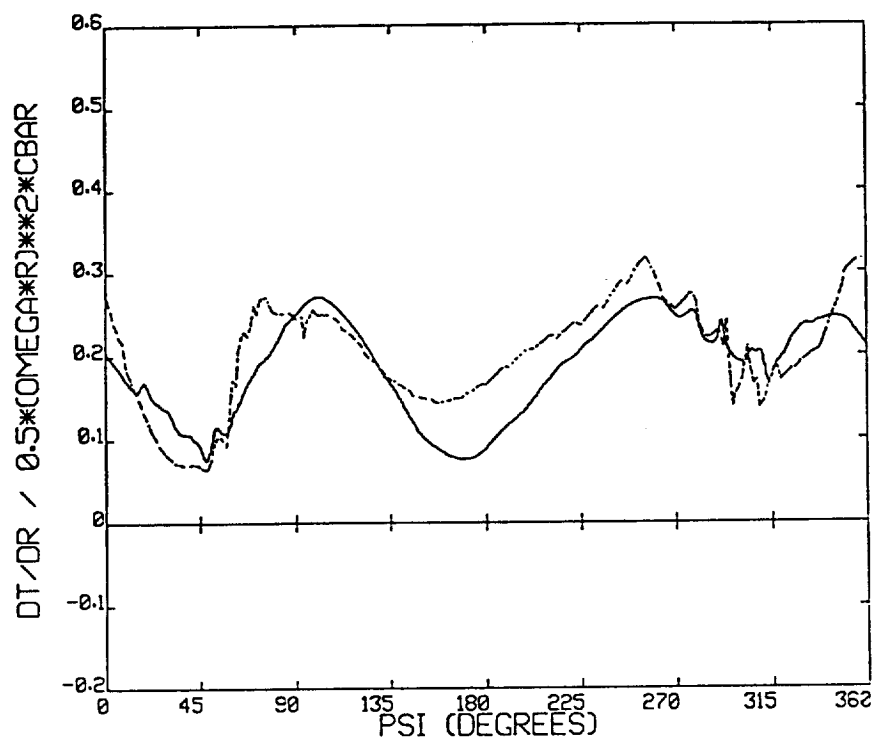
a) 48 time steps per blade revolution

b) 960 time steps per blade revolution

Figure 7-14. Sikorsky UH-60A, dC_T/dx for Test Point 1126 at $r/R = .865$; 48 time steps versus 960 time steps per blade revolution (solid = measured, dotted = predicted).

C-2

noise. This core model affords a more physically accurate representation of the internal structure of the rolled-up vortex than simple smoothing core depicted in Eq. 4-1; a more refined model is necessary when investigating these small time and spatial scales. Of equal importance is the accurate determination of the location and strength of the rolled-up tip vortex structure. This is obtained by using the centroid and strength of the tip vortex elements in the low resolution calculation that are identified as those that roll up into the tip vortex structure.

Figure 7-15 shows airload results for UH-60A Test Point 1126 for a 256 time step per blade revolution calculation performed with the refined core model. The same spanwise locations are shown as in Figures 7-13 and 7-14 to facilitate comparison. The refined core model result was obtained with 8:1 reconstruction of a 32 time step per revolution calculation. Unlike previous calculations, the high frequency event in the first quadrant of the airload is now present in the prediction. Also the prediction of the fourth quadrant higher harmonic airload appears to be improved, though slightly over predicted in the r/R=.865 case. Figure 7-16 compares just the higher harmonic airloads (harmonics above 10) between the low resolution, 48 time step calculation and the reconstructed, 256 time step, calculation with the refined core model. Clearly high frequency events absent in the low resolution calculation are being recovered with the reconstructed case with the refined core model. The correlation in both magnitude and phase clearly need to be improved, but are nonetheless encouraging. These results suggest that indeed both reconstruction and the refined core model are necessary to accurately model these high frequency airload events.

7.4 Rotor Noise Correlations

As noted previously, the ultimate application of the software developed here is the prediction of far-field noise. To this end, the RotorCRAFT/AA code contains a direct interface with NASA's WOPWOP code. Upon completion of a RotorCRAFT/AA calculation, the user has the option to continue directly into a WOPWOP calculation. The input parameters required by WOPWOP are automatically channeled from RotorCRAFT/AA and stored in the appropriate arrays and input subroutines. These parameters include blade geometry information, blade motion information, run configuration information, airfoil section profile information and the blade surface differential pressure distribution as a function of chord, span and azimuth location. The chordwise surface pressure distribution can be evaluated with the refined lattice solution described in Section 6 or with a flat plate distribution. Absolute pressures on the upper and lower blade surface are currently not available though could be determined using 2-D look-up tables to evaluate the viscous contribution to surface pressure if desired. The version of WOPWOP currently linked to the RotorCRAFT code is essentially that described in Reference 15 with a few minor modifications that allow calculations for secondary rotors (e.g., tail rotors) which rotate at different rates than the main rotor. (For such cases, the surface pressure distribution is aperiodic.) The interface allows users familiar with RotorCRAFT/AA but not WOPWOP to obtain acoustics predictions with little effort.

The following two sections contain sample noise prediction calculations using the interface between RotorCRAFT/AA and WOPWOP to demonstrate the progress achieved to date. Calculations are presented for the same three UH-60A flight conditions discussed previously: Test Points 1126 (advance ratio 0.15), 1137 (advance ratio 0.20) and 1311 (advance ratio 0.3). Extensive acoustic pressure data was recorded as part of the DNW rotor tests (Refs. 57-59). Acoustic pressure signals were recorded at microphone locations shown schematically in Figure 7-17. In order to provide a representative sample of the results obtained, computed acoustic pressure will be shown
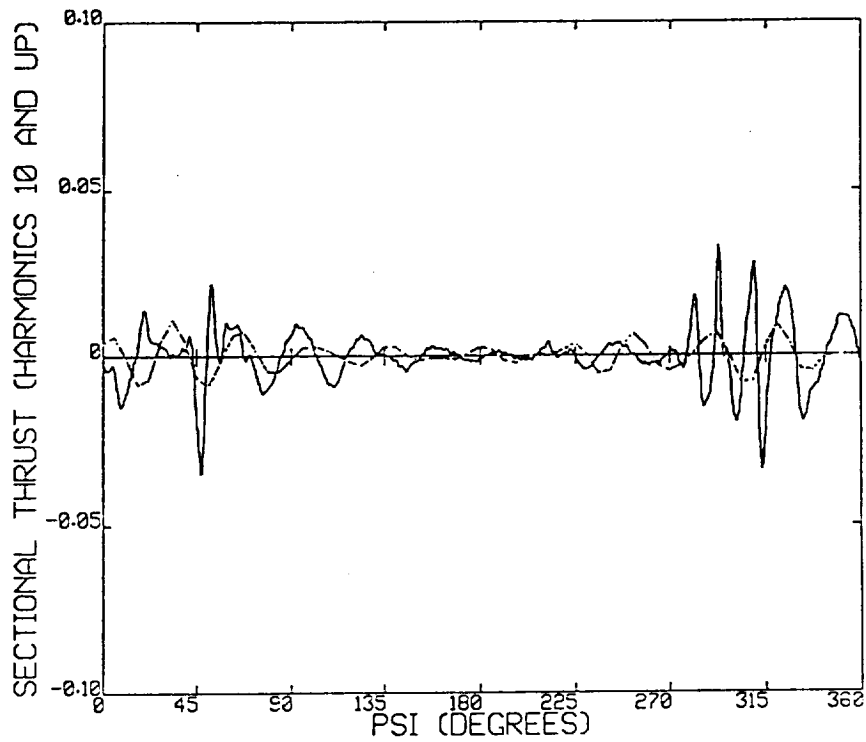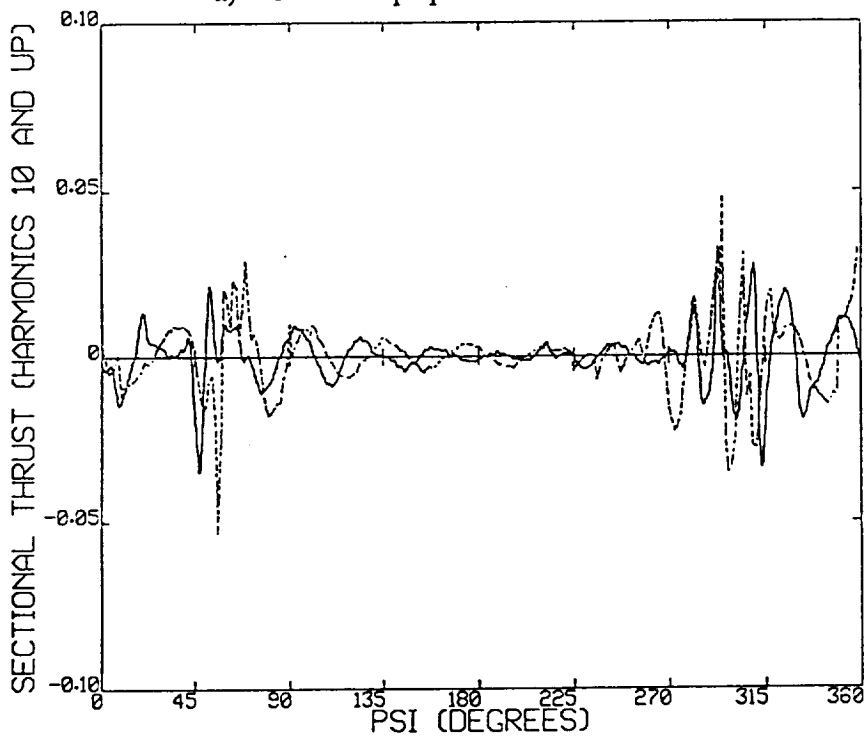
a) r/R = .865
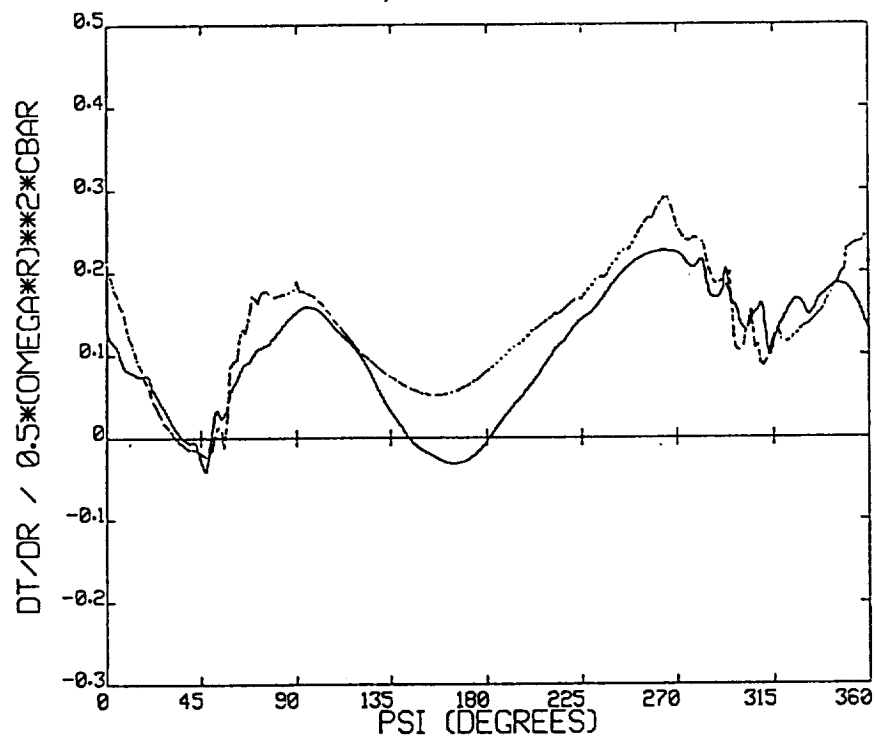
b) r/R = .920

Figure 7-15. Sikorsky UH-60A, dC_T/dx for Test Point 1126 with 256 time steps per blade revolution; refined vortex core model (solid = measured, dotted = predicted).

92

a) 48 time steps per blade revolution

b) 256 time steps and refined core model

Figure 7-16. Sikorsky UH-60A, dC_T/dx with harmonics 0-10 removed for Test Point 1126 at r/R = .920 ; 48 time steps and basic core model versus 256 time steps and refined core model (solid = measured,   dotted = predicted).

a) Top view

b) Side view

c) Front view
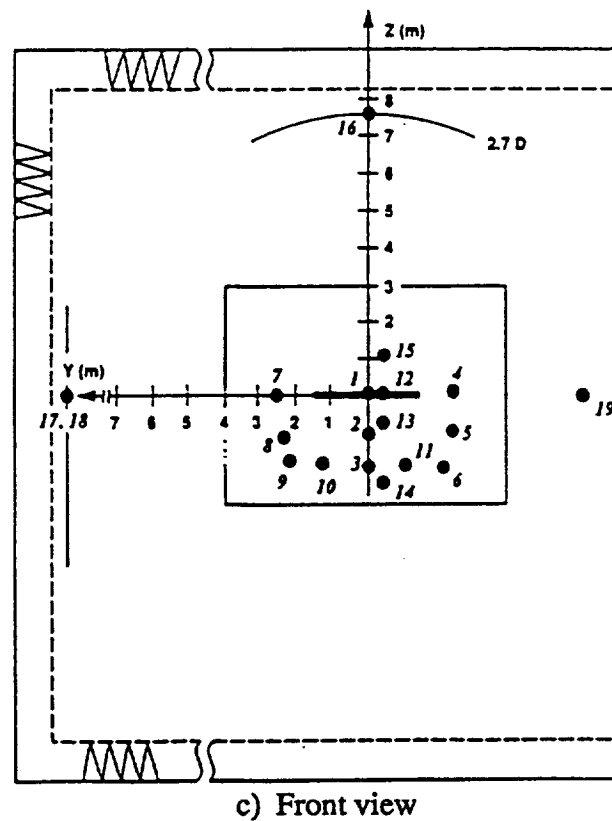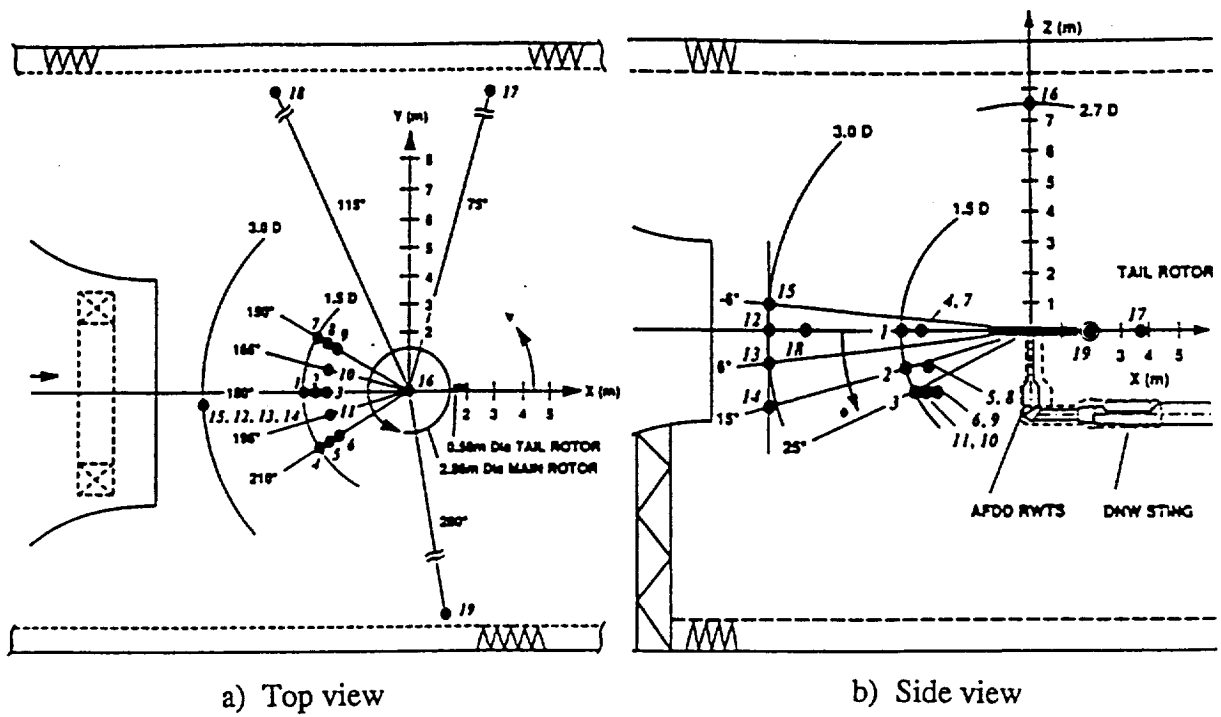
Figure 7-17.   Microphone locations for the DNW UH-60 rotor acoustics test.

for four locations: microphones 3, 6, 7 and 9 as shown in Figure 7-17. Since the microphones do not measure mean pressures, the mean pressure has been removed from the predictions in order to facilitate a proper comparison.

7.4.1 Low Resolution Noise Computations

The first demonstration calculations presented are WOPWOP calculations using the results obtained from the low resolution, 48 time step calculations discussed in Section 7.3. For these acoustics results, little difference was observed when using the flat plate surface pressure distribution instead of the refined lattice distribution (see Section 6). Therefore, the flat plate distribution was used which greatly reduced CPU time. Surface pressure information and blade motion information were channeled directly from RotorCRAFT/AA into WOPWOP and also stored in external files so that WOPWOP could subsequently be re-initiated for calculations at different microphone locations without repeating the entire RotorCRAFT/AA calculation. Default values from Reference 15 were used in most cases for WOPWOP input parameters. It was observed that 256 calculation points per blade passage were adequate for the high resolution acoustics calculation and 100 calculation points were adequate for the low resolution calculation. It was also verified that results were not sensitive to increasing the chordwise and spanwise surface pressure resolution beyond the default values.

Figure 7-18 shows the predictions for the low advance ratio case, Test Point 1126. The results at all four microphones exhibit the same qualitative accuracy; the predicted disturbance is similar in magnitude and very nearly in phase with the measured pulses, though lacking the fine structure in the data. This is particularly notable in Figure 7-18d, microphone 9, where the spiky signature in the data, indicating BVI noise, is noticeably absent in the prediction. Figure 7-19 (Test Point 1137, advance ratio 0.2) shows broadly similar results, though the under prediction of the down-pulse seen at the in-plane microphone 7 is more pronounced. The final comparison shown in Figure 7-20 confirms this pattern for Test Point 1311 (advance ratio 0.3). Though the high frequency BVI loading is imperfectly captured, the overall size and shape of the pressure pulse nonetheless emerges clearly in all three cases.

7.4.2 High Resolution Computations of Airloads and Noise

The correct resolution of BVI airloads and noise is a topic of prime importance and was the focus of considerable computational experimentation during this effort. As discussed previously with regard to airload reconstruction calculations, both high temporal and high spatial resolution appear to be necessary to accurately predict high frequency loading events and far-field noise. Therefore, the refined integral core model as described in Section 4 was incorporated in the reconstruction approach to study its effect on noise prediction. A discussion of airload predictions is first presented to identify the BVI events responsible for the noise generation and the ability of the analysis to model them.

Figure 7-21 shows the airload time histories at two radial stations for the UH-60A at Test Point 1126; here, the basic reconstruction scheme with the Scully core inner solution (Eq. 4-1) is used, with the core sizes selected using the default scheme described in Section 4.1. The calculation used 20 filaments trailing from each blade at 32 azimuth locations reconstructed with a multiplier of 30:1 to obtain 0.375 degree azimuth increments in the final result. It is evident that the loading signature on the retreating side is captured moderately well while the small but important BVI loading peaks on the advancing side are missing. Using visualizations of the computed wake configurations (e.g., counterparts to Fig. 7-9 for Test Point 1126), it was observed that the tip filaments
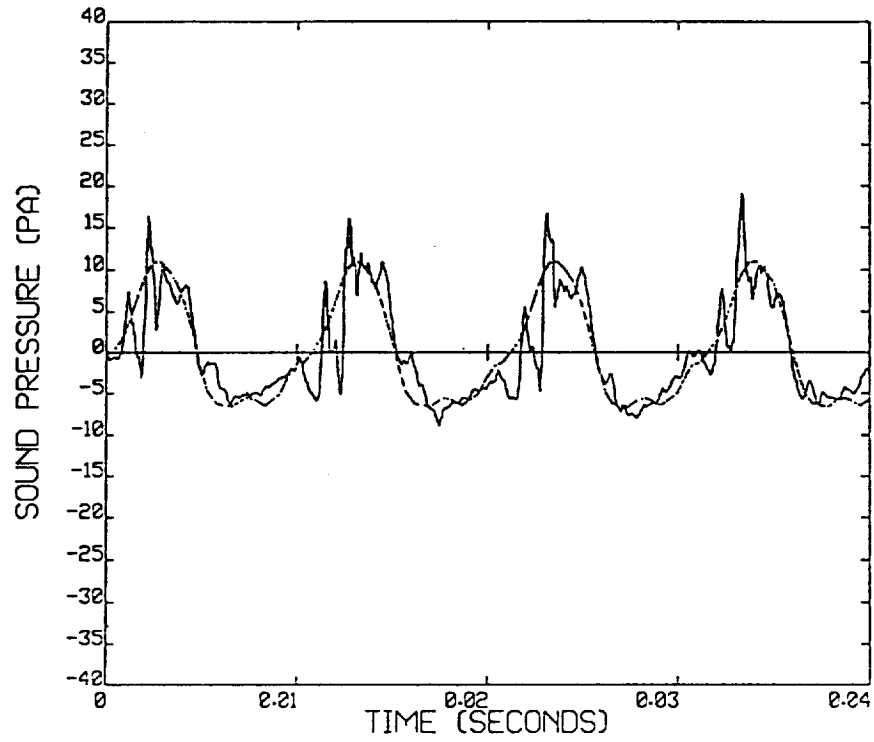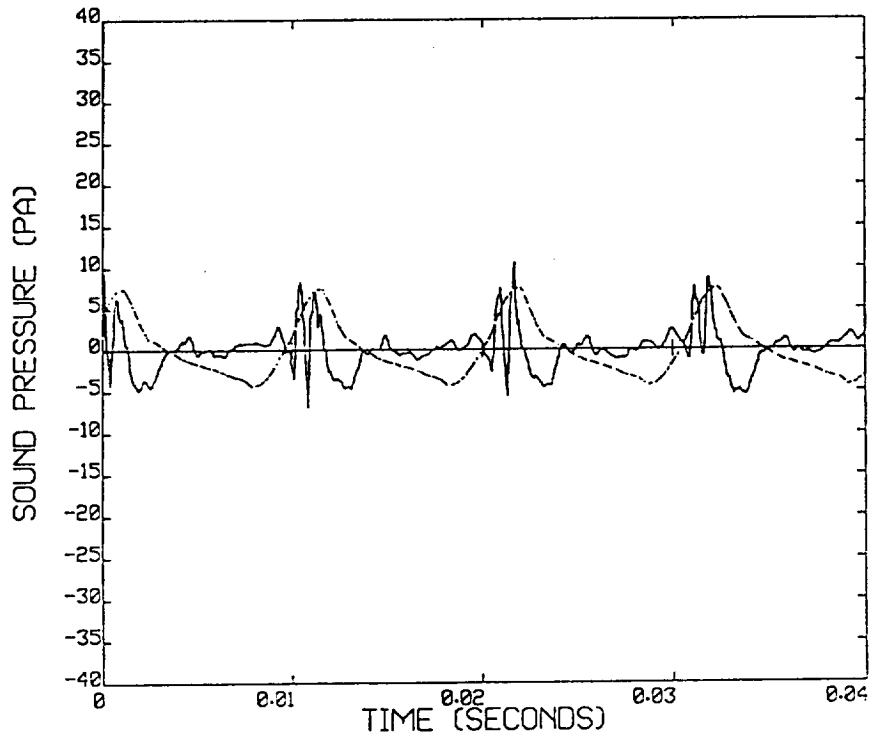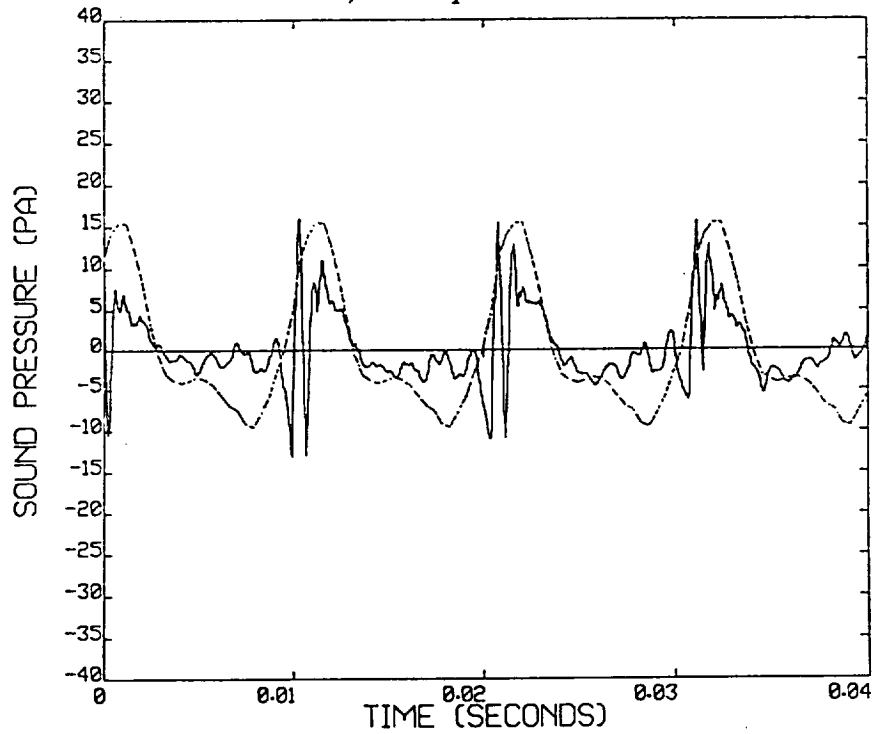
a) Microphone 3
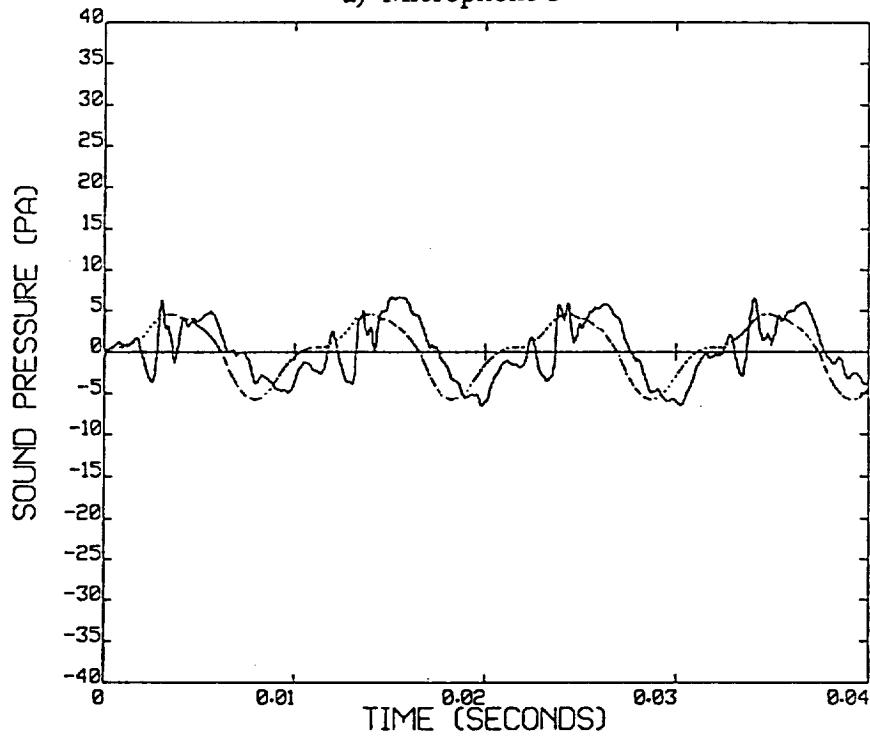
b) Microphone 6

Figure 7-18. RotorCRAFT/AA computations of rotor noise for the UH-60A model rotor: Test Point 1126 (solid = measured, dotted = predicted).
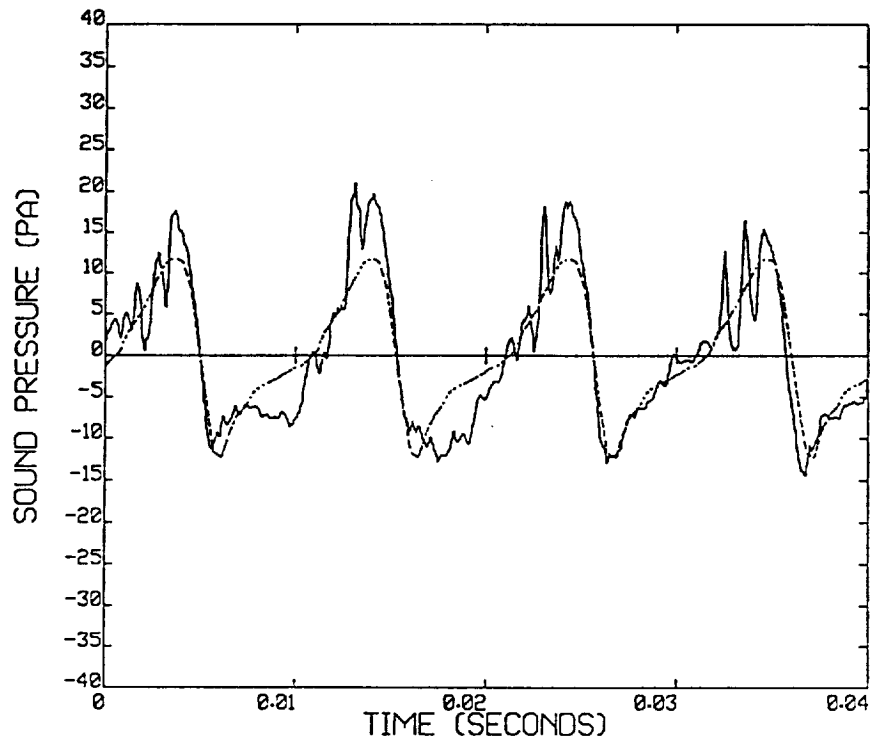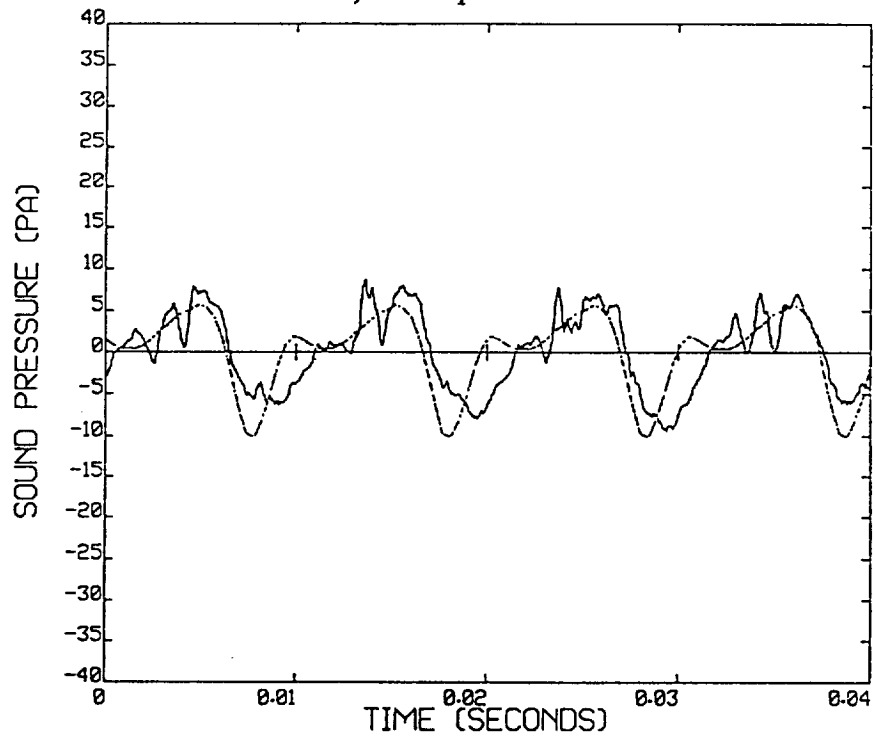
96

c) Microphone 7

d) Microphone 9

Figure 7-18 (Cont'd). RotorCRAFT/AA computations of rotor noise for the UH-60A model rotor: Test Point 1126 (solid = measured, dotted = predicted).
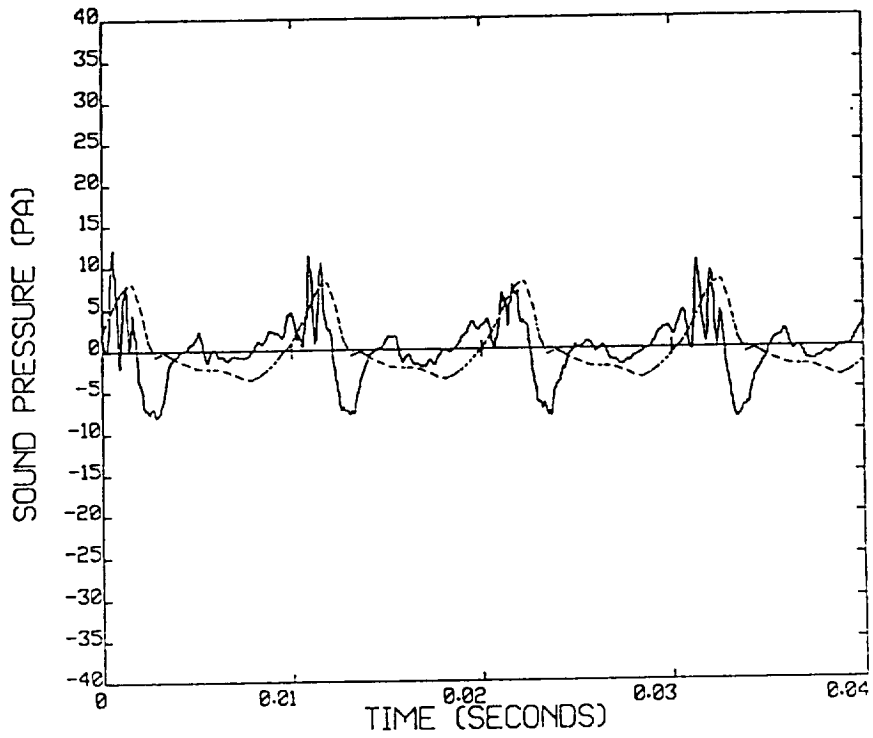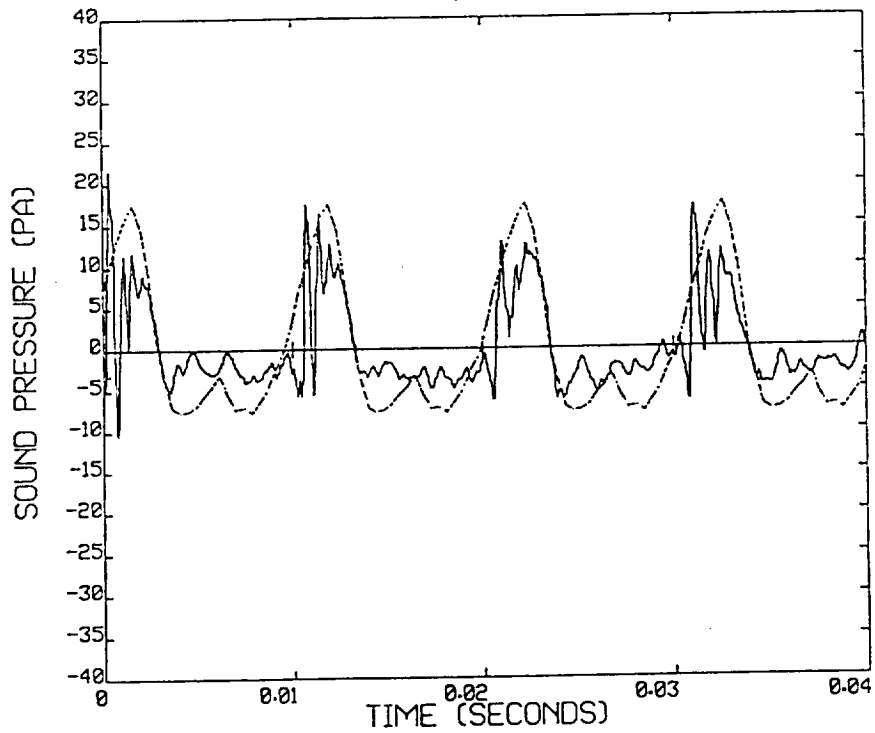
a) Microphone 3

b) Microphone 6

Figure 7-19. RotorCRAFT/AA computations of rotor noise for the UH-60A model rotor: Test Point 1137 (solid = measured, dotted = predicted).
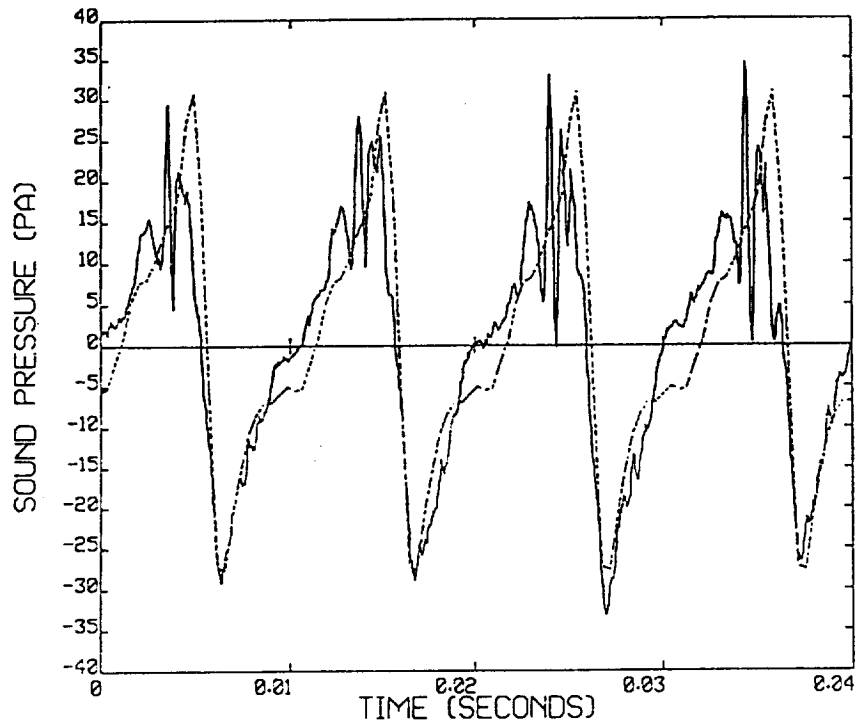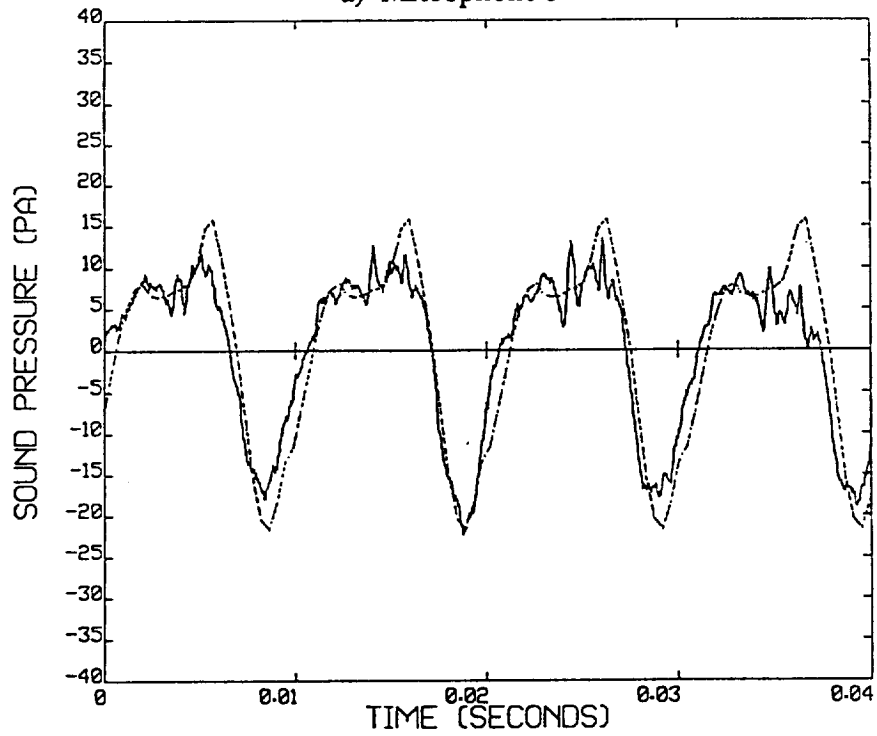
c) Microphone 7

d) Microphone 9

Figure 7-19 (Cont'd). RotorCRAFT/AA computations of rotor noise for the UH-60A model rotor: Test Point 1137 (solid = measured, dotted = predicted).
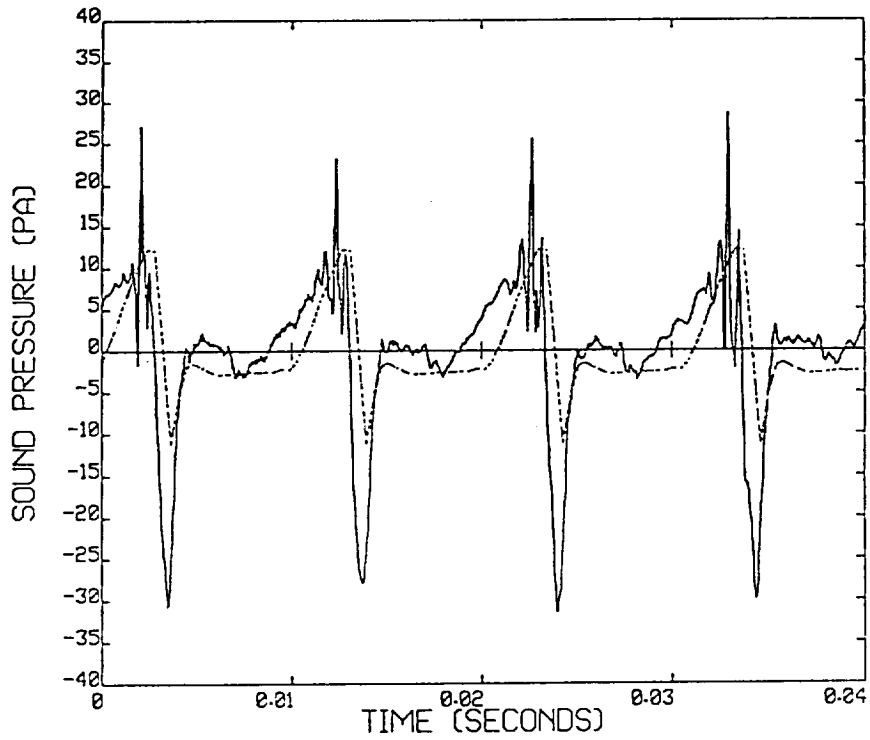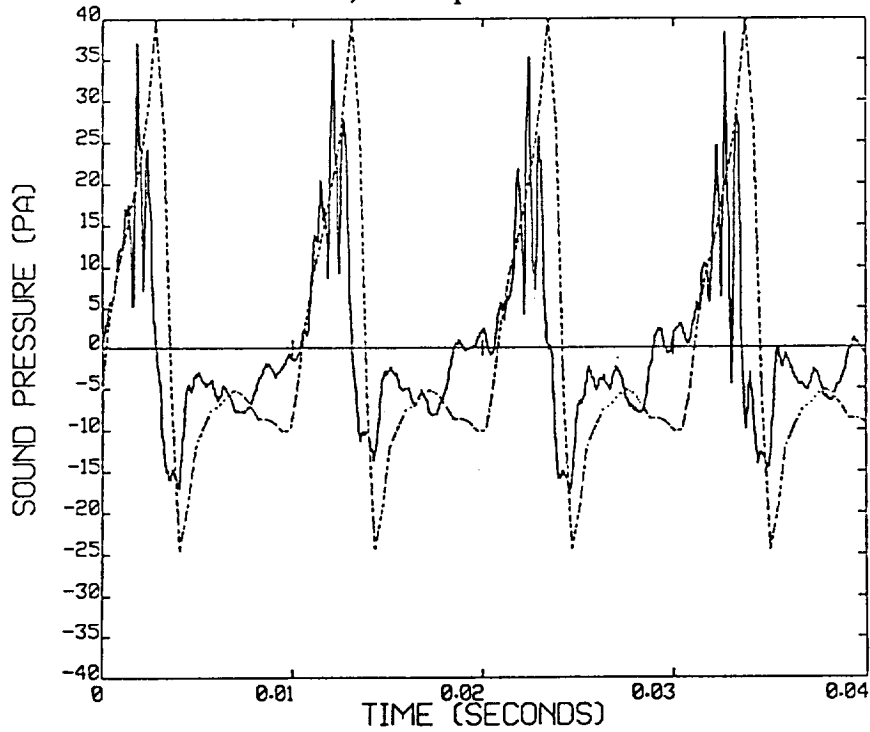
99

a) Microphone 3

b) Microphone 6

Figure 7-20. RotorCRAFT/AA computations of rotor noise for the UH-60A model
rotor: Test Point 1311 (solid = measured, dotted = predicted).

c) Microphone 7

d) Microphone 9

Figure 7-20 (Cont'd). RotorCRAFT/AA computations of rotor noise for the UH-60A model rotor: Test Point - 1311 (solid = measured, dotted = predicted).
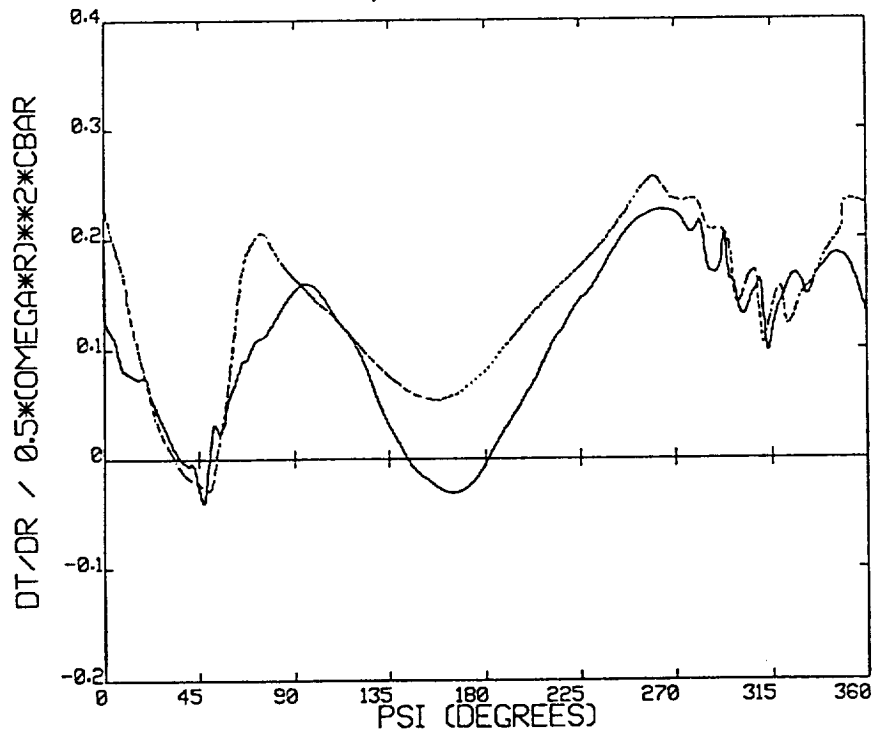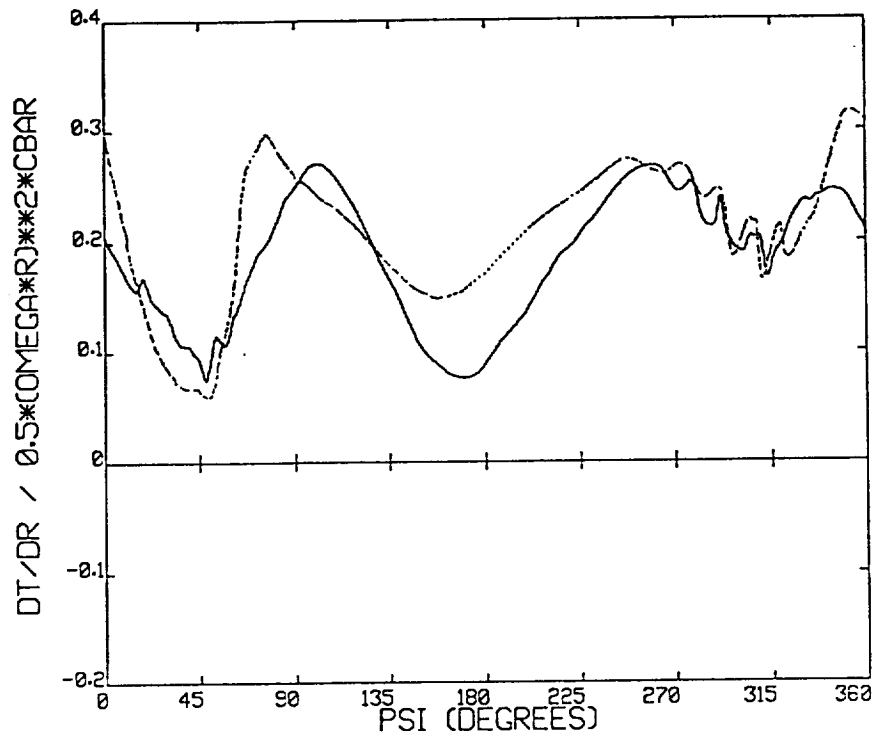
101

a) r/R = .865

b) r/R = .920

Figure 7-21. Sikorsky UH-60A dC_T/dx for Test Point 1126; 20 filaments and 32 time steps reconstructed to 960 time steps; baseline Scully core model (solid = measured, dotted = predicted).

were the likely source of the loading event around azimuth angle 45 deg., and that the CVC trailers that composed the vortex bundle interacting with the blade at this point exhibited a strong tendency to roll up, though the rollup appears incomplete at the time of interaction. It was also evident that the events on the retreating side (which are also due to tip vortex interactions) are caused by relatively "young" tip vortices (90-180 deg. of wake age) while those on the advancing side are caused by "older" tip vortices (360-540 deg. of wake age) generated from previous rotor rotations.

Applying the refined vortex core model in addition to reconstruction gave the results shown in Figure 7-22. The correlation on the retreating side of the rotor improves slightly, but the event on the advancing side is still not predicted well. This calculation was run with a relatively low value of a "vortex age parameter" which governs the age of vortices that are considered to be candidates for amalgamation (or "bundling") with the refined core model, as well as determining the strength and position of the bundled replacement vortex. The fact that the effects of the refined core model are seen here on the retreating side but not on the advancing side indicates that some element of the structure of the group of filaments encountering the blade in the first quadrant has not been fully captured with this low setting of the vortex age parameter. Increasing this parameter leads to the result in Figure 7-23, which indicates that the measured loading signature on the advancing side is now beginning to be captured (though some extraneous loading events at other azimuth locations also appear).

Increasing the vortex age parameter in this manner in general leads to fewer filaments being bundled into a replacement vortex at a given azimuthal age, but it also leads to a shift in the position of the replacement vortex, owing to the assumption that this vortex is positioned at the centroid of the bundled filaments. The change in predicted loading observed here is attributed to this effect; though fewer filaments are bundled together as the age parameter is increased - resulting in a weaker replacement vortex - the position of the bundled filament appears to shift closer to the blade, leading to the appearance of a loading event that resembles the measured signature.

In one sense, this result simply reinforces a lesson of both this and previous investigations, namely that miss distance is very important in capturing BVI loading. However, here only a subset of the trailed filaments from the generating blade will in general participate in the close interaction, suggesting that the vortical structure that the blade encounters is only partially rolled up. Qualitatively, the vortex wake geometry in this interaction is similar to that shown in Figure 7-9 for Test Point 1137, with a group of widely spaced filaments trailing from the blade in the second quadrant bundling loosely together and encountering the blade in the first quadrant. Ultimately, it will be necessary to obtain better resolution of the rollup process to enhance confidence in the quantitative predictions, but the present results are judged to be a promising step in the direction of illustrating the important mechanisms at work in this type of interaction.

To illustrate the effects of the refined vortex core model on high resolution noise prediction, the surface pressure distributions from the computations above were used to calculate the sound pressure level at microphone 9. The results are presented in Figure 7-24, with and without the refined core model. As is seen in this figure, using the refined core model captures the spikiness associated with BVI noise found in the data, whereas the spikiness is not predicted with the baseline Scully core model. Though there are still magnitude and phasing discrepancies between the prediction and the data, this result is encouraging and suggests that further improvement of the refined vortex core model within the reconstruction scheme is required to successfully capture the impulsive BVI noise signature.
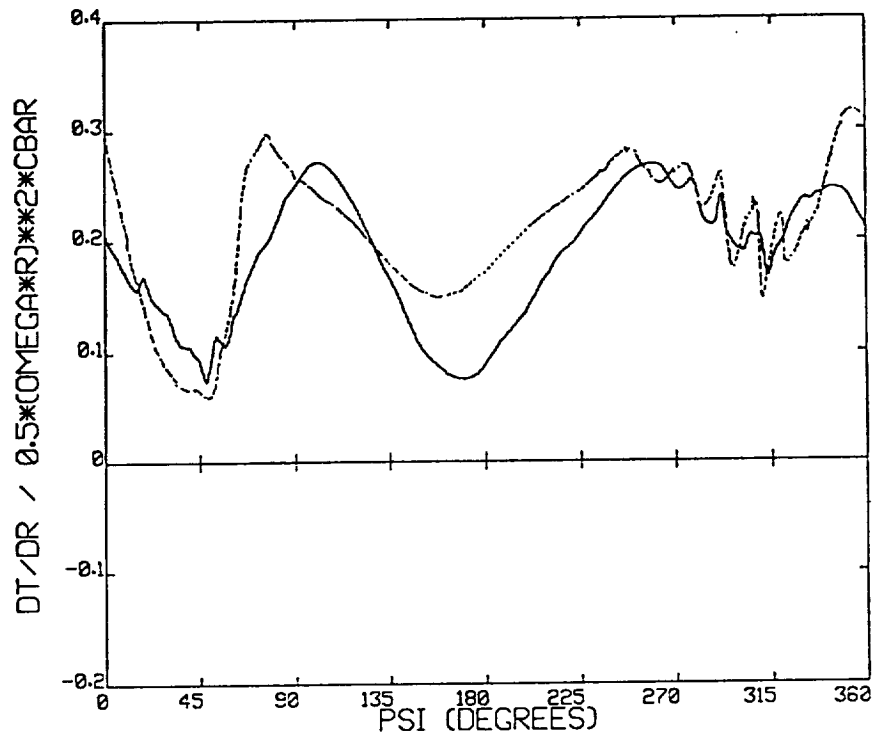
a) r/R = .865
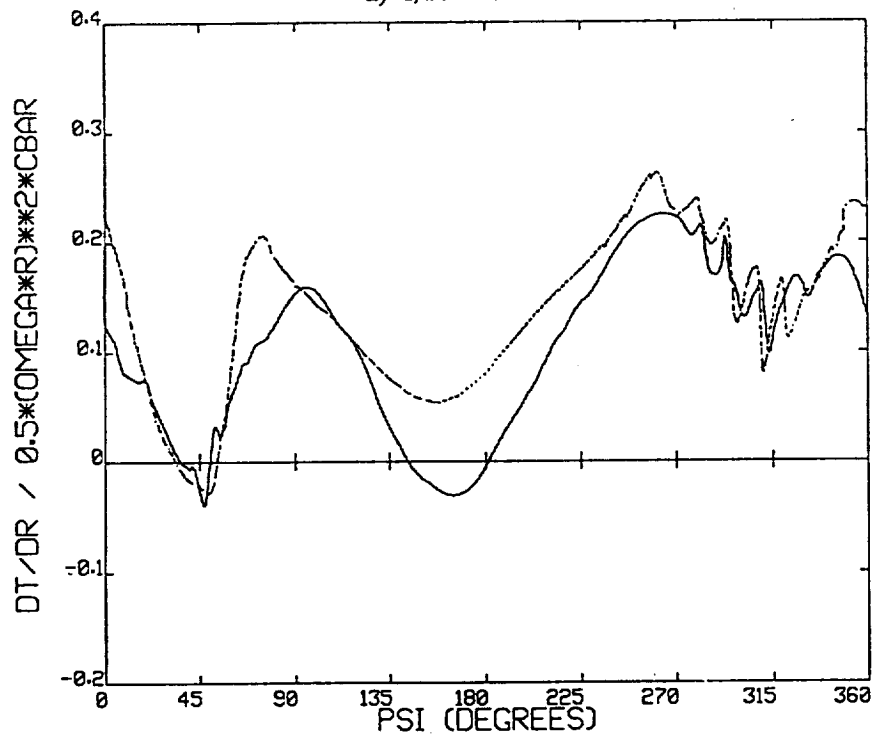
b) r/R = .920

Figure 7-22. Sikorsky UH-60A dC_T/dx for Test Point 1126; 20 filaments and 32 time steps reconstructed to 960 time steps; refined vortex core with low vortex age parameter (solid = measured, dotted = predicted).
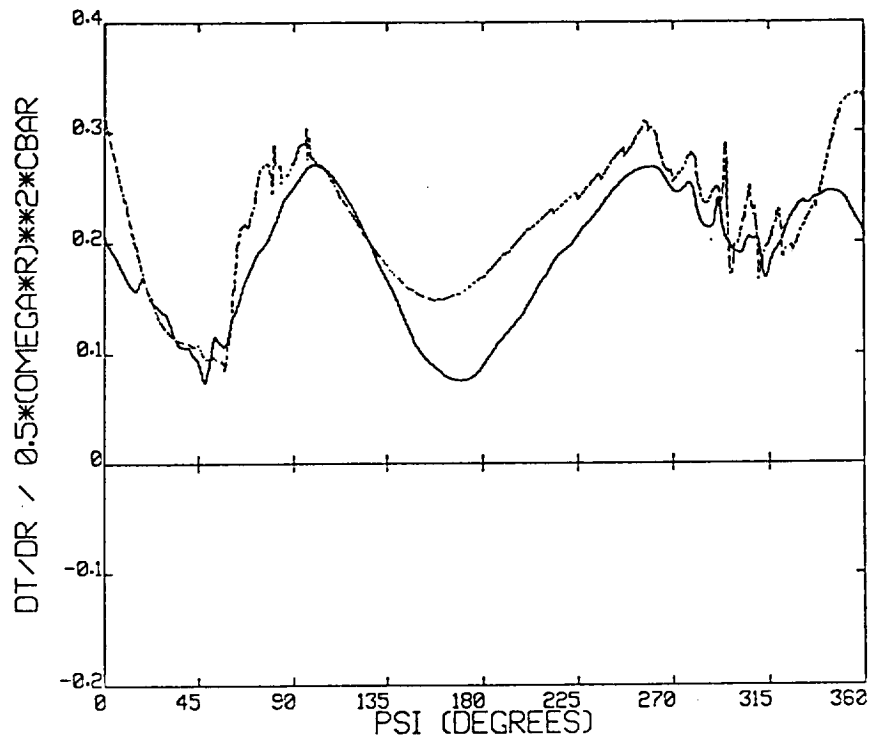
a) r/R = .865
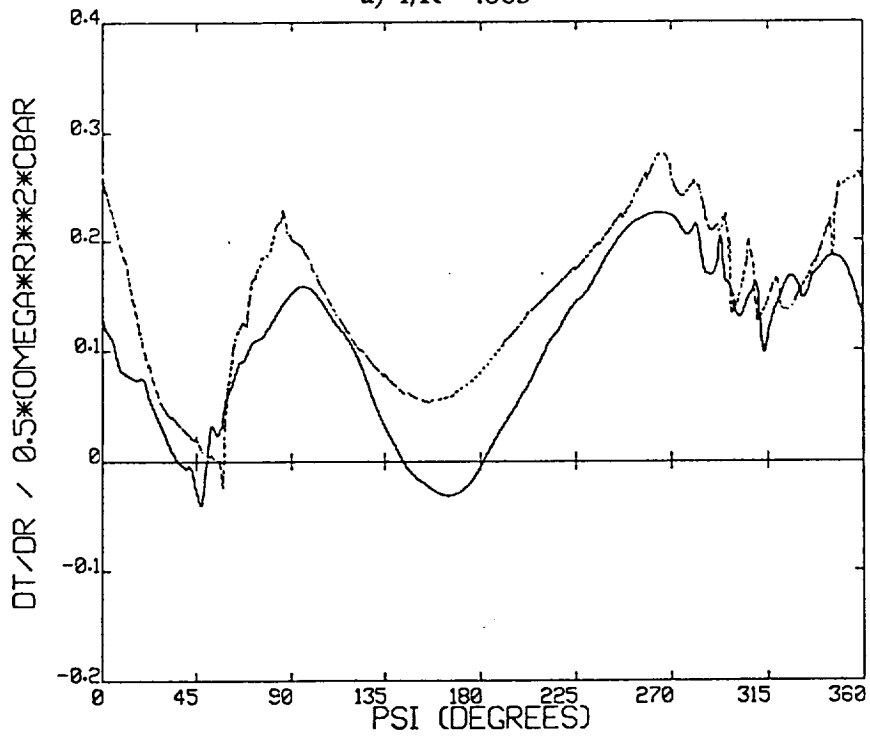
b) r/R = .920

Figure 7-23. Sikorsky UH-60A dC_T/dx for Test Point 1126; 20 filaments and 32 time steps reconstructed to 960 time steps; refined vortex core with high vortex age parameter (solid = measured, dotted = predicted).
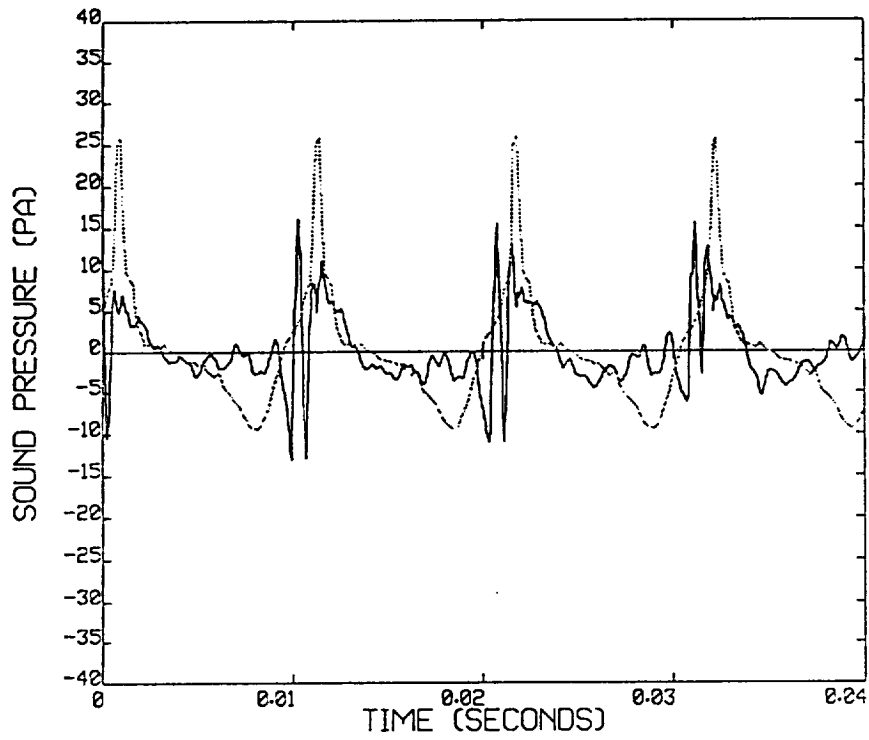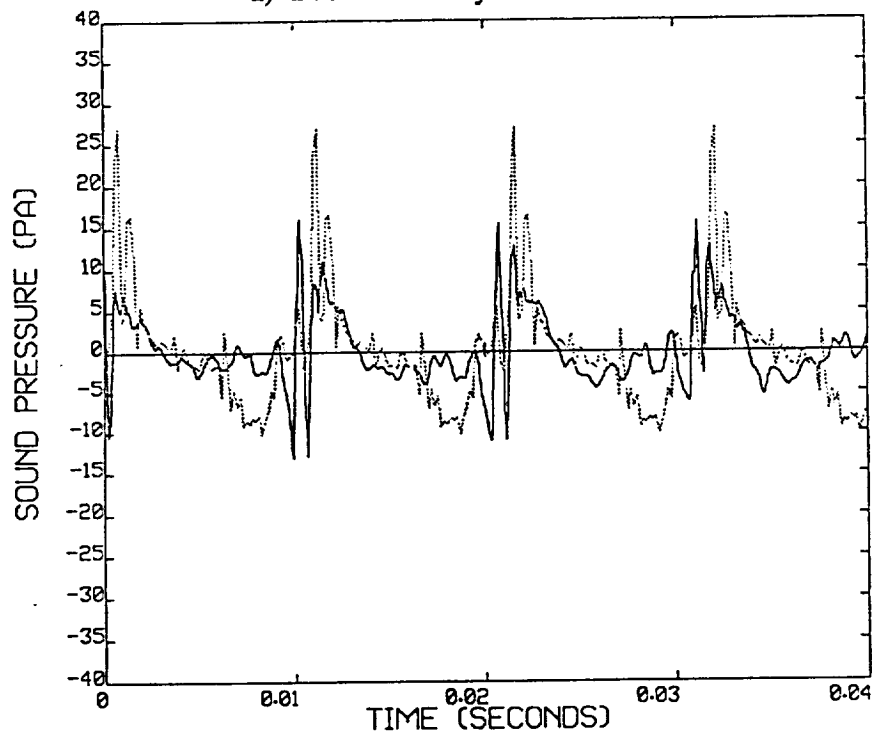
105

a) Baseline Scully core model

b) Refined vortex core with high vortex age parameter

Figure 7-24.   Acoustic pressure computed at microphone 9 for Test Point 1126
(solid = measured, dotted = predicted).

106

8.0 SUMMARY AND FUTURE WORK

The focus of this effort has been on developing and demonstrating methods for applying reconstruction techniques using the CVC wake model for the prediction of high resolution airloads. The reconstruction approach permits such calculations to be carried out with dramatically reduced computation time compared to conventional direct methods. The original formulation and implementation of flow field reconstruction for main rotors and tail rotors has been extended to directly address the loads induced by the interaction of the rotor with its self-generated wake. Demonstration calculations carried out on realistic rotor configurations in both high- and low-speed flight have shown that the current reconstruction procedure can produce high resolution predictions of the wake-induced loading. Furthermore, these reconstruction calculations confirm and even exceed early estimates of a reduction of from one to two orders of magnitude in CPU relative to direct calculations.

During the course of this effort, considerable additional improvements have been made beyond the implementation and testing of reconstruction. For example, new, accelerated free vortex modeling methods have been brought to bear on the initial low-resolution computations. Even though relatively large time steps are used in these computations, the need to have adequate spatial resolution of the CVC wake (i.e., a sufficient number of spanwise filaments and an adequate length of free wake downstream of the generating blade) means that large numbers of vortex elements will still be in use, causing a substantial computational burden. The fast vortex method applied here allows reductions in CPU of a factor of three to five for typical rotor wake computations. An alternative time integration scheme has also been employed in conjunction with code options that limit the domain of full free wake computations to offer a further factor of two to three reduction in CPU. In sum, an order of magnitude reduction in computation time can be realized over and above that obtained through the application of reconstruction.

Integral modeling of the rollup of the trailing wake from the rotor blades has made possible improved representation of the vortex core. This new core model builds on a flexible numerical matching technique that incorporates a more realistic core structure into the swirl velocity profile. This type of modeling is an example of the flexibility afforded by the reconstruction approach, which allows the analytical swirl velocity profile to be matched into the CVC filament model in a consistent manner. This implementation has also helped remove another layer of arbitrariness from the representation of the vortex wake by introducing a swirl velocity profile with direct physical motivation. While more general models for the core structure can and should be developed, the present treatment is a useful "template" for such successor models.

The analysis of rotor blade aerodynamic loading has been enhanced through the application of a selectively refined vortex lattice computation that provides improved resolution of the surface pressure distribution on the airfoil for input to the WOPWOP noise analysis. This refined lattice capability includes the effect of the unsteady near wake through an indicial function model that implicitly builds in the spanwise shed vorticity in the region immediately downstream of the blade.

Also, the final version of RotorCRAFT/AA has retained and in some cases enhanced the dual rotor capability built into the baseline high-resolution flow field code that was in hand at the outset of the effort. These capabilities have not been extensively discussed in this document, since the present focus is on correlation work with main rotor

airloads. However, the potential for dual rotor computations remains for application to tilt rotor, tandem, and coaxial configurations, within the limitations discussed above.

As indicted in the correlation studies discussed in this report, the current version of RotorCRAFT/AA has produced promising agreement with measured data, though results vary from case to case. Low resolution computations of unsteady loading at several radial stations for both the Boeing 360 and the UH-60 are close to the measured values, even though the predictions are effectively filtered by the use of coarse time steps. A similar assessment applies to the noise computations of the UH-60 test, where the gross size and phasing of the acoustic pressure is reasonably well captured at several different microphone locations.

High resolution computations with time steps as small as 0.375 deg. show the benefits of applying reconstruction to these airload and noise calculations and the importance of precise vortex core modeling for capturing the high frequency events properly. The application of the new integral core model appears to contribute substantially to the accuracy of the predicted unsteady airloads, in particular to begin to capture the loading characteristic of first-quadrant BVI events. In addition, the computations with both high time resolution and the enhanced core model in place capture some of the appropriate physical features of BVI noise in the far field, though the sensitivities of the predicted results to such issues as spatial resolution of the CVC wake, the choice for modeling the surface pressures, and the detailed structure of the core have yet to be fully determined.

A variety of near term tasks remain to be pursued during ongoing development of RotorCRAFT/AA. Additional test calculations must be carried out to assess the robustness and accuracy of using various combinations of temporal interpolation and vortex rollup strategies to predict measured airloading. Investigations of the distinctive role of the inboard wake should also be conducted, to assess its importance in determining the unsteady loading encountered by the rotor. Dual rotor calculations should be undertaken to document and evaluate the ability of RotorCRAFT/AA to directly address tail rotor loading and noise. Also, as discussed in the previous section, additional work must be done on analyzing the role of partially rolled-up vortical wakes in generating crucial first-quadrant BVI loading. Finally, the costs and benefits of complete closed-loop reconstruction - in which blade motion and loads are updated to be fully consistent with the flow field generated by the high resolution inner solution - should be assessed.

In summary, substantial improvements have been achieved in the analysis of rotor/rotor-wake interactions through the development of the high-resolution CVC wake model described in this report. The use of flow field and airload reconstruction in conjunction with linear aerodynamic blade models and improved treatments of the vortex core structure have demonstrated considerable capability in capturing unsteady rotor loading that contributes to rotor noise. However, prediction of noise for tilt rotors and helicopters for fully general flight conditions will require extending current capabilities to adequately model rotor transonic aerodynamics and aeroelasticity, since the analysis of the unsteady loading of rotor blades at high speed demands both refined structural modeling and advanced analyses of computational fluid dynamics. Such an endeavor constitutes the next logical step in the development of the computational tools now available.

9.0 REFERENCES

1. Quackenbush, T.R., Lam, C.-M.G. and Bliss, D.B.: "General Flow Field Analysis Methods for Helicopter Rotor Aeroacoustics," AIAA Paper 91-0591, Jan. 1991.

2. Quackenbush, T.R. and Bliss, D.B.: "High Resolution Flow Field Predictions for Tail Rotor Aeroacoustics," AIAA Journal, Vol. 28, No. 11, Nov. 1991.

3. Quackenbush, T.R., Bliss, D.B., Wachspress, D.A., Boschitsch, A.H. and Chua, K.: "Computation of Rotor Aerodynamic Loads in Forward Flight Using a Full-Span Free Wake Analysis," NASA CR 177611, Oct. 1990.

4. Quackenbush, T.R., Bliss, D.B., Wachspress, D.A. and Boschitsch, A.H.: "Analysis of Rotor Vibratory Loads Using Higher Harmonic Pitch Control," NASA CR 189591, Apr. 1992.

5. Jacobs, E.W. and Shenoy, R.K.: "Acoustic Characteristics of Tail Rotors and the Effects of Empennage Interactions," Proc. of the 43rd Annual Forum of the AHS, May 1987.

6. Edwards, B.D., Peryea, M.A. and Brieger, J.T.: "1/5th Scale Model Studies of Main Rotor and Tail Rotor Interactions," Proc. of the AHS National Specialists' Meeting on Aerodynamics and Aeroacoustics, Feb. 1987.

7. Liu, S.R. and Marcolini, M.A.: "The Acoustic Results of a United Technologies Scale Model Helicopter Rotor Tested at DNW," Proc. of the 46th Annual Forum of the AHS, May 1990.

8. Marcolini, M., et al.: "Prediction of BVI Noise Patterns and Correlation with Wake Interaction Locations," Proc. of the 48th Annual Forum of the AHS, June 1992.

9. Ziegenbein, P.R.: "The Development of a Prediction Method for Blade-Vortex Interaction Noise Based on Measured Airloads," Proc. of the AHS/RAeS Specialists' Meeting on Rotorcraft Acoustics, Philadelphia, PA, Oct. 1991.

10. Visintainer, J., et al.: "Acoustic Predictions Using Measured Pressures from a Model Rotor in the DNW," Proc. of the 47th Annual Forum of the AHS, May 1991.

11. Baeder, J.D., Gallman, J.M. and Yu, Y.H.: "A Computational Study of the Aeroacoustics of Rotors in Hover," American Helicopter Society 49th Annual Forum Proceedings, Volume 1, May 1993.

12. Bliss, D.B., Dadone, L.U. and Wachspress, D.A.: "Rotor Wake Modeling for High Speed Applications," Proc. of the 43rd Annual Forum of the AHS, May 1987.

13. Quackenbush, T.R., Wachspress, D.A. and Boschitsch, A.H.: "Computation of Rotor Aerodynamic Loads with a Constant Vorticity Contour Free Wake Model," AIAA Paper 91-3229, Sept. 1991.

14. Brooks, T. and Booth, E.: "Rotor Blade/Vortex Interaction Noise Reduction and Vibration Using Higher Harmonic Control," Proc. of the 16th European Rotorcraft Forum, Sept. 1990.

15. Brentner, K.S.: "Prediction of Helicopter Rotor Discrete Frequency Noise," NASA TM 87721, Oct. 1986.

16. Quackenbush, T.R., and Bliss, D.B.: "Free Wake Flow Field Calculations for Rotorcraft Interactional Aerodynamics," Vertica, Vol. 14, No. 3, 1990.

17. Bliss, D.B. and Miller, W.O.: "Vortex Filament Calculations by Analytical/Numerical Matching with Comparisons to Other Methods," AIAA Paper 89-1962, June 1989.

18. Miller, W.O. and Bliss, D.B.: "Direct Periodic Solutions of Rotor Free Wake Calculations by Inversion of a Linear Periodic System," Proc. of the 46th Annual Forum of the AHS, May 1990.

19. Heffernan, R.M., et al.: "Structural and Aerodynamic Loads and Performance Measurements of an SA349/2 Helicopter with an Advanced Geometry Rotor," NASA TM-88370, Nov. 1986.

20. Scheiman, J.: "A Tabulation of Helicopter Rotor-Blade Differential Pressures, Stresses, and Motions Measured in Flight," NASA TM-X 952, Mar. 1964.

21. Rabbott, Jr., J.P., Lizak, A.A. and Paglino, V.M.: "A Presentation of Measured and Calculated Full-Scale Rotor Blade Aerodynamic and Structural Loads," USAAVLABS, TR 66-31, July 1966.

22. Wachspress, D.A., Quackenbush, T.R. and Boschitsch, A.H.: "RotorCRAFT (Mod 1.0) Users Manual," Continuum Dynamics, Inc. Technical Note No. 91-12, Oct. 1991.

23. Hamming, R.W.: Numerical Methods for Scientists and Engineers, 2nd Ed., McGraw-Hill, New York, NY, 1973

24. Bliss, D.B., Teske, M.E., and Quackenbush, T.R.: "A New Methodology for Free Wake Analysis Using Curved Vortex Elements," NASA CR 3958, 1987.

25. Spalart, P.R. and Leonard, A.: "Computation of Separated Flows by a Vortex Tracing Algorithm," AIAA Paper 81-1246, 1981.

26. Anderson, C. and Greengard, C.: "On Vortex Methods," SIAM Jour. of Numerical Analysis, Vol. 22, pp. 413, 1984.

27. Appel, A.W.: "An Efficient Program for Many-Body Simulation," SIAM Jour. Sci. Stat. Comp., Vol. 6, p. 85, 1985.

28. Quackenbush, T.R., Lam, C.-M. G., Bliss, D.B. and Katz A.: "Vortex Methods for the Computational Analysis of Rotor/Body Interaction," Proc. of the 48th Annual Forum of the American Helicopter Society, Washington, D.C., June 1992.

29. Chua, K. and Quackenbush, T.R.: "A Three-Dimensional Fast Vortex Method for the Numerical Simulation of Reactive Flows on Parallel Computers," Continuum Dynamics, Inc. Report No. 92-03, June 1992.

30. Leishman, J.G. and Bi, N.: "Aerodynamic Interactions between a Rotor and a Fuselage in Forward Flight," Jour. AHS, Vol. 35, No. 3, p. 22, 1990.

31. Cook, C.V.: "The Structure of the Rotor Blade Tip Vortex," AGARD Conference Proceedings No. 111, Marseilles, France, Sept. 1972.

32. Biggers, J.C., Lee, A., Orloff, K.L. and Lemmer, A.J.: "Measurements of Helicopter Rotor Tip Vortices," Preprint No. 77.33-06, presented at the 33rd Annual Forum of the American Helicopter Society, Washington, D.C., May 1977.

33. Tung, C., Pucci, S.L., Caradonna, F.X. and Morse, H.A.: "The Structure of Trailing Vortices Generated by Model Rotor Blades," Vertica, Vol. 7, No. 1, 1983.

34. Strawn, R.C.: "Wing Tip Vortex Calculations with an Unstructured Adaptive-Grid Euler Solver," AHS 47th Annual Forum Proc., Vol. 1, Phoenix AZ, pp. 65-76, May 1991.

35. Scully, M.P.: "Computation of Helicopter Rotor Wake Geometry and Its Influence on Rotor Harmonic Airloads," Massachusetts Institute of Technology Aeroelastic and Structures Research Laboratory, ASRL TR 178-1, Mar. 1975.

36. Sadler, S.G.: "Main Rotor Free Wake Geometry Effects on Blade Air Loads and Response for Helicopters in Steady Maneuvers," NASA CR 2110, Volume I and NASA CR 2111, Volume II, Sept. 1972.

37. Johnson, W.J.: "A Comprehensive Analytical Model of Rotorcraft Aerodynamics and Dynamics," NASA TM 81182, June 1980.

38. Bliss, D.B.: "Analysis of Tip Vortex Structure and Self-Induced Motion," Continuum Dynamics, Inc. Report No. 86-06, Aug. 1986.

39. Betz, A.: "Behavior of Vortex Systems," NACA, TM 713, June 1933.

40. Donaldson, C.duP., Snedeker, R.S. and Sullivan, R.D.: "A Method of Calculating Aircraft Wake Velocity Profiles and Comparison with Full-Scale Experimental Measurements," J. of Aircraft, Vol. 11, Sept. 1974.

41. Bilanin, A.J. and Donaldson, C.duP.: "Estimation of Velocities and Roll-Up in Aircraft Vortex Wakes," J. of Aircraft, Vol. 12, No. 7, July 1975.

42. Quackenbush, T.R. and Bliss, D.B.: "Prediction of High Resolution Flow Fields for Tail Rotor Aeroacoustics," Continuum Dynamics, Inc. Report No. 88-08, Aug. 1988.

43. Ellin, A.D.S.: "Tail Rotor Aerodynamic Features Recorded in Flight," Proc. of the 16th European Rotorcraft Forum, Paper I.4.4., Sept. 1990.

44. Ellin, A.D.S.: "Flight Measurements Illustrating Key Features of Tail Rotor Loading Distribution," presented at Royal Aerospace Establishment Conference on Yaw Control Concepts, London, England, Feb. 1990.

45. Wachspress, D.A., Lam, C.-M.G. and Quackenbush, T.R.: "RotorCRAFT/AA Mod 0.0 User's Manual," Continuum Dynamics, Inc. Technical Note No. 93-13, Nov. 1993.

46. Schlinker, R.H. and Amiet, R.K.: "Rotor-Vortex Interaction Noise," AIAA Paper 83-0720, AIAA 8th Aeroacoustics Conference, Atlanta, GA, Apr. 1983.

47. Tadghighi, H.: "An Analytical Model for Prediction of MR/TR Interaction Noise," Proc. of the 44th Annual Forum of the AHS, Washington, D.C., June 1988.

48. Torok, M. and Berezin, C.R.: "Aerodynamic and Wake Methodology Evaluation Using the Model UH-60A Wind Tunnel Experimental Data," Proc. of the 48th Annul Forum of the AHS, May 1992.

49. Hassan, A.A., Charles, B.D., Tadghighi, H. and Burley, C.: "A Consistent Approach For Modeling The Aerodynamics Of Self-Generated Rotor Blade-Vortex Interactions," Proc. of the 49th Annual Forum of the AHS, Vol. 1, May 1993.

50. Adamczyk, J.J.: "The Passage of an Infinite Swept Airfoil Through an Oblique Gust," NASA CR-2395, 1973.

51. Margason, R.J. and Lamar, J.E.: "Vortex Lattice FORTRAN Program for Estimating Subsonic Aerodynamic Characteristics of Complex Planforms," NASA TN-D 6142, 1971.

52. Murray, J.C. and Carta, F.O.: "Lifting Surface Theory for Statically Operating Propellers," United Aircraft Research Labs, East Hartford, CT, AFAPL-TR-72-100, Dec. 72.

53. Moran, J.: An Introduction to Theoretical and Computational Aerodynamics, John Wiley & Sons, New York, NY, 1984.

54. Ueda, T. and Dowell, E.H.: "A New Solution Method for Lifting Surfaces in Subsonic Flow," AIAA Journal, Vol. 20, No. 3, pp. 348-355, Mar. 1982.

55. Eversman, W. and Pitt, D.M.: "Hybrid Doublet Lattice/Doublet Point Method for Lifting Surfaces in Subsonic Flow," J. of Aircraft, Vol. 28, No. 9, pp. 572-578, Sept. 1991.

56. Dadone, L.U., Dawson, S., and Ekquist, D.: "Model 360 Rotor Test at DNW - Review of Performance and Blade Airload Data," Proc. of the 43rd Annual Forum of the AHS, May 1987.

57. Lorber, P.F.: "Blade-Vortex Interaction Data Obtained from a Pressure-Instrumented Model UH-60A Rotor at the DNW," J. of the American Helicopter Society, Vol. 38, No. 3, July 1993.

58. Liu, S.R. and Marcolini, M.A.: "The Acoustic Results of a United Technologies Scale Model Helicopter Rotor Tested at DNW," Proc. of the 46th Annual Forum of the AHS, May 1990.

59. Lorber, P.F.: "Pressure-Instrumented Model UH-60A Black Hawk Rotor Test at DNW, Vol. 1: Description of Experiment," United Technologies Research Center Report R91-153577-1, Feb. 1991.

60. Quackenbush, T.R., Bliss, D.B., Wachspress, D.A. and McKillip, R.M.: "Free Wake Analysis of Rotor Configurations for Reduced Vibratory Airloads," presented at the AHS National Specialists' Meeting on Rotorcraft Dynamics, Arlington, TX, Nov. 1989.

61. Torok, M.S. and Goodman, R.K.: "Analysis of Rotor Blade Dynamics Using Experimental UH-60A Airloads Obtained at the DNW," Proc. of the 47th Annual Forum of the AHS, May 1991.

REPORT DOCUMENTATION PAGE

1. AGENCY USE ONLY (Leave blank)	2. REPORT DATE May 1994	3. REPORT TYPE AND DATES COVERED Contractor Report

4. TITLE AND SUBTITLE

Computational Analysis of High Resolution Unsteady Airloads for Rotor Aeroacoustics

6. AUTHOR(S)

Todd R. Quackenbush, C.-M. Gordon Lam, Daniel Wachspress, and Donald B. Bliss

5. FUNDING NUMBERS

C NAS1-19303

WU 324-02-03

7. PERFORMING ORGANIZATION NAME(S) AND ADDRESS(ES)

Continuum Dynamics, Inc.
P.O. Box 3073
Princeton, NJ 08543-3073

8. PERFORMING ORGANIZATION REPORT NUMBER

C.D.I. Report No. 93-12

9. SPONSORING/MONITORING AGENCY NAME(S) AND ADDRESS(ES)

National Aeronautics and Space Administration
Langley Research Center
Hampton, VA 23681-0001

10. SPONSORING/MONITORING AGENCY REPORT NUMBER

NASA CR 194894

11. SUPPLEMENTARY NOTES

Langley Technical Monitor: Thomas F. Brooks
Final Report

12a. DISTRIBUTION/AVAILABILITY STATEMENT

Unclassified-Unlimited

Subject Category 71

12b. DISTRIBUTION CODE

13. ABSTRACT (Maximum 200 words)

The study of helicopter aerodynamic loading for acoustics applications requires the application of efficient yet accurate simulations of the velocity field induced by the rotor's vortex wake. This report summarizes work to date on the development of such an analysis, which builds on the Constant Vorticity Contour (CVC) free wake model, previously implemented for the study of vibratory loading in the RotorCRAFT computer code. The present effort has focused on implementation of an airload reconstruction approach that computes high resolution airload solutions of rotor/rotor-wake interactions required for acoustics computations. Supplementary efforts on the development of improved vortex core modeling, unsteady aerodynamic effects, higher spatial resolution of rotor loading, and fast vortex wake implementations have substantially enhanced the capabilities of the resulting software, denoted RotorCRAFT/AA (AeroAcoustics). Results of validation calculations using recently-acquired model rotor data show that by employing airload reconstruction it is possible to apply the CVC wake analysis with temporal and spatial resolution suitable for acoustics applications while reducing the computation time required by one to two orders of magnitude relative to that required by direct calculations. Promising correlation with this body of airload and noise data has been obtained for a variety of rotor configurations and operating conditions.

14. SUBJECT TERMS

Rotor aeroacoustics; Rotor aerodynamics; Free wake analysis; High resolution airloading

15. NUMBER OF PAGES

119

16. PRICE CODE

17. SECURITY CLASSIFICATION OF REPORT	18. SECURITY CLASSIFICATION OF THIS PAGE	19. SECURITY CLASSIFICATION OF ABSTRACT	20. LIMITATION OF ABSTRACT
Unclassified	Unclassified		